DOSIMETRIC PROPERTIES OF α-Al$_2$O$_3$:C EXPOSED

TO IONIZING AND NON-IONIZING

RADIATION

By

LESLIE EDWARD COLYOTT

Bachelor of Science
Southern Illinois University
Edwardsville, Illinois
1991

Master of Science
Southern Illinois University
Edwardsville, Illinois
1992

Submitted to the Faculty of the
Graduate College of the
Oklahoma State University
in partial fulfillment of
the requirements for
the Degree of
DOCTOR OF PHILOSOPHY
July, 1997

DOSIMETRIC PROPERTIES OF α-Al$_2$O$_3$:C EXPOSED

TO IONIZING AND NON-IONIZING

RADIATION

Thesis Approved:

_____
Thesis Advisor

_____

_____

_____

_____

_____
Dean of the Graduate College

ACKNOWLEDGMENTS

I would like to thank my advisor, Dr. Stephen McKeever, for all of his guidance and patience over the past few years. I will never be able to thank him enough. I want to thank the other members of my committee for making themselves available to me whenever I asked. In particular, I must thank Dr. Joel Martin for the seemingly endless supply of borrowed equipment.

Several colleagues have also helped me tremendously over the years. I want to specifically thank Drs. Mark Akselrod, Dan Bloom, Art Fischer, Arthur Lucas, Brian Markey and Ted Schmidt for their invaluable help, both in the lab and out.

Several experiments required the assistance of Mike Lucas, Wes Cash and Larry Vaughn in the Machine Shop and Tom Denton in the Glass Shop. I sincerely thank each of you.

I want thank the Physics Department and State of Oklahoma for their financial support during this time.

My parents have been a constant source of love and support throughout my life and I will never be able to thank them for all that they have done for my family. Judy's parents, Frank and Delores, have also been a constant source of love and support. The four of you have helped us more than you realize. Thank you.

My wife Judy and children, Sydney, Chelsea and Laban, have helped me more than they will ever realize. Their love and support have been greatly appreciated, though they may

not have always realized this. The children have only known a father who has gone to school their entire lives. Now he will finally be getting a job!

Finally, I must thank my wife for all of her endless sacrifice, including that of her own education, in order to support our family and household over the past nine years. She has been nothing short of selfless throughout this endeavor. I will never be able to thank her enough. Thank you Judy. I love you.

TABLE OF CONTENTS

LIST OF TABLES

LIST OF FIGURES

Chapter 1

1 Introduction

The pioneering research in thermoluminescence (TL) dosimetry, led by Farrington Daniels and his group at the University of Wisconsin, began in the 1950s. Aluminum oxide (Al_2O_3) emerged as a thermoluminescence detector (TLD) in 1957 with a paper by Rieke and Daniels[1], which provided the first detailed study of the thermoluminescence properties of Al_2O_3. Around the same time, some of the material properties of Al_2O_3 (such as optical absorption bands[2,3] and their associated oscillator strengths[4]) were first determined. These investigations were extended in the 1960s and early 1970s to include the determination of lattice displacement threshold energy[5], the effect of x-rays on the optical properties of ruby (Al_2O_3:Cr)[6], emission spectra of ruby[7,8], gamma energy dependence[9] and additional optical absorption band measurements[10,11]. The era resulting in the most prolific research on Al_2O_3 was the period spanning the mid-1970s to late-1980s. During this time, most of the research related to α-Al_2O_3 focused attention on the origins of the optical absorption bands[12–18] and luminescence centers[18–27]. Unfortunately, the use of α-Al_2O_3 in TL dosimetry never gained the popularity of other TLD materials (most notably, LiF:Mg,Ti), due to the relatively poor sensitivity and higher energy dependence at low gamma photon energies. Attempts to increase the popularity of α-Al_2O_3, by improving the sensitivity and readout parameters (i.e. peak temperature and emission wavelength) through the introduction of various dopants[28–31], were only marginally successful.

Beginning in 1990, the dosimetry community's attitude toward α-Al_2O_3–based TLDs began to change with the introduction of α-Al_2O_3:C[32] as a new TLD material. This new material possessed a sensitivity to gamma radiation some 50 times that of the industry standard (TLD-100, otherwise known as LiF:Mg,Ti) and a linear dynamic range of nearly 7 decades of gamma dose, with a dose threshold (i.e. minimum measurable dose) equivalent to only a few hours of natural background radiation exposure. Since that time, many researchers have investigated the material and dosimetric properties of α-Al_2O_3:C. These investigations include descriptions of the general dosimetric properties[32–46], the TL and exoemission properties[47–53], the influence of the deep traps[54], the comparison between bulk crystal and surface layer sensitivity[55], light-induced fading[56–59] of TL and other optically stimulated phenomena[60–67], such as phototransferred thermoluminescence (PTTL) and optically stimulated luminescence (OSL).

1.1 Crystal Growth and Structure

The α-Al_2O_3:C samples used in this research were grown using the Czochralski method of crystal growth by either Medus (Russia) or Stillwater Sciences (Oklahoma). The starting material was Verneuil grown α-Al_2O_3 (corundum), which was melted and pulled in a strongly reducing atmosphere in the presence of graphite[32], using α-Al_2O_3 seed crystals. As a result of these growing conditions, the crystals have a relatively large concentration of carbon (100–5000 ppm) with respect to other impurities (Ca ~30 ppm, Cr and Ti ~10 ppm, Ni and Si ~5 ppm and Cu, Fe and Mg <2 ppm)[55]. The single-crystal α-Al_2O_3:C rods have a diameter of 5 mm and length of approximately 500 mm. The rods were cut into 1 mm thick discs, or crushed into powder form with a ball-tube mill.

The crystal structure of α-Al_2O_3:C is a distorted hexagonal close packed O^{2-} ion sublattice, with Al^{3+} ions occupying two thirds of the octahedral interstices, as shown in Figure 1.1. Each oxygen atom is tetrahedrally bound by four aluminum atoms, as in Figure 1.2. The four O—Al bond lengths are paired, with two longer bond lengths of 1.97 Å and two shorter bond lengths of 1.86 Å.

The strongly reducing atmosphere during crystal growth introduces additional oxygen vacancies into the crystal lattice. These oxygen vacancies create F- and F^+-centers in the crystal lattice. Two electrons trapped by an oxygen vacancy produces an F-center, which is neutral with respect to the crystal lattice. Similarly, an oxygen vacancy which traps only one electron produces an F^+-center, which is positively charged with respect to the crystal lattice. Electrons which become trapped at these latter defect sites convert the F^+-centers into F-centers. These defect sites (F- and F^+-centers) are an integral part of the TL process.

1.2   Material Properties

Levy[11] was the first researcher to measure a band gap of ~9.0 eV in α-Al_2O_3. The optical absorption bands at 6.1 eV (205 nm) and 4.8 eV (255 nm) were measured by Levy and Dienes[3] and later assigned to an F-center (6.1 eV) by Lee and Crawford[13] and an F^+-center (4.8 eV) by Buckman[8]. The 5.4 eV (230 nm) optical absorption band discovered by Hunt and Schuler[2] was labeled an F^+-center by Evans and Stapelbroek[15]. Lee and Crawford[13] first measured the optical absorption bands at 4.1 eV (300 nm), 3.5 eV (355 nm) and 2.7 (450 nm), which were later assigned to F_2-, F_2^+- and F_2^{2+}-centers, respectively, by Pogatshnik et al.[16] The optical absorption band at 1.8 eV (692 nm) measured by Draeger and Summers[20] has not been assigned to any particular defect structure.
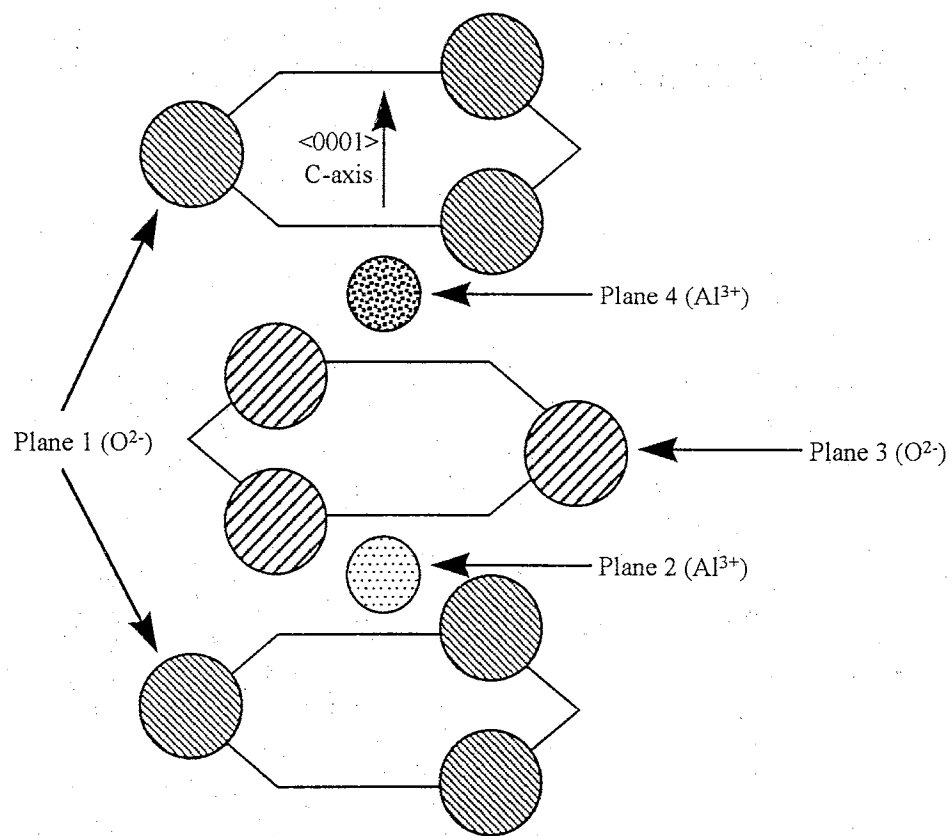
Figure 1.1 - Schematic Diagram of α-Al_2O_3 Crystal Structure. The crystal structure of aluminum oxide consists of a hexagonal close pack of O^{2-} ions (larger circles) with Al^{3+} ions (smaller circles) interstitial ions.
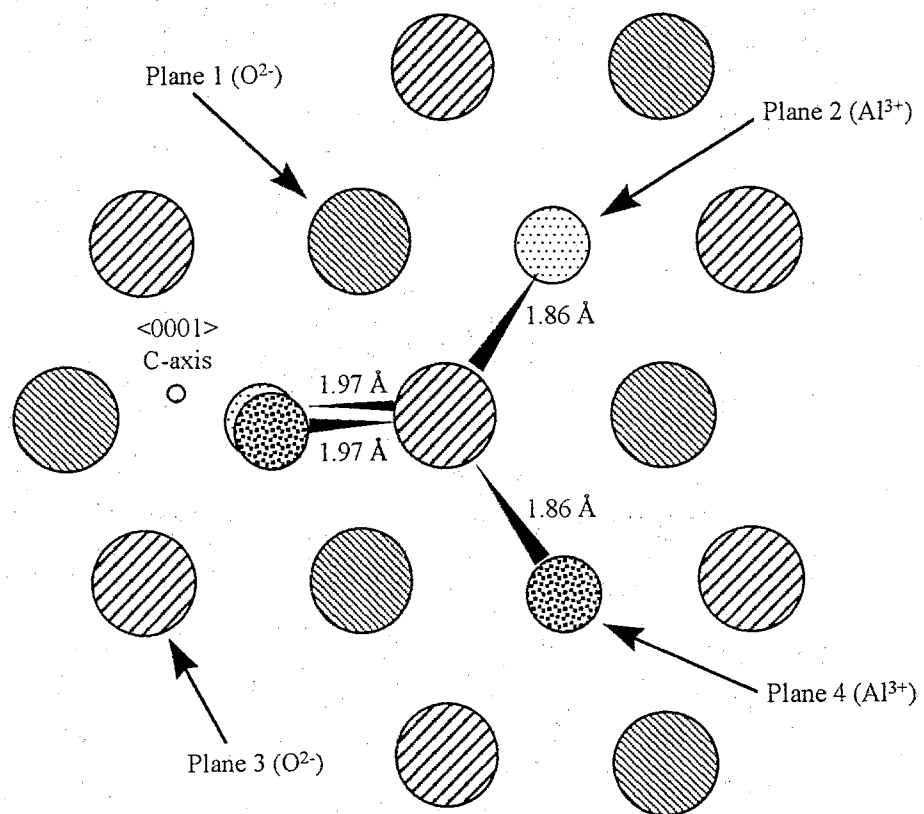
Figure 1.2 - Schematic Diagram of Oxygen Ion Tetrahedrally Bound to Aluminum Ions. Each oxygen ion (larger circles) has four bonds with aluminum ions (smaller circles) - two each of lengths 1.86 Å and 1.97 Å.

The emission bands at 3.8 eV (330 nm), 2.5 eV (505 nm) and 2.3 eV (550 nm) were first measured by Lee and Crawford[13]. Evans determined the 3.8 eV emission was due to F^+-center luminescence[15], while F_2- and F_2^{2+}-centers[18] were responsible for the 2.5 and 2.3 eV emission, respectively. The 3.0 eV (410 nm) emission was first detected by Hunt and Schuler[2] and has been labeled F-center luminescence by Brewer et al.[23] The emission lifetime of the 3.0 eV emission was determined to be 35 ms[21], while that of the 3.8 eV emission was measured as <7 ns[15].

The oscillator strength of the F-center was calculated by Lee and Crawford[13] to be 1.3. Later, an F^+-center oscillator strength of 0.66 was calculated by Evans and Stapelbroek[15]. The lattice displacement threshold energy of Al^{3+} and O^{2-} ions were determined to be ~50 eV and ~90 eV, respectively, by Arnold and Compton[5]. Table 1.1 summarizes the various material properties of α-Al_2O_3:C.

Table 1.1 - Summary of Material Properties of α-Al$_2$O$_3$:C.

Description	Value	Units	Reference
Band Gap	~9.0	eV	11
Optical Absorption Bands	6.1 (205)	eV(nm)	13,3
F	5.4 (230)		16,2
F$^+$	4.8 (255)		8,3
F$^+$	4.1 (300)		23,13
F$_2$	3.5 (355)		23,13
F$_2^+$	2.7 (450)		23,13
F$_2^{2+}$	1.8 (692)		17
Emission Bands			
F$^+$	3.8 (330)	eV(nm)	16,13
F	3.0 (410)		20,2
F$_2$	2.5 (505)		27,13
F$_2^{2+}$	2.3 (550)		27,13
Oscillator Strengths			
F	1.3		13
F$^+$	0.66		16
Lattice Displacement Threshold Energy			
Al	~50	eV	5
O	~90	eV	5
Emission Lifetimes			
3.0 eV	36	ms	27
3.8 eV	7	ns	16

7

1.3   Dissertation Project

This project involves the investigation of the dosimetric properties of α-Al$_2$O$_3$:C exposed to various forms of ionizing and non-ionizing radiation. The purpose of this investigation is to provide a comprehensive study of the PTTL properties, which, in turn, will provide a more comprehensive understanding of the role played by the deeper traps in α-Al$_2$O$_3$:C in the TL process. The information regarding the PTTL properties of α-Al$_2$O$_3$:C have also had a direct effect on the determination of this material's OSL properties (e.g. determination of the optimum wavelengths to use for OSL measurements). In addition, the inherent neutron response of this material is poor (about 4%, relative to gamma radiation). Thus, new methods of analyzing the neutron-induced TL signal were implemented, in order to enhance the detection of these signals. Finally, new methods of thermochemical treatment of this material have proven to be beneficial in the areas of neutron dosimetry and ultra high-dose measurement.

Chapter 2 provides a detailed theoretical development of the mechanisms involved in the charge transfer, energy storage and energy release phases of TL and PTTL.

In Chapter 3, the discussion centers on the general PTTL properties of α-Al$_2$O$_3$:C, such as the dependence of the PTTL signal on wavelength, temperature, dose and illumination time. This analysis is then extended to characterize some deep trap parameters, such as thermal activation and selective phototransfer. Selective phototransfer involves the transfer of charge carriers from specific deep traps to specific shallow traps, based upon the wavelength used in the phototransfer process and the temperature of the sample during illumination.

The dependence of the PTTL signal on post-irradiation anneal, pre-dose history and temperature are detailed in Chapter 4. This includes a discussion of the wavelength dependence of the light-induced fading of the TL signal. As a result of these experiments, a theoretical model is developed which attempts to explain the balance between the fading and the phototransfer of the TL/PTTL signal.

Chapter 5 details the application of PTTL to a dosimeter which measures the integrated ultraviolet-B (UVB) exposure in air or in water. This dosimeter exploits the increased phototransfer efficiency of α-Al$_2$O$_3$:C to light in the UVB region of the spectrum to produce a near-linear dynamic range of over three decades of UVB exposure. The dosimeter exhibits virtually no temperature dependence in the region of biological interest. Through the use of diffusers, the inherent angular dependence of the interference filter is broadened, thus improving the overall angular dependence of the dosimeter.

In Chapter 6, TL and PTTL signals are analyzed, using an algorithm which assumes that a distribution of trapping levels are responsible for the observed TL signals. The signals are deconvolved into unique distribution signatures, which enable the discrimination between irradiations due to gamma/beta, alpha and neutrons.

The results of experiments involving the high temperature anneal of α-Al$_2$O$_3$:C powder in an oxygen atmosphere are discussed in Chapter 7. These experiments suggest a diffusion of oxygen vacancies out of the crystal lattice under these conditions, resulting in a decrease in F- and F$^+$-centers. As a result, the F-center luminescence is reduced – effectively desensitizing the gamma response of the material. In addition, TL resulting from exposure to ultraviolet light suggests a discrete distribution of trapping levels. Application of the deconvolution algorithm described in Chapter 6 confirms this analysis.

Chapter 8 summarizes the work performed in this study and provides a few possible directions for future work related to this study.

Chapter 2

2 Theory of Thermoluminescence and Phototransferred Thermoluminescence

2.1 Introduction

Radiation dosimetry is the measurement of the absorbed dose of radiation resulting from the interaction of radiation with matter[68]. The absorbed dose is the energy imparted per unit mass by a medium, where the energy imparted is essentially the energy removed from the radiation field. In practice, however, radiation dosimetry is the determination of absorbed dose in the medium of interest, via the measurement of a radiation-induced effect in another medium[69]. Typically, this involves the detection of some quantity, such as temperature, charge or, as in the present case, luminescence intensity, which is proportional to the absorbed dose in the medium of interest.

Daniels et al.[70] were the first researchers to realize the potential benefit of using thermoluminescence in radiation dosimetry. Thermoluminescence (TL) is the thermally stimulated emission of light by an insulator or semiconductor that has previously absorbed energy in the form of ionizing radiation [71]. They realized that many materials exhibit an intensity of thermoluminescence which is proportional to the amount of radiation absorbed by the material[71]. The observation of thermoluminescence was first published by Boyle in 1663 (cited in McKeever[71]), and later by others throughout the period spanning the late 1600's to late 1800's. The word 'thermoluminescence' was not coined until 1895, in a paper by Weideman and Schmidt (cited in McKeever[71]). Weideman and Schmidt also pioneered

11

the study of 'artificial' thermoluminescence by irradiating their specimens with an electron beam in the laboratory. Prior to this time, researchers had restricted their observations to 'natural' thermoluminescence, which had been induced by natural background radiation.

Daniels and colleagues first used LiF as a TL dosimeter in 1953, in order to measure the radiation resulting from an atomic weapon test[72] and also to measure the internal radiation dose received during cancer treatments[70]. Daniels abandoned LiF in 1957 to begin working with Al_2O_3. LiF did regain popularity until Cameron and colleagues (cited in McKeever[71]) developed an impurity-doped version of LiF, known as LiF:Mg,Ti. This material, marketed as TLD-100, by Bicron-NE, is the current industry standard. However, LiF:Mg,Ti is plagued by several properties which make the material unattractive for dosimetry purposes. The dose response of LiF is unpredictable, unless various pre- and post-irradiation annealing procedures are adopted. In addition, the glow curve for LiF consists of several overlapping glow peaks, which can lead to difficulties in interpreting the dosimetric results. Several other materials (e.g. LiF:Mg,Cu,P; CaF_2 - doped with Mn, Dy or Tm; $CaSO_4$ - doped with Dy or Tm; BeO; MgO and α-Al_2O_3 - doped with C or Mg,Y) have gained various levels of popularity over the years, as well[73].

Since 1965, eleven international conferences on luminescence dosimetry have been conducted: Stanford, USA (1965); Gatlinburg, USA (1968); Roskilde, Denmark (1971); Krakow, Poland (1974); Sao Paulo, Brazil (1977); Toulouse, France (1980); Ottawa, Canada (1983); Oxford, United Kingdom (1986); Vienna, Austria (1989); Washington, USA (1992) and Budapest, Hungary (1995). The published proceedings resulting from these conferences provide a history of the development of thermoluminescence dosimetry over the past 30 years.

2.2   Thermoluminescence

In general, this is described as energy (radiation) exciting an electron out of the valence band and into the conduction band. From the conduction band, the electron can then become trapped at some intermediate energy level (e.g. in the potential well of a lattice defect), referred to as an electron trap. (This discussion assumes that electrons are the charge carriers involved in the TL process; however, a similar argument can be made with respect to 'holes'. A hole is an electron vacancy which behaves in a manner similar to that of an electron. The form of the equations that follow would remain unchanged and would require only corrections to the charge carrier dependent definitions (e.g. $n_c \rightarrow m_v$, etc.).) Figure 2.1 is an energy level diagram representing the thermoluminescence energy storage mechanism. The energy difference between the electron trap and the conduction band, E_t, is referred to as the activation energy or trap depth. The electron will remain trapped until excited with sufficient energy to be released back into the conduction band. Heating the material can provide enough thermal energy to overcome the potential well of the electron trap. The energy transferred to the trapped electron is given by

$$E_t \approx 25kT \tag{2.1}$$

where k is Boltzmann's constant (eV K^{-1}) and T (K) is the temperature of the material. The thermally released electron can become trapped again or recombine with a trapped 'hole'. Recombination with a trapped hole causes the luminescence center to become excited into a higher energy level. Relaxation of the luminescence center to the ground state energy level results in the emission of a photon, whose wavelength is related to the difference between the excited state(s) and ground state energy levels of the luminescence center by

$$E = hc/\lambda \tag{2.2}$$

13
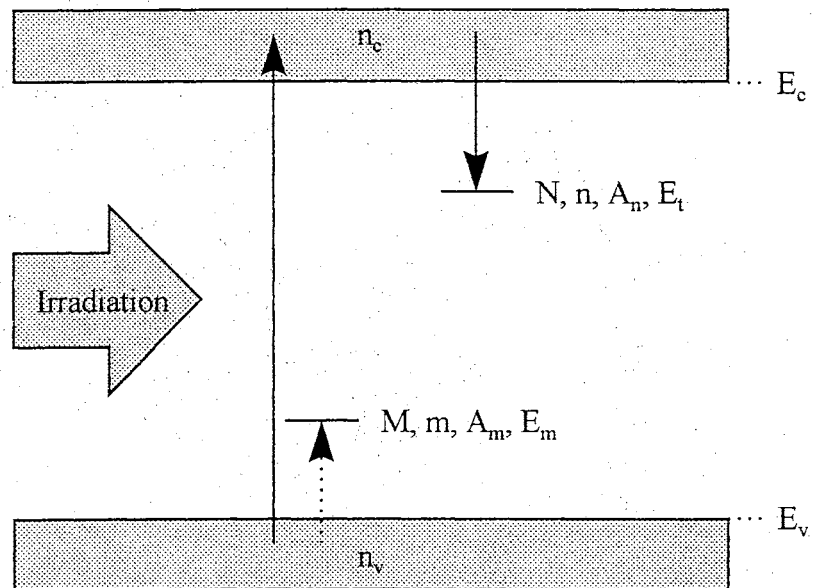
Figure 2.1 - Energy Level Diagram of TL Energy Storage. Solid arrows represent electron transitions, while dotted arrows represent hole transitions.

where h is Planck's constant (eV s), c is the speed of light in a vacuum (m s⁻¹) and λ is the wavelength of the photon (m). Figure 2.2 is an energy level diagram representing the thermoluminescence energy release mechanism. A plot of the resulting luminescence intensity with respect to the material temperature produces a TL 'glow peaks'. A TL 'glow curve' is, in turn, comprised of one or more TL glow peaks.

The TL glow peaks are a result of the combined effect of increasing the temperature of the sample. As the temperature is increased, the probability of releasing trapped electrons increases. At the same time, an increase in free electrons increases the probability of recombination with trapped holes. However, at some point, the trapped electron concentration will begin to decrease. Thus, while the detrapping rate increases, the luminescence will increase; however, as soon as the detrapping rate begins to decrease, the luminescence will decrease. The product of these two processes, as will be shown, produces the characteristic TL glow peak.

The lifetime, τ, of the electron in the trap is related to the temperature, T, of the material and the energy of the trap by

$$\tau = s^{-1}\exp\{E/kT\} \tag{2.3}$$

where s is a constant (s⁻¹) (often referred to as the 'attempt-to-escape frequency'). Alternatively, the probability p per unit time (i.e. $p = \tau^{-1}$) for thermal excitation from the trap is given by

$$p = s\exp\{-E/kT\} \tag{2.4}$$

15
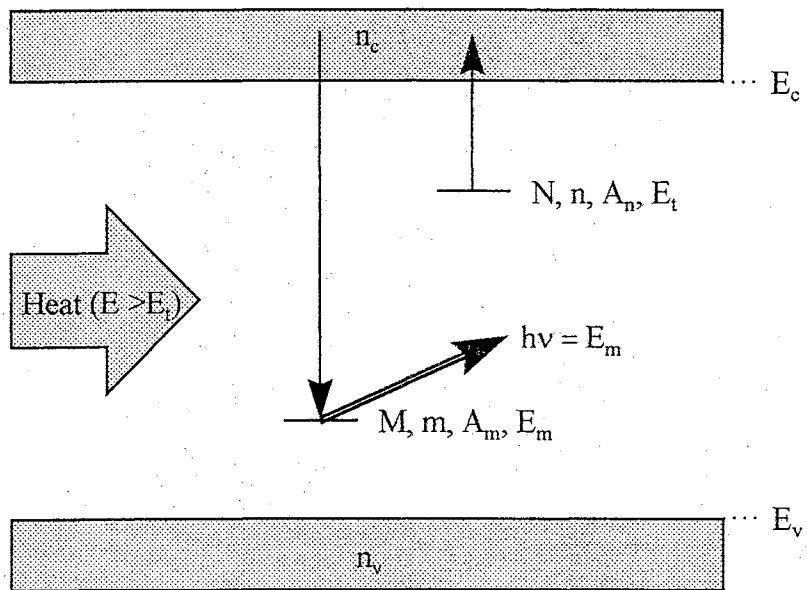
Figure 2.2 - Energy Level Diagram of TL: Energy Release. Smaller, solid arrows represent electron transitions. Larger arrow represents photon emission resulting from electron-hole recombination.

The rate equations which describe the flow of charge into and out of the delocalized bands during heating are, from Chen and McKeever[77]:

$$\frac{dn_c}{dt} = ns\exp\left\{\frac{-E_t}{kT}\right\} - n_c(N-n)A_n - n_c m A_{mn} \tag{2.5}$$

$$\frac{dn_v}{dt} = 0 \tag{2.6}$$

$$\frac{dn}{dt} = n_c(N-n)A_n - ns\exp\left\{\frac{-E_t}{kT}\right\} \tag{2.7}$$

$$\frac{dm}{dt} = -n_c m A_{mn} \tag{2.8}$$

The concentrations are defined as follows: n_c – free electrons in the conduction band, n_v – free holes in the valence band, n – trapped electrons, m – holes available for recombination and N - n – empty traps. The transition coefficients (m^3 s^{-1}) are: A_n – the retrapping probability and A_{mn} – the recombination probability. The transition coefficients, A_n and A_{mn}, are equal to the product of the free electron thermal velocity and the capture cross-sections for the retrapping and recombination, respectively, of free carriers.

From Randall and Wilkins[74], the rate of thermal excitation from level 1 back to the conduction band is

$$-dn/dt = np = ns\exp\left\{-E/kT\right\} \tag{2.9}$$

where the negative sign signifies a loss of electrons from level 1. Restricting this discussion to first-order kinetics (i.e. the probability of recombination is much greater than the

probability of retrapping), the intensity of phosphorescence, $I(t)$, is proportional to the rate

of release of trapped electrons from level 1 and is given by

$$I(t) = \eta\{-dn/dt\} = \eta n s \exp\{-E/kT\} \qquad (2.10)$$

where η is the radiative efficiency. The radiative efficiency is 1 when all recombinations

produce photons and all photons are detected. Integrating, Eq. (2.10) becomes

$$I(t) = \eta I_0 \exp\{-tp\} \qquad (2.11)$$

where I_0 is the intensity at time $t = 0$.

Charge neutrality considerations dictate that

$$n_c + n = m \qquad (2.12)$$

and, consequently

$$\frac{dn_c}{dt} = \frac{dm}{dt} - \frac{dn}{dt}. \qquad (2.13)$$

The intensity of the TL emitted during the heating stage is determined by the rate of

recombination and can be summarized by

$$I_{TL} = -\eta \frac{dm}{dt}. \qquad (2.14)$$

Equations (2.5)–(2.8) are coupled, non-linear differential equations which represent

the exchange of electrons during the heating stage of a system initially perturbed from

equilibrium. The concentrations are all functions of time and temperature and the

equations are analytically insoluble unless simplifying assumptions are introduced. The

18

most significant simplifying assumption requires the free electron concentration in the conduction band to remain relatively constant. This quasiequilibrium (QE) assumption

$$\left| \frac{dn_c}{dt} \right| \approx 0 \qquad (2.15)$$

allows the rate equations (2.5)–(2.8) to be simplified, since

$$\frac{dn}{dt} \approx \frac{dm}{dt} = I_{TL}. \qquad (2.16)$$

Substitution of Eqs. (2.4) and (2.10) into Eq. (2.11) yields

$$I(t) = n_0 s \exp\left\{\frac{-E_t}{kT}\right\} \exp\left\{-s \int_{t_0}^{t} \exp\left\{\frac{-E_t}{kT}\right\} dt\right\} \qquad (2.17)$$

If the sample is heated at a linear rate, $\beta = dT/dt$, such that $T(t) = T_0 + \beta t$, then

$$I(t) = n_0 s \exp\left\{\frac{-E_t}{kT}\right\} \exp\left\{-s \int_{t_0}^{t} \exp\left\{\frac{-E_t}{kT}\right\} dt \frac{dT}{dt} \frac{dt}{dT}\right\}$$

$$I(t) = n_0 s \exp\left\{\frac{-E_t}{kT}\right\} \exp\left\{-\left(\frac{s}{\beta}\right) \int_{T_0}^{T} \exp\left\{\frac{-E_t}{k\Theta}\right\} d\Theta\right\} \qquad (2.18)$$

where n_0 is the initial number of trapped electrons at T_0 (i.e. $t = 0$) and is proportional to the absorbed energy. Θ is a dummy variable representing temperature. Eq.(2.18) is the Randall-Wilkins[74] equation for the shape of a first-order TL glow curve. Figure 2.3 (curve a) is a computer-generated first-order TL glow curve ($E_t = 1.5$ eV, $s = 10^{14}$ s^{-1}), which was produced by numerically integrating Eq. (2.18). Also shown in Figure 2.3 are the detrapping probability (curve b) and the trapped electron concentration (curve c) components of the TL glow curve.
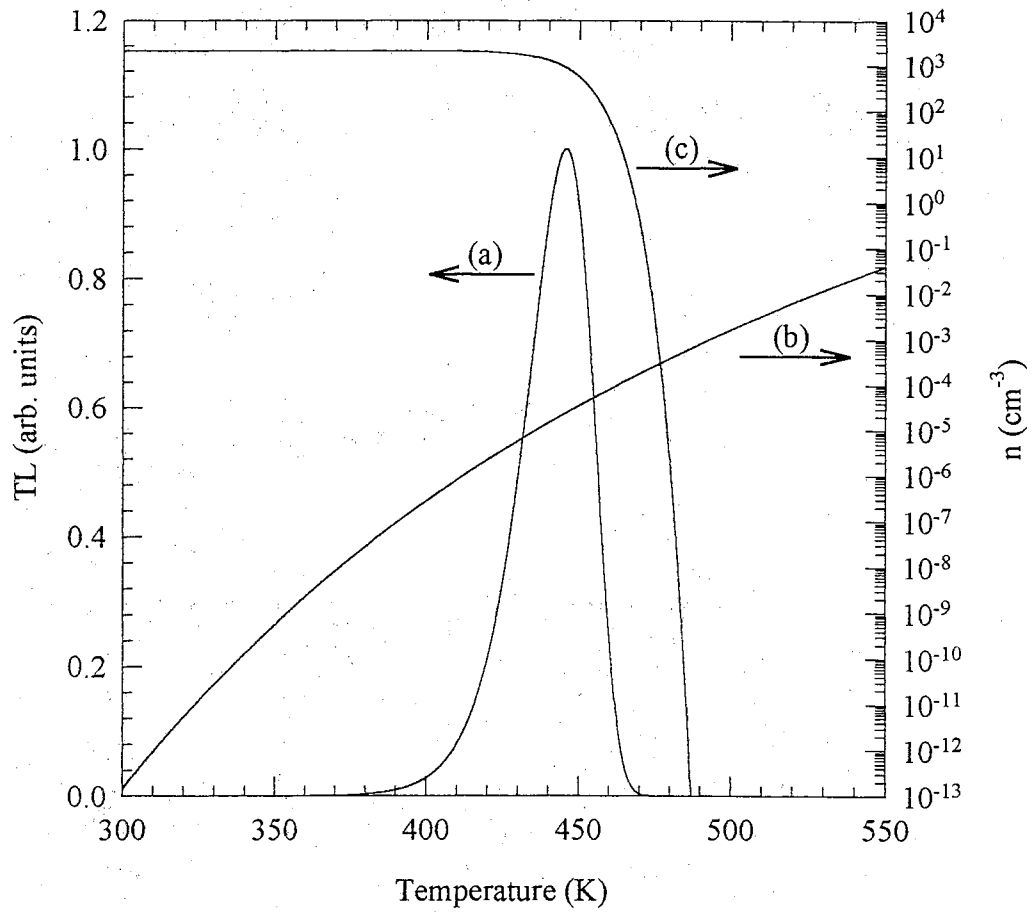
Figure 2.3 - Computer-Generated First-Order TL Glow Curve. Intensity of TL glow peak calculated using the Randall-Wilkins equation, with E_t = 1.5 eV and s = 10^{14} s^{-1}.

Curve b represents the increasing probability of releasing trapped electrons as the temperature is increased (rising side of TL glow peak), while curve c represents the decreasing probability of having trapped electrons to release (falling side of TL glow peak) due to a decrease in the concentration of trapped electrons.

Randall and Wilkins[75] also developed a theory based upon the equivalent rates of retrapping and recombination. This second-order kinetics model was later developed further by Garlick and Gibson[76]. By considering equivalent rates of retrapping and recombination, Eq. 2.10 becomes

$$I(t) = -\eta \frac{dn}{dt} = \alpha n^2 \tag{2.19}$$

where α is a constant at constant T. Integration of Eq. 2.19 now yields

$$I(t) = \frac{I_0}{(n_0 \alpha t + 1)^2}. \tag{2.20}$$

Now, with the assumptions that $m\sigma_{mn} \ll (N - n)\sigma_n$ (i.e. retrapping dominates over recombination), $N \gg n$ and $n = m$, we have (from Chen and McKeever[77])

$$I_{TL} = -\frac{dn}{dt} = s\left(\frac{\sigma_n}{N\sigma_{mn}}\right) n^2 \exp\left\{-\frac{E_t}{kT}\right\}. \tag{2.21}$$

The final assumption that $\sigma_n = \sigma_{mn}$ yields, upon integration of Eq. 2.21,

$$I_{TL} = \left(\frac{n_0^2}{N}\right) s \exp\left\{-\frac{E_t}{kT}\right\}\left[1 + \left(\frac{n_0 s}{\beta N}\right)\int_{T_0}^{T} \exp\left\{-\frac{E_t}{k\Theta}\right\}d\Theta\right]^{-2}. \tag{2.22}$$

Equation 2.22 is the Garlick-Gibson equation for the shape of a second-order TL glow curve.

The Randall-Wilkins expression (Eq.2.18) is considered first-order since $dn/dt \propto n$. The Randall-Wilkins expression for TL produces asymmetric peaks, as shown in Figure 2.3. The asymmetry of the peak is a characteristic feature of first-order kinetics, whereas second-order kinetics (as developed by Garlick and Gibson[76], in which $dn/dt \propto n^2$) will produce peaks which are more symmetrical. The peak position of first-order peaks depends on the combination of activation energy and 'attempt-to-escape' frequency factor, while the peak height scales with n_0. On the other hand, second-order kinetics predict that the glow peak will shift to lower temperature as n_0 increases.

First-order kinetics expressions for thermally stimulated conductivity (TSC) and TL have been derived without the quasiequilibrium approximation[78–80]. Lewandowski and colleagues abandoned the QE and kinetic-order (KO) assumptions of Randall-Wilkins and Garlick-Gibson. The QE assumption was replaced with the physically meaningful function $Q(T)$, which is defined as the degree to which QE is maintained; similarly, the KO assumption was replaced by the $P(T)$ function, which is defined as the degree of retrapping.

Thus, instead of the QE assumption (Eq. 2.15), the Q function is given by

$$-\frac{dn_c}{dt} = q\frac{dm}{dt} \tag{2.23}$$

and

$$Q\frac{dm}{dt} = \frac{dn}{dt} \tag{2.24}$$

where $Q = q + 1$. As a result, QE would require $Q \approx 1$ (i.e. $q \approx 0$).

The KO assumption is replaced by the P function, which is defined by

$$P(T) = \frac{(N-n)\sigma_n}{m\sigma_{mn}}.$$ (2.25)

Thus, slow-retrapping requires $P \ll 1$, while fast-retrapping is given by $P \gg 1$.

The introduction of these parameters allows the degree of adherence to the QE and KO concepts to vary with temperature. This is in contrast to the assumptions made by Randall-Wilkins and Garlick-Gibson, which were required to be fixed for all temperatures.

Defining the rate of recombination, R_{recom}, as

$$R_{recom} = -\frac{dm}{dt} = n_c v_n \sigma_{mn} m,$$ (2.26)

the rate of thermal excitation, R_{ex}, as

$$R_{ex} = ns\exp\left\{-\frac{E_t}{kT}\right\}$$ (2.27)

and the rate of recapture, R_{recap}, as

$$R_{recap} = n_c(N-n)v_n\sigma_n$$ (2.28)

allows the following relationships for the Q and P functions to be written:

$$Q = \frac{1}{R_{recom}}(R_{ex} - R_{recap})$$ (2.29)

and

$$P = \frac{R_{recap}}{R_{recom}}.$$ (2.30)

As a result of these definitions, the relationship between Q and P can be written as

23

$$Q + P = \frac{R_{ex}}{R_{recom}} \qquad (2.31)$$

and

$$\frac{Q}{P} = \frac{R_{ex}}{R_{recap}} - 1. \qquad (2.32)$$

From these definitions of the Q and P functions, Lewandowski and colleagues developed (within the confines of the chosen model) a perfectly general equation for TL, which assumes neither QE nor a particular KO. The TL intensity can thus be rewritten as

$$I_{TL} = n_0 \left(\frac{s}{Q+P} \right) \exp\left\{ -\frac{E_t}{kT} \right\} \exp\left[-\frac{1}{\beta} \int_{T_0}^{T} \left(\frac{Q}{Q+P} \right) s \exp\left\{ -\frac{E_t}{k\Theta} \right\} d\Theta \right]. \qquad (2.33)$$

This general equation easily reduces to the Randall-Wilkins equation (Eq. 2.18), by substituting $Q \approx 1$ and $P \ll 1$. However, $Q \approx 1$ and $P \gg 1$ does not obviously reduce to the Garlick-Gibson equation (Eq. 2.22).

TL is a particularly useful method for studying deep levels within a semiconductor's or insulator's band gap given the wide variety of analysis methods available. These methods, have been developed to extract trapping parameters such as 'attempt-to-escape' frequency factors and activation energies and include the initial rise technique of Garlick and Gibson[76], Hoogenstraaten's heating rate method[81], Chen's peak shape method[82], computer-aided curve fitting. Keating approximated Eq. 2.18 using an asymptotic series, which produced a closed-form expression[83] given by

$$I_{TL} = n_0 s \exp\left\{ -\frac{E_t}{kT} \right\} \exp\left[-\frac{ksT^2}{\beta E_t} \left(1 + \frac{(b-4)kT}{E_t} \right) \exp\left\{ -\frac{E_t}{kT} \right\} \right]. \qquad (2.34)$$

24

The 'attempt-to-escape' frequency factor is assumed to be proportional to T^{2-b}, where $0 \leq b \leq 4$. The fitting parameters for this expression are n_0, s, E_t and b.

The simple model described above (i.e. 1 electron trap and 1 recombination center, introduced by Haering and Adams[84] and Halperin and Braner[85]) provides a good basis for understanding TL kinetics, but real materials are much more complicated. A material described by the simple model would have only one TL peak and the emission would be at a single wavelength (unless, of course, several excited energy levels exist for the excited states of the luminescence center), as depicted in Figure 2.3. Normally, a number of peaks are observed and emissions at several wavelengths or over a range of wavelengths are common. One extension to the simple model is the addition of a thermally disconnected trap[86,87]. A thermally disconnected trap is one in which the trap depth is so great that any carriers trapped at the level are unable to be detrapped at the temperatures reached during the measurement. Chen et al.[88], found that the kinetics tended towards first-order when the number of carriers trapped in thermally disconnected traps was much greater than the number of trapped carriers at the non-thermally disconnected trap (i.e. the shallow trap). When the number of carriers in the shallow trap was much greater than the number in the thermally disconnected trap the kinetics were second-order.

2.3   Phototransferred Thermoluminescence

PTTL is the thermoluminescence resulting from the optically-induced excitation (and subsequent transfer) of charge from deeper, populated traps to shallower traps. Typically, the induction of a PTTL signal involves the pre-irradiation of a sample at a temperature T_{irr}. The sample is then preheated to a temperature T_{ph} to excite charge carriers out of shallower

traps which are thermally unstable at that temperature, while the population of charge carriers in deeper traps remain unaffected. Illumination of the sample at a temperature $T_{ill} < T_{ph}$ will populate any shallower traps which are thermally stable at T_{ill}. Thus, the charge carriers of deeper filled traps are *phototransferred* to shallower traps. Subsequent heating of the sample will produce TL, without any additional irradiation.

2.3.1 A Simple Model

The simplest model to describe the phototransfer mechanism involves the excitation of charge carriers from one deep trap into one shallow trap, with only one recombination center for luminescence, as shown in Figure 2.4. Chen and McKeever[77] have developed a mathematical description of this model. For electron concentrations of n_1 and n_2 in the shallow and deep traps, respectively, and m concentration of holes in the recombination centers, the initial conditions following irradiation and preheat, but prior to illumination, are $n_{10} = 0$ and $n_{20} = m_0$. If f represents the optical excitation rate of electrons from the deep traps, then the rate equations which govern the illumination period are given by

$$\frac{dn_2}{dt} = -n_2 f + n_c (N_2 - n_2) A_2 \tag{2.35}$$

$$\frac{dn_1}{dt} = n_c (N_1 - n_1) A_1 \tag{2.36}$$

$$\frac{dm}{dt} = -n_c m A_m \tag{2.37}$$

where N_1 and N_2 represent the concentration of shallow and deep traps, respectively, A_1, A_2 and A_m are the trapping (shallow (1) and deep (2)) and recombination constants (cm^3 s^{-1}), respectively, and n_c is the concentration of free electrons. All concentrations are in units of

Figure 2.4 - Energy Level Diagram of PTTL: Simple Model. Solid arrows represent electron transitions during illumination.

cm^{-3}. The solutions to the above equations, assuming quasiequilibrium and no re-trapping

into the deep source traps ($n_2 f >> n_c(N_2 - n_2)A_2$), are

$$n_2(t) = n_{20} \exp\{-tf\} \tag{2.38}$$

$$n_1(t) = N_1[1 - \exp\{-Bt\}] \tag{2.39}$$

$$m(t) = m_0 \exp\{-t/\tau\} \tag{2.40}$$

where $B = n_c A_1$ and $\tau = (n_c A_m)^{-1}$. (B and τ are approximately constant if $dn_c/dt \approx 0$, i.e. the

quasiequilibrium approximation is true.) Therefore, after a period of illumination, each of the

traps and recombination centers will have a concentration of charge, subject to the charge

neutrality considerations given by

$$n_c + n_1 + n_2 = m. \tag{2.41}$$

Once the illumination is complete, the sample must be heated in order to produce the

PTTL signal. This phase of the process produces competition among the traps and

recombination centers. Assuming quasiequilibrium and $n_1(t^*) << N_2 - n_2(t^*)$ (i.e. the number

of electrons trapped in the shallow trap is much less than the number of available deep traps),

we have

$$I(t^*) = \frac{C m(t^*) n_1(t^*)}{(N_2 - n_2(t^*))} \tag{2.42}$$

or

$$I(t^*) = \frac{C \exp\{-t^*/\tau\} N_1[1 - \exp\{-Bt^*\}]}{(N_2/n_{20} - \exp\{-t^* f\})} \tag{2.43}$$

for the variation of the PTTL signal due to the shallow trap as a function of the illumination time, t^*.

2.3.2 A More Complex Model

The results of the simple model predict a PTTL versus time curve which increases monotonically from zero to some maximum level. However, some experimental PTTL versus time curves initially increase, reach a maximum and then decrease as the illumination time continues. While this phenomena can be modeled as simply simultaneous optical bleaching of the induced TL signal, a non-radiative recombination center can also explain the observed behavior. Figure 2.5 is an energy level diagram of the new model, first proposed by Bøtter-Jensen et al.[67,89] and discussed at length recently by Chen and McKeever[77], McKeever et al.[90–92], and Alexander et al.[93].

This model includes an additional deep trap (concentration N_3, electron population n_3) and a non-radiative recombination center (concentration M_5, hole population m_5). The additional deep trap is not thermally or optically active, although the high temperature annealing will release any trapped charge, and serves only to provide sensitivity changes. The additional recombination center provides a competing, non-radiative pathway and the resulting charge neutrality of this new model becomes

$$n_c + n_1 + n_2 + n_3 = m_4 + m_5 \tag{2.44}$$

where m_4 is the concentration of the radiative recombination center previously discussed in section 2.3.1.

With this model, PTTL now follows the principles outlined by McKeever[94,95] where the reduction of the PTTL as a result of continued illumination is due to the removal of holes from the radiative recombination centers during illumination. Although the simple model of
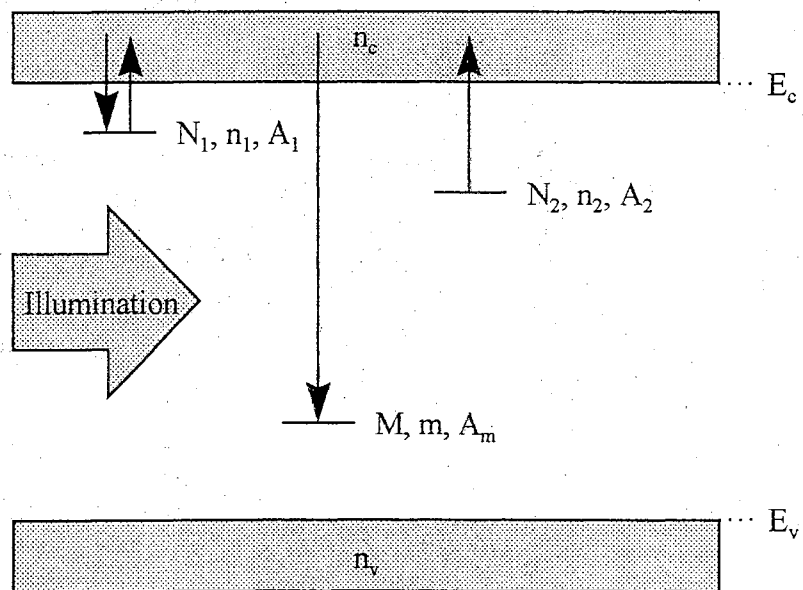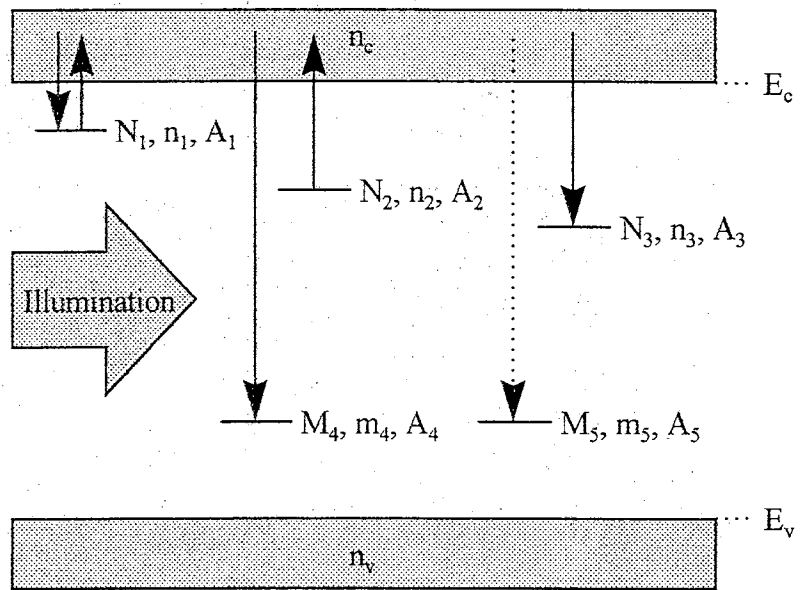
Figure 2.5 - Energy Level Diagram of PTTL: Complex Model. Solid arrows represent electron transitions during illumination. Gray arrow represents electron transitions into non-radiative recombination center.

the previous section produces a similar removal of holes via recombination, the charge neutrality condition of that model (Eq. 2.41) restricts n_1 to values less than (or equal to) m_4. As a result, whenever n_1 is increasing, sufficient holes always exist such that the PTTL signal follows n_1. However, in the present model, the new charge neutrality conditions (Eq. 2.44) allow n_1 to be less than *or greater than* m_4. As a result, while n_1 may be increasing, *sufficient holes may not exist* in the radiative recombination centers to accommodate all of the available electrons – even though the total number of available holes (m_4+m_5) will always be greater than (or equal to) n_1. As a result, n_1 will be less than m_4 at the beginning of the illumination and the PTTL signal will increase with n_1. However, as the illumination progresses, n_1 may become greater than m_4 and the PTTL intensity will decrease with m_4. This effect can be summarized by

$$I_{PTTL} = \min(n_1, m_4),\qquad\qquad (2.45)$$

However, this argument is too simplistic if competition and multiple recombination pathways for the electrons exist. In these cases, the PTTL intensity does not always follow the minimum of n_1 or m_4, and the resultant PTTL intensity must be calculated by solving the appropriate equations numerically[93].

Using this scenario, Alexander et al.[93] have shown a decrease in the PTTL intensity is possible without optical bleaching of the shallow traps. In addition, the steady-state PTTL (following long illumination times) need not be zero. This situation can occur when the source trap electron concentration depletes due to long illuminations (i.e. $n_2 \to 0$ as $t \to \infty$). Thus, a final steady-state value of $m_4 \geq 0$ would yield a PTTL steady-state value ≥ 0, depending upon the relative initial values of n_2 and m_4. These authors have shown numerical solutions to the complex model for PTTL which exhibit increases in the PTTL intensity for

shorter illumination times, followed by decreases after longer times. The curves of PTTL vs.

illumination time vary, depending upon the wavelength of the stimulating light used for

phototransfer. Shorter wavelengths cause both the growth and decay portions of the curve

to change more rapidly than longer wavelengths. The wavelength dependence of the

stimulating light was introduced into these computations by considering an optical excitation

rate of the form

$$f(\lambda) = \sigma_0(\lambda)\,\varphi(\lambda) \tag{2.46}$$

where $\sigma_0(\lambda)$ is the photoionization cross-section (m^2) and $\varphi(\lambda)$ is the photon fluence (photons

m^{-2} s^{-1}). The photoionization cross-section for the excitation of electrons from the deep traps

is assumed to follow that of parabolic delocalized bands, given by

$$\sigma_0 = C\sqrt{E_0}\,\frac{(h\nu - E_0)^{3/2}}{h\nu(h\nu - \gamma E_0)^2} \tag{2.47}$$

where C is a constant, γ is a constant dependent upon the electron effective mass, E_0 is the

optical threshold energy for ionization and $h\nu$ is the photon energy[96].

2.4   Summary

This chapter has focused on the theoretical background of TL and PTTL. This includes

a description of the rate equations for the flow of charge into and out of the delocalized bands

and two models for TL: one, first-order kinetics, which assumes a condition of

'quasiequilibrium' exists within the conduction band and that $m\sigma_{mn} \gg (N-n)\sigma_n$ (slow

retrapping); while the other, second-order kinetics, considers the possibility of the retrapping

and recombination rates being equivalent (fast-retrapping). In addition, two models for PTTL

are described: the simple model, which assumes excitation from one optically active deep trap

into one shallow trap and recombination via a single radiative recombination center; however, the complex model, includes a competing, non-radiative recombination center, as well.

The analysis of the data presented in the balance of this dissertation will focus on the first-order kinetics described by the Randall-Wilkins equation (Eq. 2.18) and the description of the complex model for PTTL (section 2.3.2). In general, these models are used as tools, in order to extract dosimetric information from the data obtained. In most cases, the analysis supports the use of first-order kinetics, rather than second-order kinetics. In fact, some of the data refute claims of other authors as to possible second-order behavior of the main dosimetric peak in α-Al_2O_3:C. However, the validity of the models (and/or their assumptions) are not challenged.

Chapter 3

3 Phototransferred Thermoluminescence in α-Al_2O_3:C

3.1   Introduction

The study of optically induced effects in α-Al_2O_3:C is becoming increasingly important

in view of the strong sensitivity of the TL signal from this material to light[32,54,60,66], and

in view of the potential applications of the material in OSL dosimetry[66]. Understanding

these optically induced effects is important for understanding the TL and OSL properties of

this material. In particular, establishing the optical stimulation spectra, the thermal stability

of the optically sensitive centers and the dependence of these effects on dose is necessary

information in this context, and PTTL is a useful tool in this regard.

Recently, Oster et al.[60] reported stimulation spectra for PTTL in α-Al_2O_3:C for the

phototransfer of charge from deep traps into the so called 'main dosimetry' trap[45,55,71,73].

(The TL peak of the 'main dosimetry peak' appears near 450 K.) Earlier, Akselrod and

Gorelova[54] examined the temperature dependence of the process and established that the

deep traps responsible for the phototransfer effect become unstable at temperatures around

900 K and 1200 K. In this work, these studies are extended to the study of phototransfer to

traps unstable below room temperature, i.e. into traps which yield TL peaks below room

temperature.

3.2 Experimental

The experiments were conducted using TLD-500 α-Al$_2$O$_3$:C samples supplied by Harshaw-Bicron. The samples were 1 mm thick, 5 mm in diameter and unpolished. The light source was a 150 W Xe arc lamp with silica condenser optics. Wavelengths were selected using a GCA/McPherson 0.3 m scanning monochromator. The bandwidth varied between 1.49 nm and 3.90 nm. A fused silica fiber optic guide was used to direct the light on to the sample. The sample was mounted to the planchet using a small amount of vacuum grease to improve thermal contact. The temperature controller provided a linear heating rate of 0.3 K s^{-1}. Light was collected with a model 9635QB Thorn-EMI bi-alkali PMT, which was used in current mode. The illumination power was adjusted to give the same photon flux at the sample, at each wavelength.

Two PTTL peaks were monitored in this experiment, at 265 K and 450 K. The response of the peaks was monitored as a function of illumination time, pre-heat temperature, wavelength and dose. All the irradiations were performed at room temperature using a ^{90}Sr/^{90}Y source. The illuminations were conducted at 190 K for the 265 K peak, and at 340 K for the 450 K peak. In the latter case, the trap responsible for the 450 K peak was first emptied, immediately after irradiation and before illumination, by either heating to 500 K, or by annealing for 5 min at 575 K.

For the illumination time dependence, the sample was pre-irradiation annealed for 15 min at 1175 K and given a dose of 10 Gy. For each PTTL measurement, the sample was illuminated for 10 s with 500 nm light. The experiment was then repeated using different illumination times from 30 s to 3000 s. The whole experiment was then repeated using 400 nm and 300 nm light. The power was adjusted at each wavelength to maintain a constant

35

photon flux of 3.3×10^{13} photons s^{-1} cm^{-2} at the sample. Typical powers used were in the range of 50 μW to 250 μW. Preliminary measurements showed that, for the doses used in this experiment, such low powers and short illumination times do not significantly deplete the source of the phototransferred charge. Therefore, all measurements, at a given wavelength, were performed from the same initial irradiation.

For the pre-heat temperature dependence, the same procedures were used, except that each sample was pre-heated to a temperature T_{ph} for 2 min, before being illuminated for 2 min with 300 nm or 500 nm light at a constant photon flux of 6.6×10^{14} photons s^{-1} cm^{-2} at the sample. The experiment was repeated several times for pre-heat temperatures varying from room temperature to 1175 K (675 K, for the measurement using 500 nm light). As before, all measurements were performed from the same initial irradiation. For the 265 K PTTL peak, the experiment was performed with 300 nm and 500 nm light; for the 450 K PTTL peak, only 300 nm light was used.

For the wavelength dependence, the same procedures used in the illumination time experiment were adopted, except that each sample was illuminated for a fixed time of 1 min with light of a given wavelength. The experiment was repeated, changing the wavelength each time in increments of 10 nm, from 250 nm up to 700 nm (for the low temperature PTTL peak) or up to 450 nm (for the main dosimetric PTTL peak). The power was adjusted at each wavelength to maintain a constant photon flux of 1.2×10^{14} photons s^{-1} cm^{-2} at the sample. As before, all measurements were performed from the same initial irradiation.

For the dose dependence, the sample was pre-irradiation annealed for 15 min at 1175 K, irradiated, and illuminated for 1 min with 300 nm light. The sample was then re-annealed and the process repeated, for doses ranging from 64 mGy to 40 Gy. For the low

temperature PTTL peak, the experiment was repeated with 500 nm light. The power was adjusted at each wavelength to maintain a constant photon flux of 6.6×10^{14} photons s^{-1} cm^{-2} at the sample.

3.3   Results

Figure 3.1 represents a typical glow curve for α-Al_2O_3:C obtained by irradiating a sample at 80 K with 10 mGy from a ^{137}Cs source and heating at a rate of 0.3 K s^{-1}. Three peaks are observed – which we label peaks 1, 2 and 3 – at temperatures of ~265 K, ~310 K and ~450 K, respectively. Peak 3 is the 'main dosimetric peak'. Figure 3.2 shows the relationship between the 265 K and 450 K PTTL peaks with respect to illumination time. The data show that the PTTL signals are linear up to 3000 s, indicating a lack of significant source trap depletion at these illumination times (in agreement with the observations by Oster et al.[60]). In addition, the relatively short illumination times used are not sufficient to test the PTTL theory of Chapter 2, which predict a linear rise for short illumination times and reaching a plateau for very long illuminations.

Figure 3.3 displays the relationship of the PTTL signal with respect to the preheat temperature. At 500 nm, the 265 K trap appears to receive most charge carriers from the 450 K trap (with only ~0.1% stemming from deeper traps). However, at 300 nm, the 265 K trap appears to receive charge carriers from the 450 K trap, as well as from deeper traps which become unstable near 900 K and 1200 K. Similarly, the 450 K trap also appears to receive charge carriers from both the 900 K and 1200 K traps, but there is also a reduction in the PTTL efficiency as the temperature increases past ~550 K. A weak TL peak has often been reported here and is believed to be related to the presence of Cr[97].
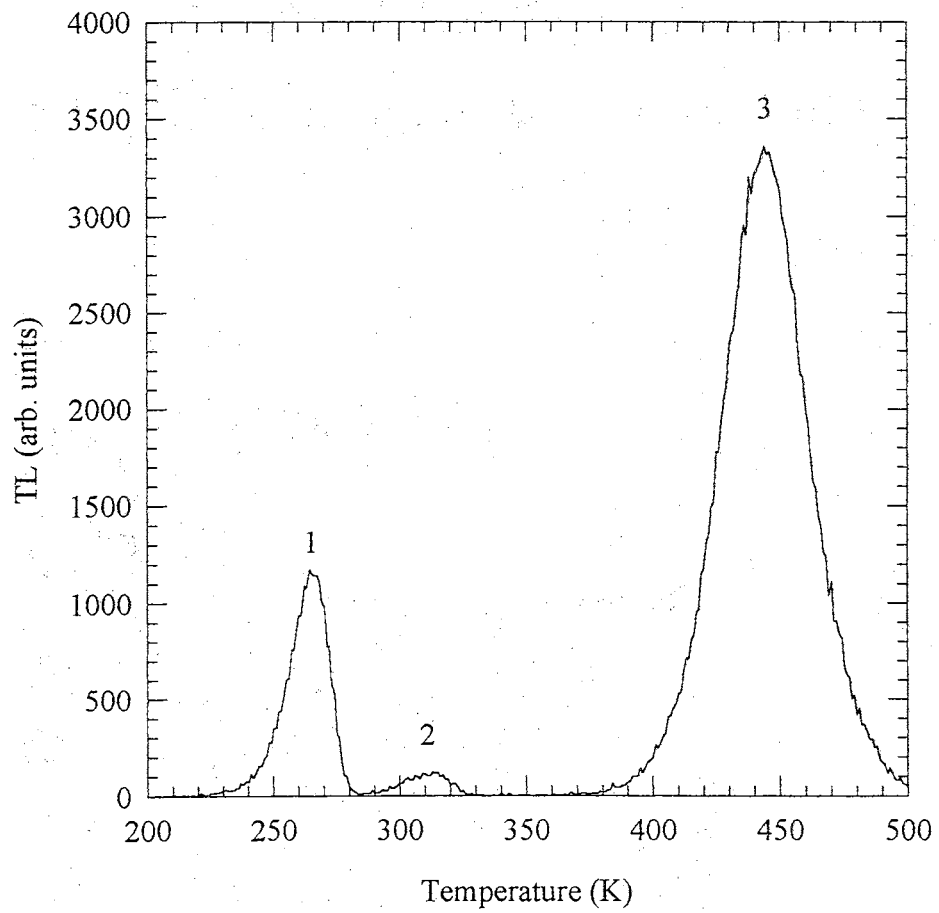
Figure 3.1 - Typical TL Glow Curve for α-Al$_2$O$_3$:C. Dose of 10 mGy ^{137}Cs delivered at 80 K and heated at 0.3 K s.$^{-1}$ The three main peaks are labeled peak 1 (265 K), peak 2 (310 K) and peak 3 (450 K).

Figure 3.2 - PTTL as a Function of Illumination Time. Dose of 10 Gy ^{90}Sr/^{90}Y delivered at room temperature and heating at 0.3 K s.$^{-1}$ The illumination was at 190 K with a photon flux of 3.3 x 10^{13} photons s^{-1} cm^{-2}. Filled circle - 500 nm (265 K); filled square - 400 nm (265 K); filled triangle - 300 nm (265 K); filled inverted triangle - 300 nm (450 K).
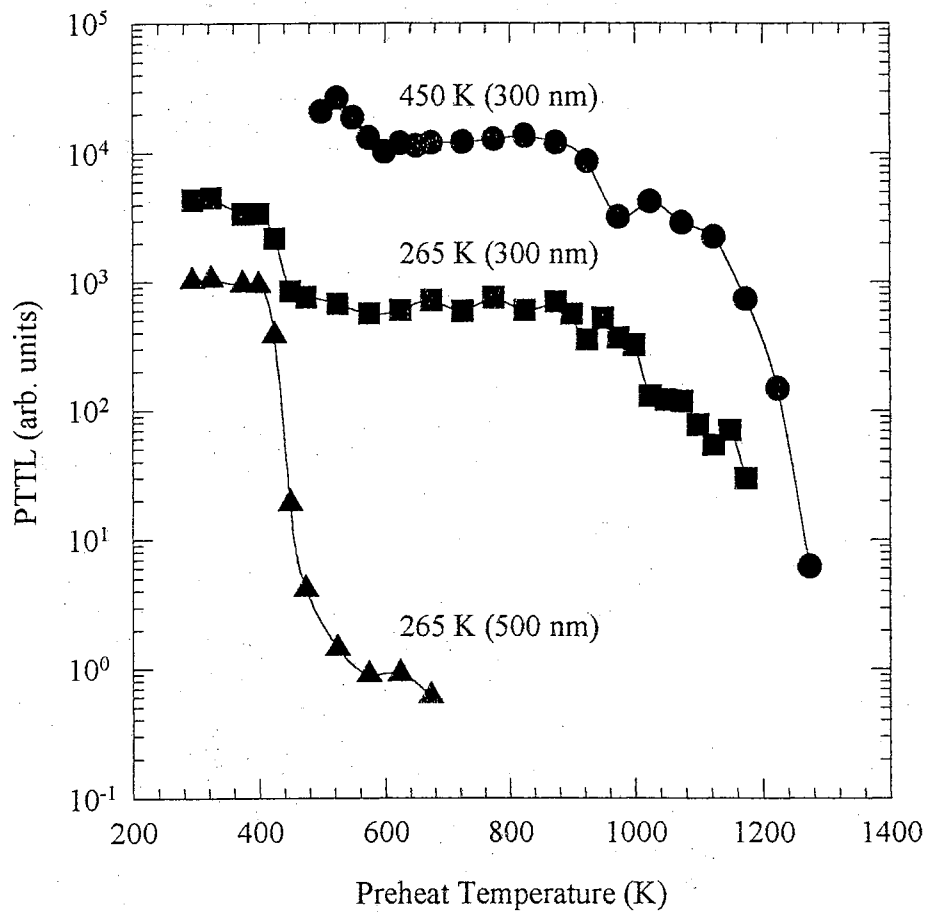
Figure 3.3 - PTTL as a Function of Preheat Temperature. Dose of 10 Gy ^{90}Sr/^{90}Y delivered at room temperature and heated at 0.3 K s^{-1}. The illumination was at 190 K for 1 min with a photon flux of 6.6 x 10^{14} photons s^{-1} cm^{-2}. The sample was preheated for 2 min between irradiation and illumination. Filled circle - 450 K peak at 300 nm (40 Gy dose); filled square - 265 K peak at 300 nm (10 Gy dose); filled triangle - 265 K peak at 500 nm (10 Gy dose).

Figure 3.4 shows the relationship of the PTTL signals with respect to illumination wavelength. The most effective wavelengths are in the short wavelength visible to UV range. Several features can be seen in the stimulation spectrum, including a maximum for all curves at approximately 280 nm. For peak 1 there are stimulation bands centered at approximately 340 nm and 420 nm. The stimulation spectrum for peak 2 is almost identical to that of peak 1, namely a maximum at 280 nm and a shoulder at 340 nm. In addition, even after pre-heating to a temperature of 975 K, the stimulation spectrum of the 450 K PTTL peak remains the same as that observed without the pre-heat.

Figure 3.5 represents the variation of the PTTL signals with pre-dose. The data show that the PTTL signal is slightly supralinear with dose in the range of 6 mGy to 40 Gy.

One interesting aspect of the experiments concerns the position and shape of the PTTL peaks with respect to those of the TL peaks. For peak 1, the shape and position of the PTTL peak are identical to those of the TL peak under all conditions examined. However, for peak 3, the PTTL peak position varies, depending upon the exact conditions of dose and pre-heat temperature. In particular, the PTTL peak is observed at ~448 K following either low doses or after pre-heating the sample to temperatures >900 K, in agreement with the results of Oster et al.[60]. However, if the dose is high, and the sample has not been pre-heated to >900 K, the PTTL peak appears at ~455 K.

3.4   Discussion

The wavelength dependence data shown in Figure 3.4 demonstrate that charge transfer takes place from a number of traps of different optical trap depths. The 265 K PTTL peak shows stimulation maxima at ~280 nm, ~340 nm and ~420 nm. The 450 K peak, on the
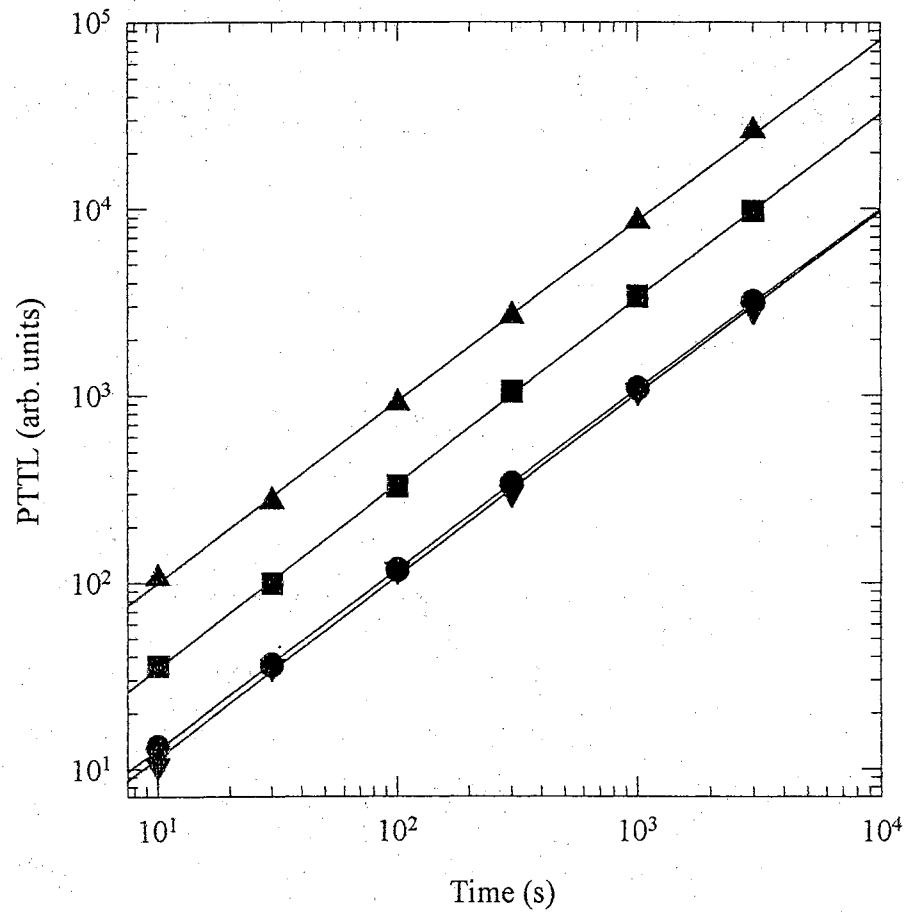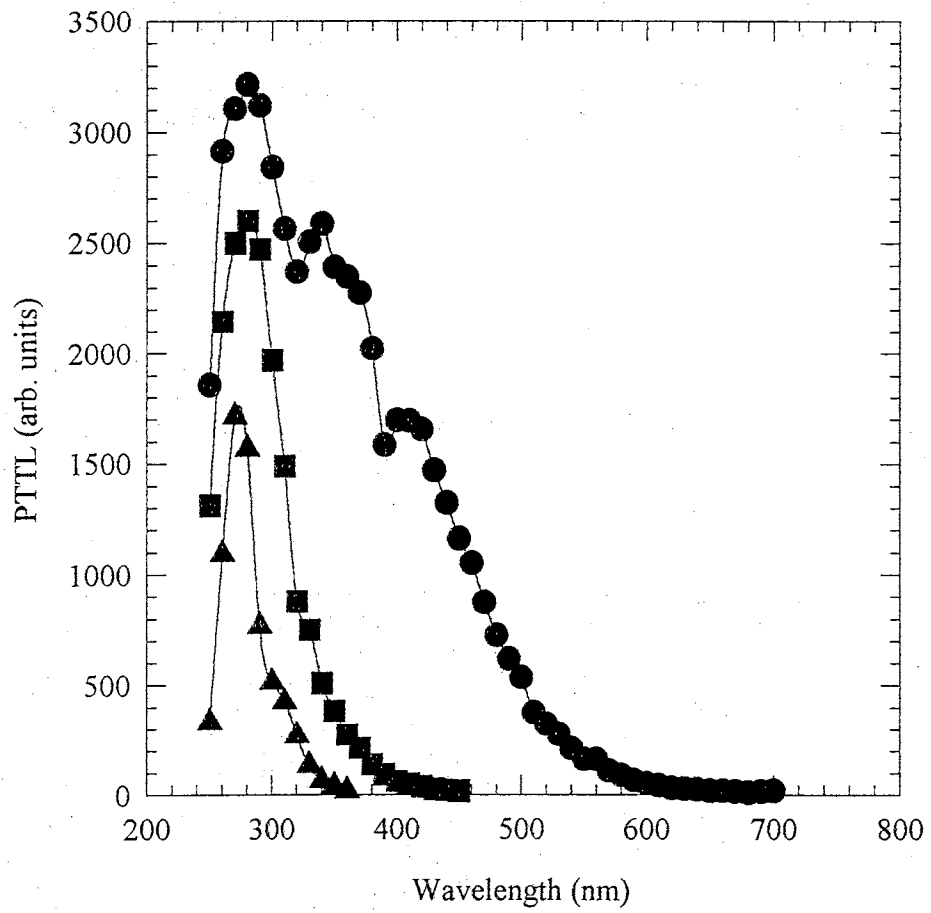
Figure 3.4 - PTTL as a Function of Illumination Wavelength. Dose of 40 Gy ^{90}Sr/^{90}Y delivered at room temperature and heated at 0.3 K s^{-1}. The illumination was at 190 K for 1 min with a photon flux of 1.2 x 10^{14} photons s^{-1} cm^{-2}. Filled circle - 265 K peak; filled square - 450 K peak; filled triangle - 450 K peak after a preheat to 975 K.
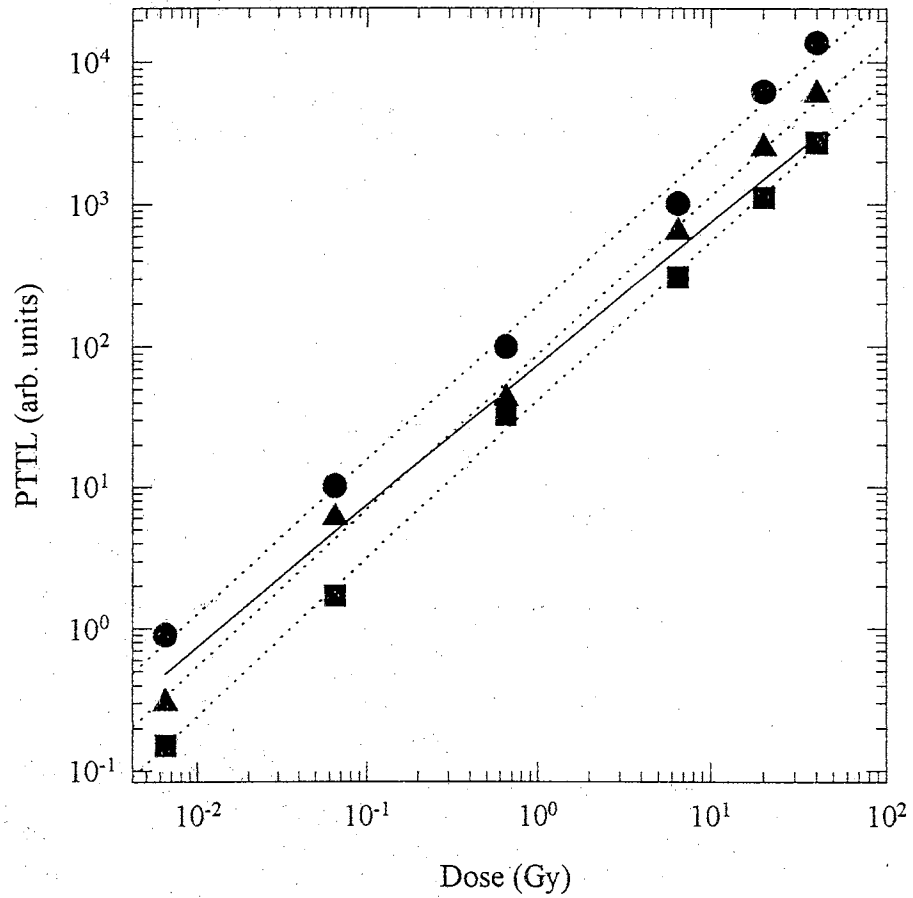
Figure 3.5 - PTTL as a Function of Absorbed Dose. Absorbed dose of $^{90}Sr/^{90}Y$ delivered at room temperature and heated at 0.3 K s^{-1}. The illumination was at 190 K for 1 min with a photon flux of 6.6 x 10^{14} photons s^{-1} cm^{-2}. Filled circle - 300 nm (265 K); filled square - 500 nm (265 K); filled triangle - 300 nm (450 K); full lines - regressions; dashed line - line of linearity.

other hand, shows stimulation maxima at ~280 nm, but only a weak shoulder at ~340 nm. An important observation is that the stimulation spectrum for the 450 K PTTL is the same for pre-heat temperatures <900 K as it is for temperatures >900 K. This suggests that the stimulation spectrum represents the optical trap depth of the deep, 1200 K traps. As a result, the stimulation bands at 280 nm and 340 nm appear to correspond to the release of charge from the 1200 K trap. Stimulation spectra for OSL were reported earlier, albeit over a much narrower wavelength range[61]. Over the same range, the spectra reported here for the 265 K PTTL peak agree well with the reported OSL data and support the view that the OSL signal results from the phototransfer of charge from the same traps.

The temperature stability of the deep traps involved in the phototransfer process may be inferred from Figure 3.3. When shorter wavelength light is used in the phototransfer process, deep traps can be accessed. These deep traps contribute to both the 265 K and the 450 K PTTL signals, and become thermally unstable at temperatures of ~550 K, ~900 K and ~1200 K. The latter two traps have been identified by Akselrod and Gorelova[54] as a hole trap and an electron trap, respectively. The 550 K trap has been suggested to be a hole trap[97]. In addition to the deep traps, the trap at 450 K is also observed to contribute to the PTTL at 265 K. Indeed, when longer wavelength light is used, such that the deep traps cannot be probed, the 450 K trap is seen to contribute >99% of the PTTL to the 265 K trap. Taken together, Figures 3.3 and 3.4 clearly demonstrate the potential of selectively probing different traps using different wavelengths and this leads to advantages when using OSL as a dosimetric method[61,66].

The trap responsible for the 265 K peak has been identified as an electron trap[24,25]. Attempts at peak fitting, using standard TL equations, suggest that a single trap is responsible

for this peak, exhibiting classic Randall-Wilkins, first order behavior. The lack of a shift in the PTTL peak independent of the conditions of the experiment, and the agreement between the position and shape of the PTTL peak and the TL peak induced at this temperature all support this view.

Similar attempts to fit the peak at 450 K, however, suggest an overlap of several peaks, or even a distribution of trapping levels. This view is supported by the alteration in the shape and position of both the TL and the PTTL peaks, dependent upon the dose and thermal history of the sample (as will be shown in Chapter 4). Furthermore, the TL peak at 450 K of Mg-doped samples emits primarily at 420 nm on the low temperature side, and primarily at 330 nm on the high temperature side[24]. The former is usually described as originating from e^-–F^+-center recombination, whereas the latter is thought to result from h^+–F-center recombination[25]. Possible explanations of these observations include a distribution of hole states thermally unstable at these temperatures. The released holes may recombine with F-centers, thereby producing excited F^+-centers. Energy transfer from the F^+- to F-centers may then occur, yielding emission at both 330 nm and 420 nm. Note that excited F-centers are thermally unstable at these temperatures and this process would also result in F-center ionization and the emission of electrons. Alternatively, the 450 K peak may be considered to be a composite of both electron and hole traps, with the electron traps dominating at the low temperature side of the peak, and hole traps dominating at the high temperature side. The shifts in position and changes in shape of the overall peak are then explained as changes in the ratios of the component peaks as a function of dose, dose history, and thermal history. (This idea of a distribution of traps responsible for the observed TL signal will be discussed in detail in Chapter 6.)

Although the current data do not lead to any resolution of these different views of the TL process in α-Al_2O_3:C, they do indicate the importance of both electrons and holes in the phototransfer processes. Furthermore, they highlight the fact that several traps, with different optical trap depths, are involved in the transfer process and by selecting particular wavelengths one can probe these traps separately. This has relevance to the use of this material in optically stimulated luminescence dosimetry[61,66].

Chapter 4

4   Light-Induced Fading of Thermoluminescence from α-Al$_2$O$_3$:C

4.1   Introduction

One potential limitation in the use of α-Al$_2$O$_3$:C for dosimetry is the reported sensitivity of this material to light. The light sensitivity of this material occurs in three ways: (a) the generation of a TL signal in unirradiated samples[59], resulting from the absorption of light by oxygen-vacancy centers (F- and F$^+$-centers) which generates free charge carriers[25]; (b) the phototransfer of charge from deep states to shallower states, giving rise to a PTTL signal[54,60,65] and (c) a light-induced fading of the TL signal.

A number of groups[32,56,57,59,98,100] have previously studied the light-induced fading of this material using fluorescent and incandescent light sources. The only detailed studies of the wavelength dependence of this effect are a suggestion[56] that yellow light appears to be less effective than unaltered fluorescent and incandescent light, and an observation[100] that red light is less effective than light of shorter wavelengths.

In this chapter, the results of a detailed study of the wavelength dependence of the light-induced fading of the TL signal from α-Al$_2$O$_3$:C are presented. Samples which had been annealed at 1175 K for 15 min after TL readout and prior to the next irradiation, and samples which were reirradiated after TL readout but without an annealing sequence were both studied in order to monitor the simultaneous effects of fading and phototransfer.

4.2   Experimental Details

The samples used in these studies were TLD-500 single crystals from Bicron-NE (formerly Harshaw/Bicron, U.S.A.) grown at the Urals Polytechnical Institute. All samples were given an initial anneal at 1175 K for 15 min. Thereafter, two irradiation-illumination readout-annealing sequences were adopted. In the first sequence, we irradiate using a $^{90}Sr/^{90}Y$ beta-particle source at room temperature, illuminate at a fixed wavelength for a given time, readout the TL signal and then anneal at 1175 K for 15 min in air. The sequence was repeated using a different illumination wavelength. These samples are referred to as the 'annealed' samples. The other sequence adopted was as described above, but without the annealing at 1175 K for 15 min. These are referred to as the 'unannealed' samples.

Two sets of TL apparatus were used: one at Oklahoma State University (OSU), U.S.A. and the other at Risø National Laboratory, Roskilde, Denmark. At OSU the illumination of the sample was achieved using a 150 W Xe lamp and a GCA/McPherson 218 monochromator (equipped with a 1200 lines/mm grating blazed at 300 nm and with a dispersion of 2.65 nm/mm). The light was directed through a silica fiber cable and silica lens onto the sample in the TL cryostat. Efforts were made to ensure that the photon flux (i.e. the number of photons per unit area per unit time) incident on the sample was approximately the same at all wavelengths. This was done by adjusting the output slit widths of the monochromator (between 0.05 nm and 2.0 nm) at each wavelength used. The widest bandwidth used was 5.3 nm. The wavelength range used in the measurements was from 300 nm to 600 nm. The power was measured using a Newport Research model 815 power meter with model 818-UV silicon photodetector. The power was varied to maintain a constant photon flux of 1.73 x 10^{12} photons s^{-1} cm^{-2} at the surface of the sample. The TL

48

measurements were performed in a nitrogen atmosphere at a partial vacuum of 600 torr. The emission was detected using an EMI 9635QB photomultiplier tube at ambient temperature in the integrated current mode. No filters were used for the TL output. In all cases the heating rate was approximately 2.0 K s^{-1}. The irradiation dose was 0.1 Gy, unless otherwise noted.

Similar measurements were also made at the Risø National Laboratory, using the Risø automatic TL/OSL reader. This system was equipped with a 75 W tungsten halogen lamp (with a color temperature of 3350 K) as an illumination source, and a monochromator with a linear graded interference filter to obtain different illumination wavelengths[101]. The system does not allow for the adjustment of the illumination power. As a result, the time of illumination was adjusted to give the same incident energy (250 mJ) at each wavelength used. The wavelength range was from 425 nm to 650 nm. The irradiation dose was 70 mGy from a ^{90}Sr/^{90}Y beta source. A heating rate of 2.0 K s^{-1} was used during TL readout. A Hoya U-340 filter was used for the TL output.

All samples were pre-annealed at 1175 K for 15 min. Thereafter the two irradiation-illumination-readout sequences adopted were the same as those used at OSU, except that a pre-heat stage was added between the irradiation and the illumination. The pre-heat consisted of heating the sample (at 2.0 K s^{-1}) to 325 K. In each case the TL data were plotted as the percentage TL lost due to the illumination, defined as

$$\% TL_{lost} = \frac{TL_0 - TL_\lambda}{TL_0} \times 100 \qquad (4.1)$$

where TL_0 is the TL obtained immediately after irradiation (and pre-heat) but without any illumination, and TL_λ is the TL following illumination for a given time at wavelength λ.

4.3   Results

4.3.1   TL Glow Curves

Figure 4.1 shows some typical TL glow curves from α-Al$_2$O$_3$:C (TLD-500) following

irradiation (33 mGy–300 Gy) at room temperature. The same sample was reused in these

measurements; following each TL reading, the sample was annealed at 1175 K for 15 min

before being re-irradiated. All curves are normalized to the same peak height. The variation

in the position and shape of the peak as a function of the absorbed dose suggests that the

apparently single peak is in fact made up of several overlapping peaks, in agreement with

earlier assertions[34,54]. Over the dose range from 10 mGy to 10 Gy the peak position is

steady at 453 K (for a heating rate of 2.05 K s^{-1}). However, for doses >10 Gy, the combined

peak shifts to lower temperatures. This is illustrated in Figure 4.2, and is in agreement with

previous data[45]. The observation of a shift over a certain dose range, coupled with the

symmetric shape of the peak, has led some authors to conclude that the kinetics of TL

production are non-first-order. For example, Kitis et al.[37] conclude that the TL signal is

a single peak, described by a kinetic order of ~1.45. Similarly, Kortov et al.[38] and Milman

et al.[39] assume a single peak, concluding that the kinetics are second-order. However, the

conclusions of these authors predict a monotonic shift in the peak position with dose – a

prediction which is not observed in our work. Using the parameters determined by Kortov

et al.[38] and Milman et al.[39], the predicted shift[71] in the peak position is illustrated in

Figure 4.3. The actual behavior of the peak position as a function of dose (Figure 4.2) does

not conform to this simple pattern. The present data, along with the data from other

studies[45,65] indicate that the shift is a complex function of the dose, the type of radiation,

the annealing conditions and the illumination history. In addition, the shift is sample

50
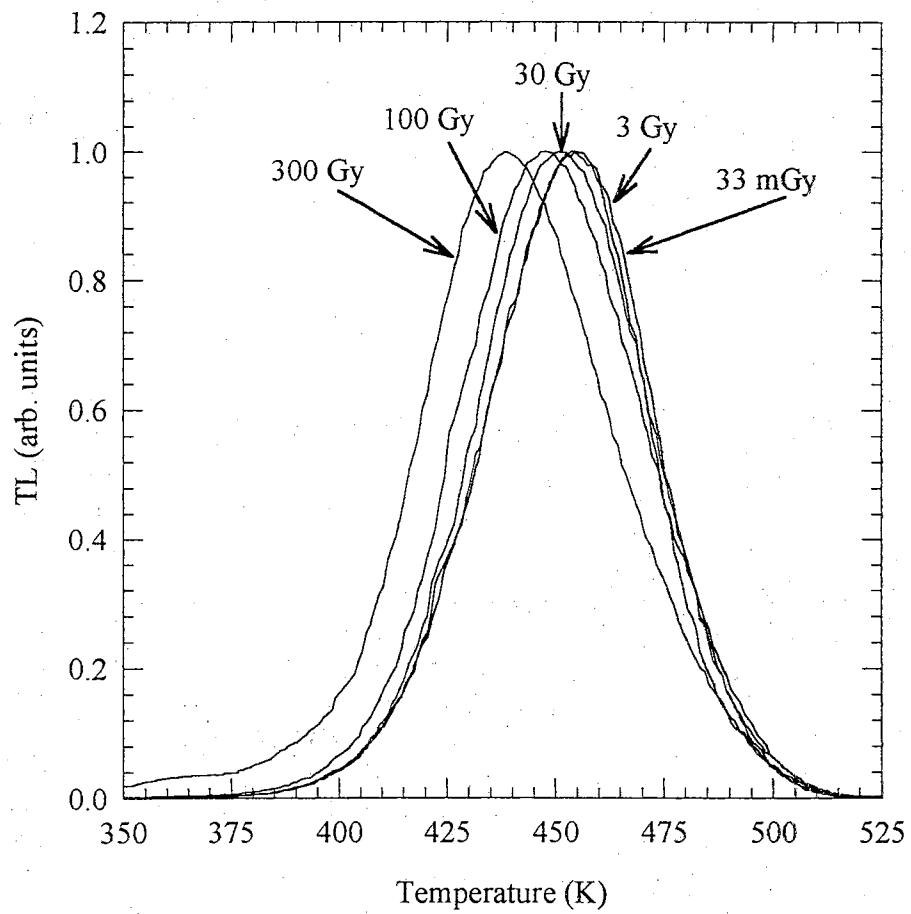
Figure 4.1 - Changes in TL Peak as a Function of Dose. The variation in the TL peak as a function of dose over the dose range 33 mGy–300 Gy. The peaks have been normalized to the same peak height.

51
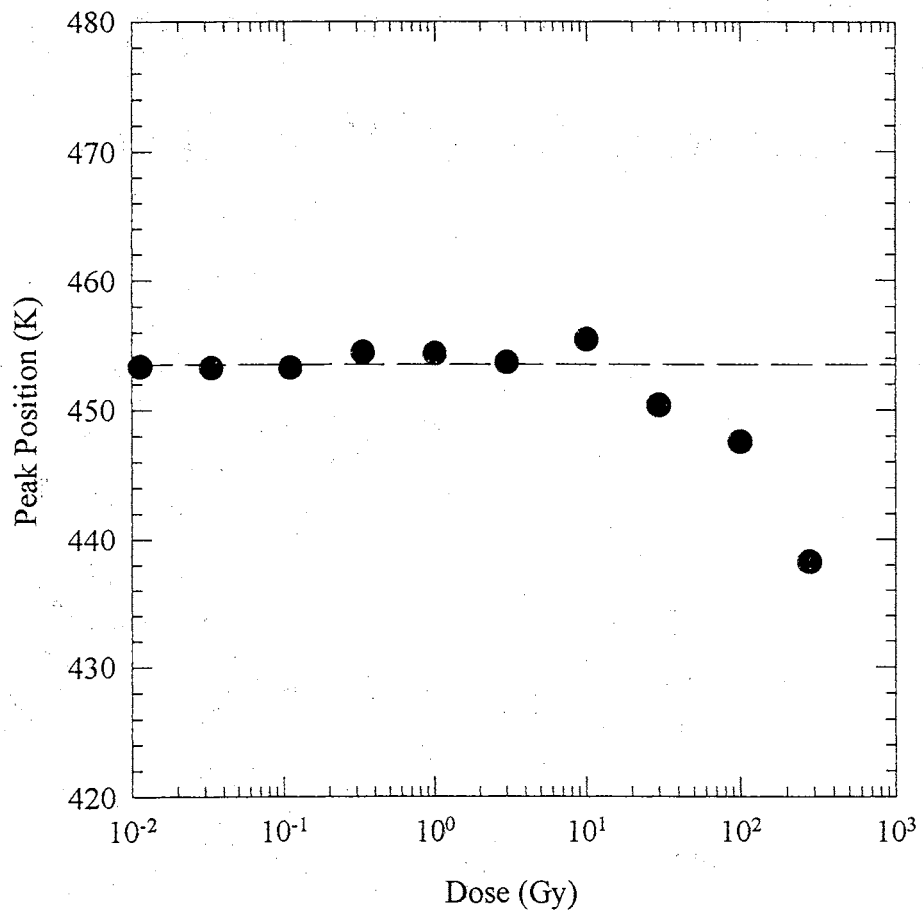
Figure 4.2 - Dose Dependence of TL Peak Position. The shift in the position of the main dosimetric peak as a function of dose. Filled circle - peak position of the glow curves shown in Figure 4.1.
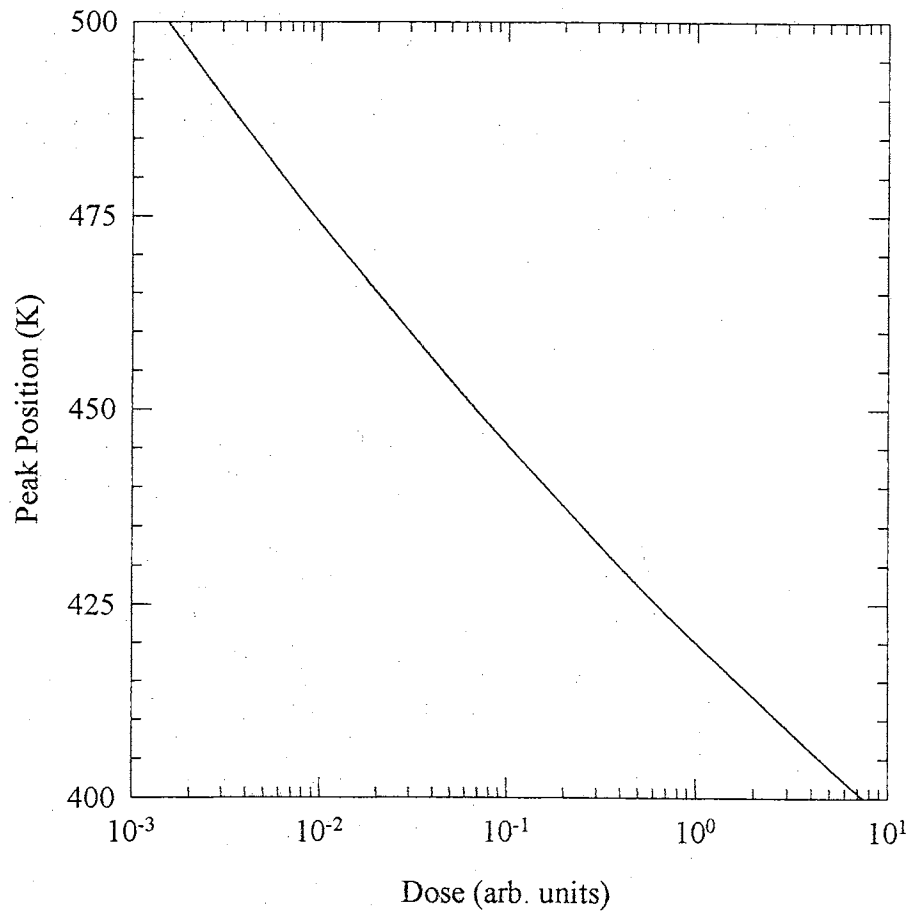
Figure 4.3 - Predicted Dose Dependence of TL Peak Position. The expected shift for a second-order process using the parameters obtained by Kortov et al.[38] and $\beta = 2.0\ K\ s^{-1}$. The comparison indicates that the kinetics do not follow simple second-order but suggests that the TL peak is, in fact, a composite of several overlapping components. [Note that 'dose' is given in arbitrary units since this is a calculation of the shift in the peak position as a function of the level of trap filling. The latter is related to 'dose' by unknown constants.]

dependent. The observed dependence on dose is more likely to be a function of the different growth rates of each of the overlapping components of the TL peak, as a function of dose, rather than non-first-order kinetics. Thus, the data suggest that several closely spaced energy levels (or even a distribution of levels) contribute to the TL signal. The contribution of a set of energy levels (or distribution) is important in understanding the wavelength dependence of the optical sensitivity of the TL signal.

The TL from α-Al$_2$O$_3$:C is known to suffer from thermal quenching[55]. As a result, the high temperature side of the TL glow curve may be distorted (i.e. reduced intensity) and, in principle, one should correct for this before analysis of the glow peak is performed. The correction curve for thermal quenching of luminescence is generally of the form of the Mott-Seitz equation[71]:

$$\eta(T) = \frac{1}{1 + C \exp\{-\Delta E / kT\}} \tag{4.2}$$

where $\eta(T)$ is the luminescence efficiency at temperature T, C is a constant, ΔE is the activation energy required for thermal quenching, and k is Boltzmann's constant. Corrections of this sort are not normally applied during routine dosimetry measurements, however. In the present work the TL intensity is defined as the peak height. Although small shifts in peak position are observed as a function of bleaching, the errors associated with ignoring the thermal quenching correction when determining the normalized TL intensity (cf. Equation 4.1) are minor and have little effect on the final conclusions. As a result, no attempt was made to account for thermal quenching of the TL signal in any of the measurements. Similarly, since for first-order kinetics, the peak height is proportional to the peak area, no major alterations to the conclusions would be found by monitoring the peak area.

Since the TL peak shifts to lower temperatures at higher doses (>~10 Gy), the TL peak is likely to be less affected by thermal quenching in this dose range, such that the TL peak will be slightly larger than otherwise expected at these dose levels. This may partially explain why more supralinearity is observed in the TL response of this material[32,98] than in the OSL response[61,66]. In fact, a more appropriate interpretation may be that the TL response is actually sublinear at lower doses.

4.3.2 Wavelength Dependence of Light-Induced Fading

Measurements of the dependence on wavelength were performed at Risø. The illuminations were performed at fixed energy, varying the illumination time to account for the variation in the power of the lamp at different wavelengths. The wavelength dependence of the bleaching efficiency under these conditions (expressed as the percentage TL lost) is summarized in Figure 4.5. Two sets of data for unannealed samples and one set for annealed samples are shown in this figure. Little difference is observed between the data sets, which suggests that samples exposed to low doses of irradiation do not require annealing prior to re-use. Figure 4.4 clearly shows longer wavelengths are less effective at removing the TL signal than shorter wavelengths.

4.4   Discussion

4.4.1   Wavelength Dependence

The data presented reveal that the TL signal from α-Al_2O_3:C is extremely sensitive to visible light and that significant loss of the TL signal can occur. The overall behavior is insensitive to whether or not the samples had been annealed immediately before irradiation and illumination for the relatively small doses used in this experiment. However, a more
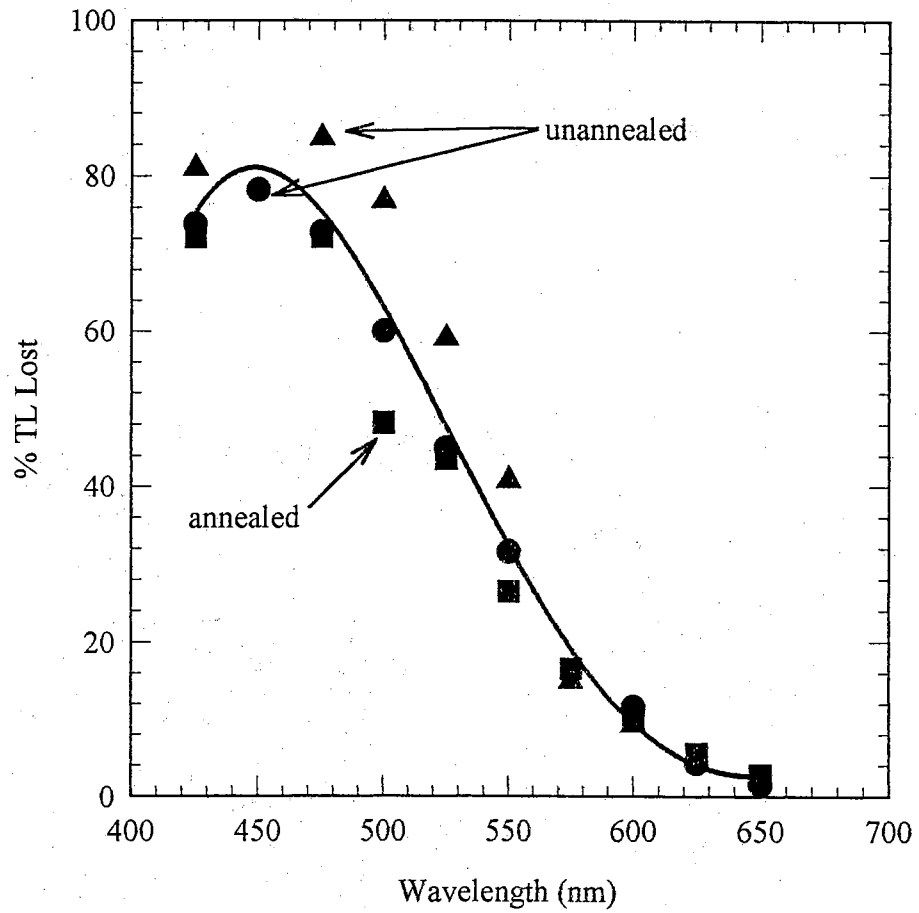
Figure 4.4 - Percentage TL Loss as a Function of Illumination Wavelength. Percentage TL lost as a function of the wavelength of the illuminating light, under conditions of constant illumination energy. Data are recorded using the Risø apparatus. The three data sets include two annealed samples and one unannealed sample.
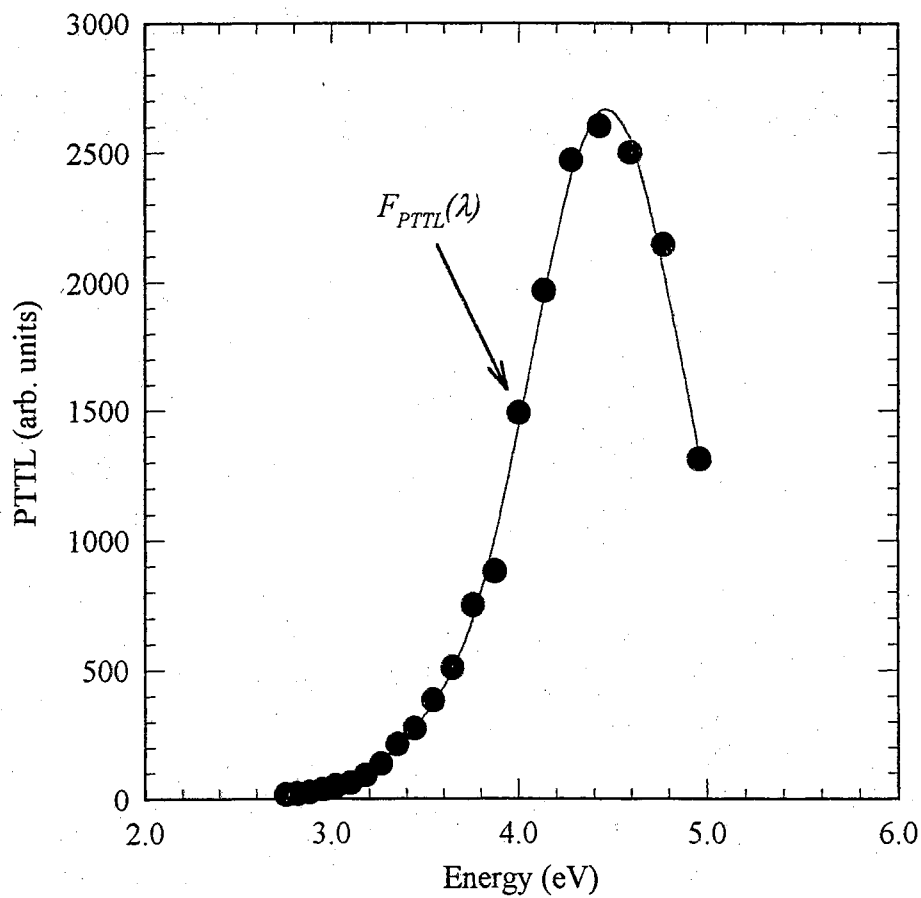
Figure 4.5 - PTTL Excitation Spectrum. PTTL excitation spectrum for the transfer of charge from the deep traps into the dosimetric trap. The data are redrawn from Figure 4(b) of Colyott[65] and the fitted line is $F_{PTTL}(\lambda)$.

pronounced dependence upon annealing is expected for samples which have received larger doses. The simplest interpretation of these data, therefore, is that the light is optically stimulating charge into the delocalized band from the traps responsible for the main dosimetry peak (Figure 4.4), thus giving rise to a weaker TL signal. The proposition that the light excites charge into the delocalized bands is supported by the photoconductivity data of Walker et al.[58], which show a maximum photocurrent in this same wavelength region. This proposition is further supported by recent PTTL data[65] (as discussed in Chapter 2), which clearly show that the main TL peak is the major source of phototransferred charge to low temperature traps (i.e. traps responsible for TL peaks at temperatures less than or equal to room temperature, RT), when an irradiated sample is illuminated at T ≤ RT.

The PTTL data also show the illumination of an irradiated sample transfers charge from deep states into the main dosimetric traps. Oster et al.[60] and Colyott et al.[65] determined the wavelength dependence of this process and the relevant data from the latter authors are shown in Figure 4.5, which shows wavelengths less than 400 nm are the most efficient for these processes. We also observe that some transfer occurs over a part of the wavelength range used in the present experiments. Thus, as the wavelength is reduced there is an increasing likelihood that the light, in addition to emptying charge from the dosimetric traps, is also transferring charge into these traps from the deep traps. The balance between these two effects, and their individual wavelength dependencies, determine the net trapped charge population at the dosimetric traps for a given irradiation dose, illumination power and illumination time. Thus, for fixed conditions of illumination (power, time, etc.) we can write that the wavelength dependence of the TL lost is determined by:

$$\% TL_{loss}(\lambda) = F_f(\lambda) - F_t(\lambda) \qquad (4.3)$$

where $F_f(\lambda)$ is a 'fading function' and $F_t(\lambda)$ is a 'transfer function'. The form of the fading function can be approximated by the photoionization cross-section $\sigma_0(\lambda)$ expected for ionization of charge from deep centers into the delocalized band. Assuming parabolic bands, this can be written[96] as (from Eq. 2.47, with $hv \gg \gamma E_0$)

$$F_f(\lambda) = K_1 \sigma_0(\lambda) \approx K_2 \sqrt{E_0} \frac{(hv - E_0)^{3/2}}{hv^3} \tag{4.4}$$

where K_1 and K_2 are constants, E_0 is the threshold energy for ionization (i.e. the optical trap depth) and hv is the energy of the incident photon. Similarly, $F_t(\lambda)$ is determined from the function $F_{PTTL}(\lambda)$ shown in Figure 4.5, i.e.

$$F_t(\lambda) = K_3 F_{PTTL}(\lambda) \tag{4.5}$$

where K_3 is a scaling constant.

Figure 4.6 shows a fit of experimental $\%TL_{lost}$ data to Equation 4.3, using Equation 4.4 and Equation 4.5, with K_2, K_3 and E_0 as fitting parameters. While the fit is crude, the main elements of the data can be observed – namely, a threshold energy near 2 eV and a maximum in the response near 2.75 eV (450 nm). This illustration assumes only one trap, whereas, as noted earlier, the TL signal under study appears to be made up of several overlapping components, implying several closely spaced traps, each with its own optical trap depth. (For example, the addition of an extra trap with a threshold energy of ~1.82 eV could easily account for the low energy tail in the data.) This crude model suggests the observed result can be reasonably explained by considering the wavelength dependence of both the optical emptying of the trap and the optical transfer of charge into the trap.

If PTTL must be considered in order to explain the wavelength dependence of the TL fading, then a sample which has not been annealed at high temperature between uses should
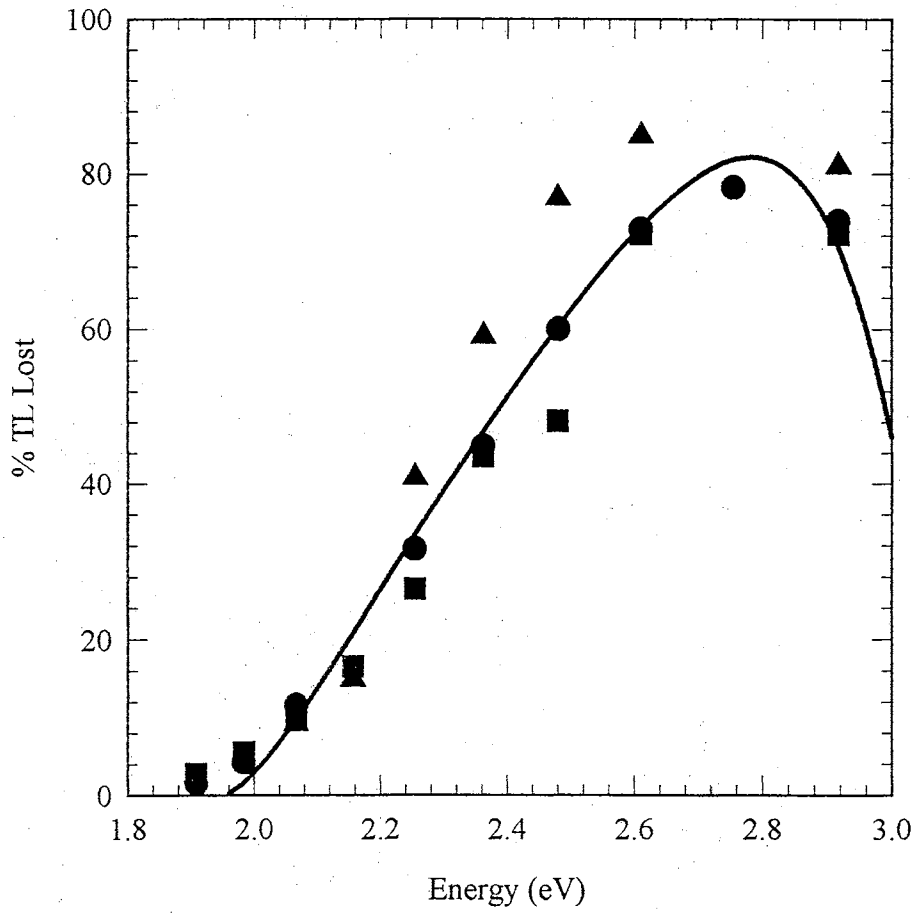
Figure 4.6 - Percentage TL Loss as a Function of Excitation Energy. The data of Figure 4.4 replotted as a function of energy and fitted to Equation 4.3.

display a greater PTTL effect than a sample which had been annealed. Akselrod and Gorelova[54] have demonstrated that the PTTL efficiency is dependent upon the annealing temperature and is much reduced after annealing above 1075 K. However, the doses used by these authors (3 kGy) are over four orders of magnitude higher than the doses used in the present study (100 mGy). While we find little difference in the behavior of the annealed and the unannealed samples at low doses, samples which had previously been exposed to large doses (such that a considerable population of charge will be present in the deep traps) may display a noticeable dependence on the annealing treatment. This assertion is supported by the data of Figure 4.7. The λ-dependence of the fading was examined for a sample which had experienced a pre-irradiation dose of only 500 mGy, as compared to the λ-dependence of the same sample after it had received larger pre-doses of 5.0 and 50 Gy. In each case, the OSU apparatus was used and a constant photon fluence was maintained for each wavelength. The sample had been annealed at 1175 K before the start of the experiment. For the photon flux and illumination times used in this experiment only about 20% of the TL is lost due to fading for the 500 mGy pre-dosed sample. After a 50 Gy pre-dose, however, the PTTL component is so strong that, at short wavelengths, a large *increase* (60% at 300 nm) in the TL signal is observed. The 5.0 Gy pre-dose case is intermediate between these two. This result justifies our use of Equation 4.3 in describing the wavelength dependence of the TL sensitivity.

4.4.2   Relevance to Dosimetry

A few years ago, the use of α-Al$_2$O$_3$:C in low dose dosimetry, without thermal annealing, was demonstrated by Moscovitch[34]. The present data indicate that for low dose dosimetry the lack of thermal annealing does not have a significant effect on the optical fading characteristics of the TL, over the wavelength range studied. Our observation that red light
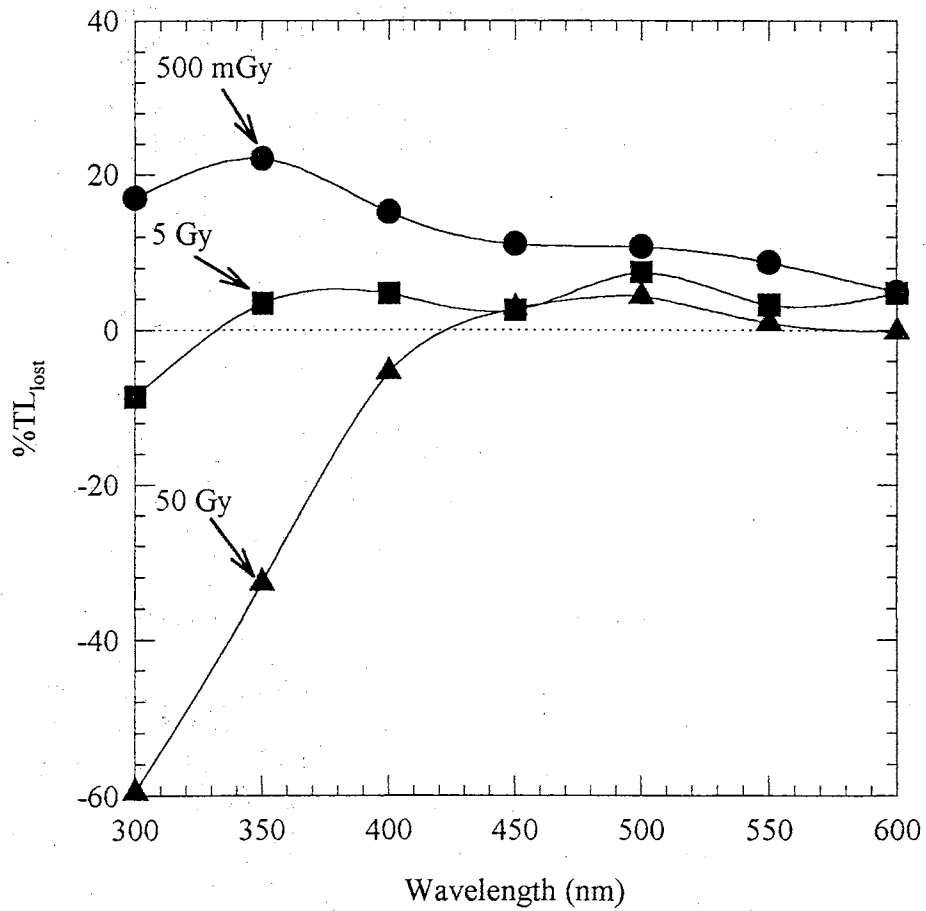
Figure 4.7 - Predose Dependence of Percentage TL Loss. Percentage TL lost vs wavelength for a sample which had received pre-doses of either 0.5, 5.0 or 50 Gy.

(580–600 nm) does not induce significant fading of the TL signal, for the light intensities and illumination times used in this study, is particularly important for dosimetry applications. Thus, while handling samples in red light may be acceptable, shielding them from shorter wavelength light is essential. Furthermore, packaging dosimeters in light-proof containers is imperative during dosimetry operation.

Chapter 5

5 An Application of PTTL to Ultraviolet-B Dosimetry

5.1 Introduction

In the past, most environmental ultraviolet (UV) dosimetry has been concentrated in the wavelength region from 320 nm to 400 nm (UVA)[102]. This was primarily due to the lack of any shorter wavelength UV transmission through the atmosphere. Specifically, the ozone layer, as well as atmospheric oxygen, absorbs all wavelengths below 280 nm and, until recently, most of the wavelengths below 320 nm[103]. Recent evidence of ozone layer depletion[104–106] however, has raised the issue of UV dosimetry for wavelengths shorter than 320 nm, particularly at southern latitudes where the ozone layer depletion appears to be most significant. A recent study in Antarctica indicates a 29% increase in ultraviolet-B (UVB) levels, concurrent with a 21% decrease in ozone layer column thickness[107]. Studies as far north as Toronto have indicated that summer ultraviolet-B (UVB), 280–320 nm, levels are increasing at a rate of 7% per year[108].

The current interest concerning UVB is due to the uncertainty of the biological impact this wavelength region may have on the molecules of plants and animals. Biological molecules such as proteins and nucleic acids may absorb UVB[109] and this may lead to problems regarding plant growth and flowering[110], pigment concentrations[111] and increased ratios of UV-absorbing compounds to chlorophyll[109,111–116]. In addition, several investigators have reported damaging effects to physiological processes (DNA damage[114],

photosynthesis, respiration and ion transport[117–119]) as a result of enhanced UVB irradiation.

Human and animal populations may expect a suppression of normal immune function[120]. In addition, increases in erythema (sunburn)[121], skin cancers (specifically, basal and squamous cell carcinomas)[122–124], eye disorders (particularly cortical cataracts)[125–127] and DNA damage[122,123,128] have been shown to increase as UVB levels increase.

Biological dosimeters (i.e. dosimeters based upon the response of a particular biological system), such as *Bacillus subtilis*[107], pre-Vitamin D and bacteriophage T7, have been used as UV dosimeters due to their small size, portability, lack of any power requirements, linear response to increasing radiation and sensitivity. Additionally, a UV dosimeter should preferably be unaffected by temperature and humidity[129].

UV dosimetry using TL has been suggested in the past[130–144] and offers the advantage of being able to place the dosimeters *in situ*, without requiring any special monitoring or logistical considerations (e.g. portable field power source for any electronics, which other UV dosimeters may require). The design requirements of the UVB dosimeter described in this chapter included the ability to measure an integrated UV exposure, in air or in water, ranging from a few minutes in early morning sunlight to several days of total exposure. TLDs appear to offer these characteristics and, based upon previous work[58,65], α-Al_2O_3:C appeared to be a suitable TLD material to accomplish the task. This material is a sensitive TL and PTTL detector. In particular, the PTTL properties of α-Al_2O_3:C provided the versatility required for this UVB dosimeter.

65

In general, PTTL involves the production of TL by the phototransfer of charge to empty traps from deeper, filled traps. Thus, by filling the deeper traps (as well as the dosimetry trap) of α-Al_2O_3:C with a pre-dose of irradiation and subsequently preheating the sample to remove any trapped charge from the dosimetry trap, charge can be transferred from the deep traps to the dosimetry trap when exposing the sample to light. When heated, a TL peak – the PTTL signal – is observed when the transferred charge is released from the dosimetry traps. The PTTL signal is proportional to the light exposure, as well as the initial pre-dose of irradiation. The light-induced effects of transferring charge from deep traps, while at the same time fading the induced TL signal, have been discussed in depth in Chapter 4. While α-Al_2O_3:C's sensitivity to light can be a disadvantage when dealing with TL fading issues[32,47,56–59], this 'problem' can be taken advantage of through the use of PTTL. The PTTL wavelength dependence of α-Al_2O_3:C has been shown[58,65] to peak in the region of interest. As a result, the current design of this UVB dosimeter is based upon the UV PTTL efficiency of α-Al_2O_3:C.

5.2   Dosimeter Design

Figure 5.1 is a schematic drawing of the dosimeter. The dosimeters were machined from black Delrin™. Each dosimeter consisted of a Teflon™ window/diffuser (thickness - 0.3 mm), a UVB interference filter, a second Teflon™ diffuser (thickness - 0.8 mm) and a thin-layer α-Al_2O_3:C detector. The 25 mm diameter UVB interference filters (CVI model F25-307.1-4, diameter - 25.4 mm, thickness - 3.5 mm) were centered at 307 nm with a FWHM of 25 nm. O-rings at the window interface and the cap/base interface make the dosimeters light tight, as well as watertight.
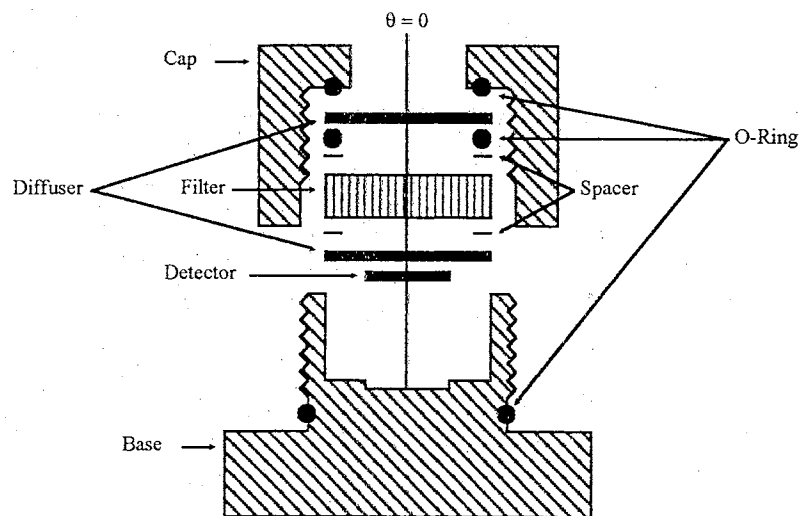
Figure 5.1 - Schematic Diagram of UVB Dosimeter. Dosimeter dimensions: cap diameter - 41.3 mm, base diameter - 50.8 mm, height (when sealed) - 32.1 mm, opening diameter - 19.1 mm.

Thin-layer α-Al$_2$O$_3$:C detectors were used, which have been described previously and used in beta-particle dosimetry[45]. They consisted of a thin layer of α-Al$_2$O$_3$:C powder (2–5 mg cm^{-2}, grain size < 40 μm) on a 1 cm diameter by 1 mm thick aluminum substrate. The α-Al$_2$O$_3$:C powder is pressed into the substrate and requires no binding material[45]. The thin-layer α-Al$_2$O$_3$:C detectors were provided by Stillwater Sciences, LLC.

5.3   Experimental

Dosimeter calibrations were conducted using natural sunlight and a Biospherical Instruments model GUV-511C ground-based ultraviolet radiometer. The 305 nm channel was monitored and data recorded every 30 seconds. Each 30 second record comprised an average of approximately 100 scans of the 305 nm channel. Measurements of UVB intensity with respect to the time-of-day (and, indirectly, the angle of the sun) were made using an Ultra-violet Products model UVX-31 radiometer. Intensity readings were made on the same sunny day, recorded every 30 seconds for 30 minutes and integrated.

In order to perform the PTTL measurements, the thin-layer detectors were first pre-irradiated to a dose, D (typically 1–30 Gy), in a ^{60}Co gamma source at room temperature. The detectors were then preheated at 600 K for 2 minutes to remove the charge trapped at the main dosimetry trap (~465 K). Subsequent UV illumination then produced the PTTL signal which, as will be shown, is proportional to the UV exposure.

Each detector calibration was performed using multiple laboratory UV illuminations and PTTL measurements. The UV calibration illuminations were conducted using a 150 W Xe arc lamp with silica condenser optics and a GCA/MacPherson model 218 monochromator. The monochromator was equipped with a 1200 lines·mm^{-1} grating, blazed at 300 nm with a

linear dispersion of 2.65 nm mm^{-1}, and set to 307.0 nm with a bandwidth of 2.3 nm. A fused silica fiber optic guide was used to focus light onto the sample. Illuminations were made at room temperature for 10 minutes with an intensity of 0.250 μW cm^{-2}. The power was measured using a Newport Research model 815 power meter with model 818-UV silicon photodetector.

All PTTL measurements were made with the computerized TL system at Oklahoma State University (OSU) in a nitrogen atmosphere at a partial vacuum of 600 torr. The temperature controller provided a linear heating rate of 2 K s^{-1}. Light was collected with a model 9635QB Thorn-EMI bi-alkali photomultiplier tube (PMT), which was used in current mode.

The dependence of the PTTL signal on the temperature of the sample during illumination was investigated over the temperature range 200–400 K. The sample was heated or cooled to the appropriate temperature with a heating rate of 1 K s^{-1} in a nitrogen atmosphere at a partial vacuum of 600 torr. Once the sample reached the appropriate temperature, the illumination was performed, while maintaining a constant temperature. The PTTL measurement was then performed, as described above.

Measurements of the angular dependence of the interference filter were performed, using a Varian Corporation model Cary 5 UV-VIS-NIR spectrophotometer.

While individual α-Al$_2$O$_3$:C single crystal detectors can be used repeatedly, the detectors are normally annealed at ~1200 K to remove charge carriers from all known traps, prior to each irradiation. Earlier measurements have indicated that the deep traps are thermally stable up to 900 K and 1200 K[55,65]. One disadvantage of using thin-layer detectors is the inability to anneal these deep traps. Since each detector consists of α-Al$_2$O$_3$:C powder on an aluminum substrate (melting point 933 K), the thin-layer detectors cannot be annealed above

this latter temperature (unlike their single crystal counterparts). As a result, a 'weak beam calibration' was used for each sample. In this way, each sample is irradiated with a pre-dose of, say, 30 Gy, preheated and illuminated with a 'weak beam' ($0.250 \mu W \ cm^{-2}$) of 307.0 nm light for 10 minutes. This produces a given (relatively small) PTTL signal. Further measurements are then each followed by a similar 'weak beam calibration' to detect any change in the concentration of charge trapped in the deeper, source traps. If the 'weak beam calibration' signal indicates a depletion of charge in the source traps, a small 'restoration-dose' is applied to the detector to bring the calibration signal back to within tolerance (i.e. 1 standard deviation).

5.4 Results and Discussion

5.4.1 Phototransferred Thermoluminescence

As previously noted, phototransferred thermoluminescence is the production of light via phototransfer from deeper filled traps to empty shallower traps. Figure 5.2 shows a typical PTTL glow curve (30 Gy pre-dose) for the thin-layer detectors used in this study, following illumination at 200 K. Deeper traps, thermally stable up to approximatley 550 K, 900 K and 1200 K[55,65], are used as the source traps in the PTTL process. Figure 5.3 shows the PTTL glow curve of peak 3 produced with 'weak beam calibrations', for illumination temperatures of 200 K and 400 K. The PTTL signal used in this study is the area under the curve of peak 3. Figure 5.4 shows multiple 'weak beam calibrations' (illuminated at room temperature) for three typical detectors. The reproducibility of the PTTL measurement per detector showed an average percent standard deviation of $\pm$ 2.7%, as shown in Table 5.1. The detectors used in this study had a relatively large distribution in sensitivity from detector
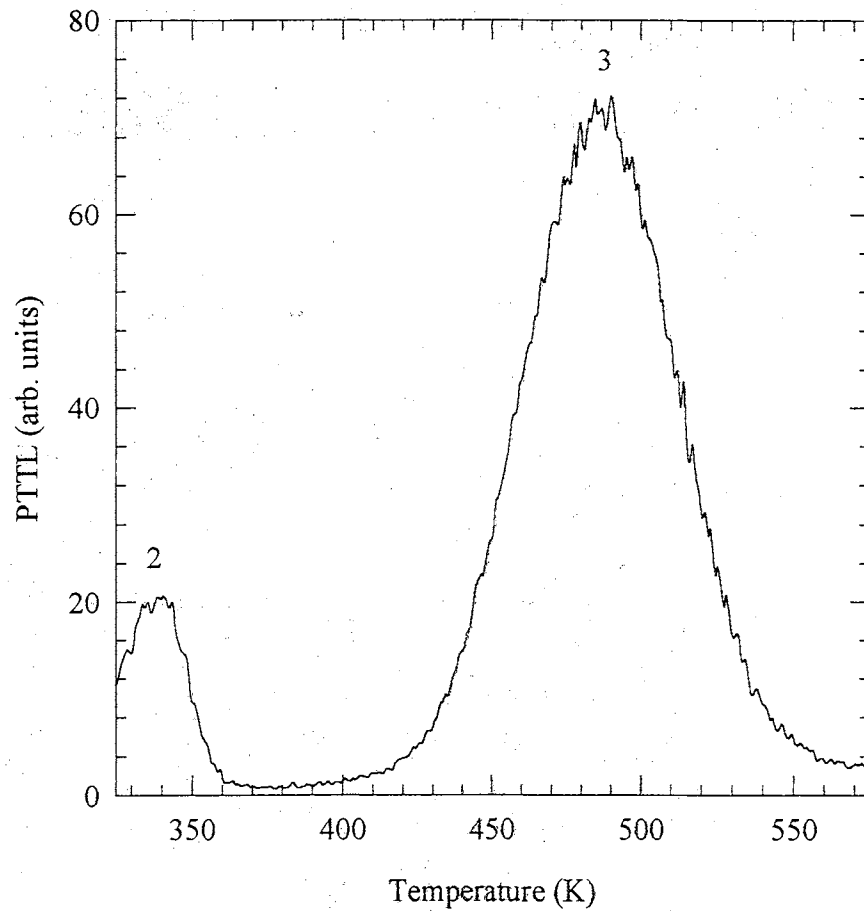
Figure 5.2 - PTTL Glow Curve for α-Al₂O₃:C Thin-Layer Detectors. Typical PTTL glow curve for α-Al₂O₃:C thin-layer detector following illumination at 200 K. The predose of 30 Gy ^{60}Co was delivered at room temperature. The sample was preheated to 600 K for 2 minutes and illuminated for 10 minutes at 307.0 nm with an intensity of 0.250 μW·cm^{-2} before being heated at 0.33 K·s^{-1}. Peak 3 is the 'main dosimetric' peak.

71
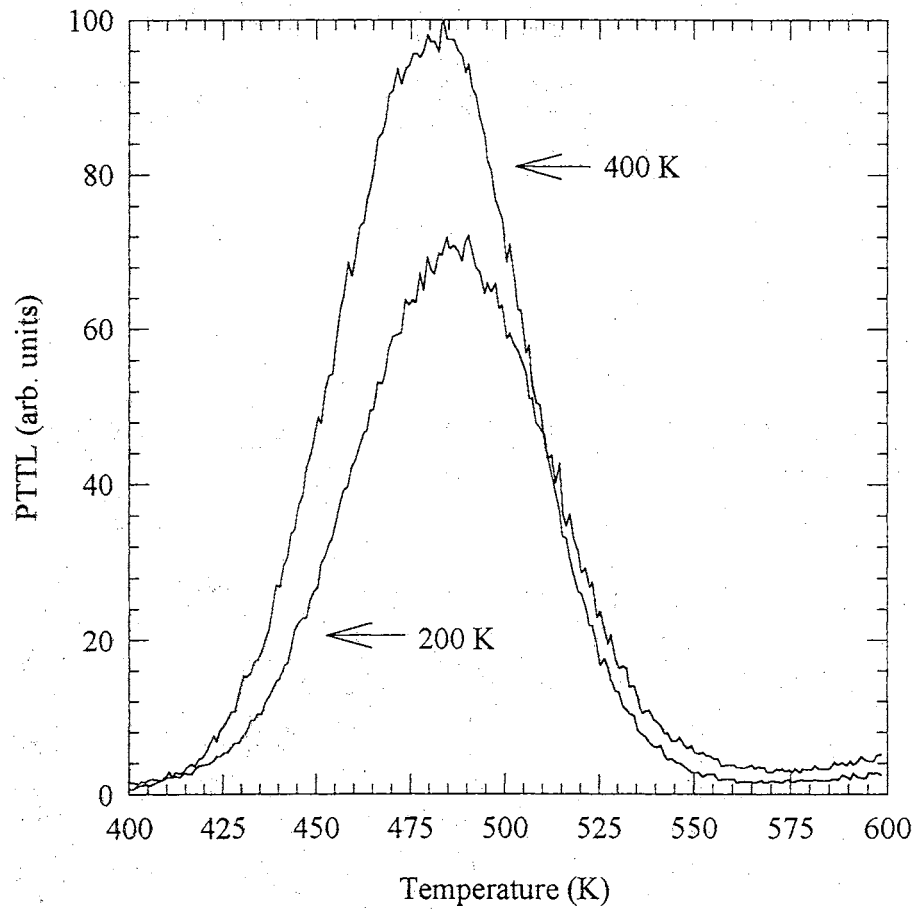
Figure 5.3 - Dependence of PTTL Glow Curve Shape on Temperature of Illumination. Comparison of PTTL glow curves following illumination at 200 K and 400 K. The predose of 30 Gy ^{60}Co was delivered at room temperature. The sample was preheated to 600 K for 2 minutes, then illuminated for 10 minutes at 307.0 nm with an intensity of 0.250 μW·cm^{-2} before being heated at 2.0 K·s^{-1}.
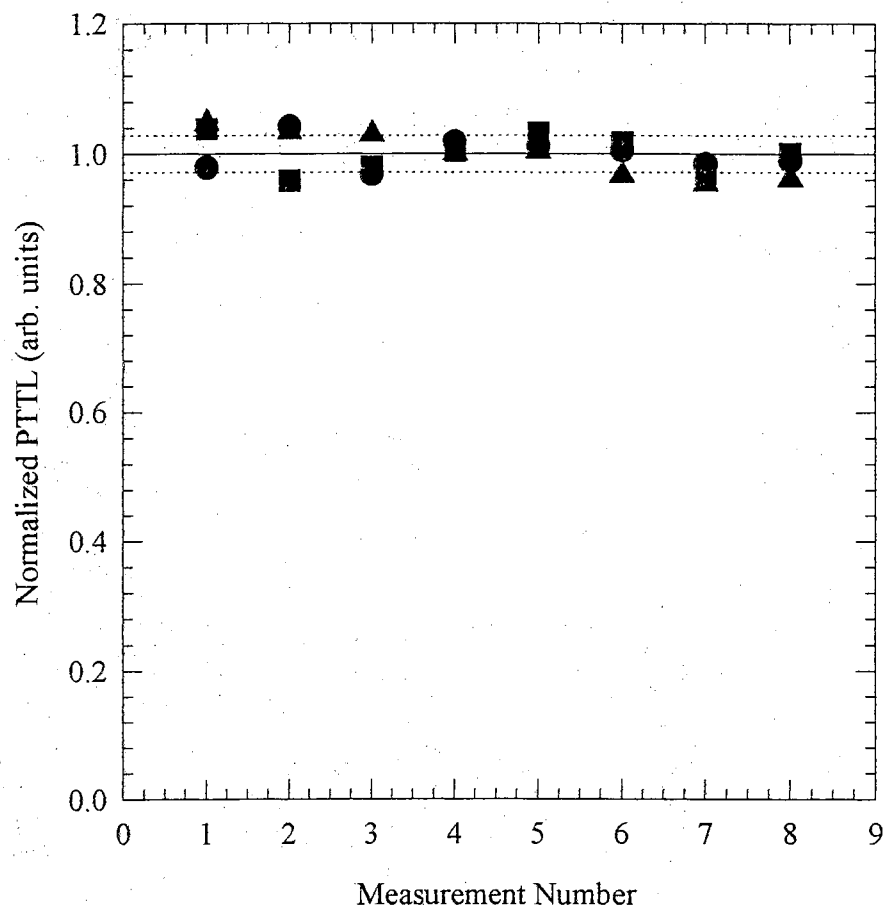
Figure 5.4 - Multiple Weak Beam Calibrations for Three Thin-Layer α-Al$_2$O$_3$:C Detectors. The predose of 30 Gy ^{60}Co was delivered at room temperature. The sample was preheated to 600 K for 2 minutes and illuminated for 10 minutes at 307.0 nm with an intensity of 0.250 μW·cm^{-2} before being heated at 2.0 K·s^{-1}. Each symbol represents a different thin-layer α-Al$_2$O$_3$:C detector. Solid line - mean PTTL signal, dotted line - ± 1 standard deviation.

Table 5.1 - 'Weak Beam Calibration' for Selected α-Al$_2$O$_3$:C Thin-Layer Detectors

Detector	Average PTTL	1 s.d.	%s.d.	Normalization
1	9018.3	30.6	0.3	1.13964
2	10855.6	254.1	2.3	1.37181
5	5732.0	137.0	2.4	0.72435
6	5170.0	150.0	2.9	0.65333
9	9149.9	209.0	2.3	1.15626
10	7130.7	106.7	1.5	0.90111
13	8166.2	246.5	3.0	1.03195
14	6764.6	169.9	2.5	0.85483
17	8490.5	717.2	8.4	1.07294
18	8419.3	399.0	4.7	1.06394
21	7609.1	52.8	0.7	0.96155
22	8514.9	183.1	2.1	1.07602
25	9137.4	445.9	4.9	1.15468
26	8896.2	301.5	3.4	1.12421
29	9473.7	34.1	0.4	1.19718
30	8684.6	192.7	2.2	1.09746

to detector (± 17%, with respect to the mean), which may be due to differences in the mass of powder deposited on each detector. The calibration of each detector (i.e. thin-layer of α-Al_2O_3:C powder on an aluminum substrate) was performed separately from that of each dosimeter (i.e. detector, with optics, inside of Delrin™ holders (see Figure 5.1)), as shown in Table 5.2. As a result of these measurements, a matrix of detector and dosimeter responses exists which allows calibration of any detector/dosimeter combination.

5.4.2 Dosimeter Response

Our UVB dosimeters were calibrated against the 305 nm channel of the GUV-511C radiometer. The exposures were made in natural sunlight at periodic intervals during the same day. Figure 5.5 shows the relationship between the response of the GUV-511C radiometer and the PTTL signal from our UVB dosimeters, using the calibration data for each detector/dosimeter combination, as described above. The data show a nearly linear relationship (slope = 0.95) over at least 3 decades of UVB exposure. As a result, we have dosimeters with a near-linear response from several minutes of early morning natural sunlight exposure to 4 days of total exposure. Based upon these and other measurements, we project we will be able to extend the high exposure limit of the dosimeters to approximately 60 days, while maintaining this linearity, with the current configuration of pre-dose, diffusers, etc.

5.4.3 Angular Response

The angular response of the dosimeter is an important design and performance consideration. Figures 5.5 and 5.6 show the response of the interference filter with respect to the incident angle of illumination. As expected, the central wavelength of the interference

Table 5.2 - UVB Dosimeter Calibrations

Dosimeter	PTTL	Detector	Normalized PTTL	Dosimeter Normalization
1	9382.8	23	8362.7	1.00000
2	7946.4	24	7825.5	0.93576
3	8728.6	25	7559.3	0.90393
4	9396.6	26	8358.4	0.99949
5	5148.1	27	6276.6	0.75055
6	5438.2	28	5772.8	0.69031
7	9233.9	29	7713.0	0.92231
8	7321.9	30	6671.7	0.79779
9	7035.7	31	5747.8	0.68731
10	5758.3	32	5099.4	0.60978
11	7163.0	6	10963.8	1.31104
12	12110.8	10	13440.0	1.60713
13	14513.1	13	14063.7	1.68172
14	10997.4	16	11975.6	1.43202
15	15383.3	17	14337.5	1.71446
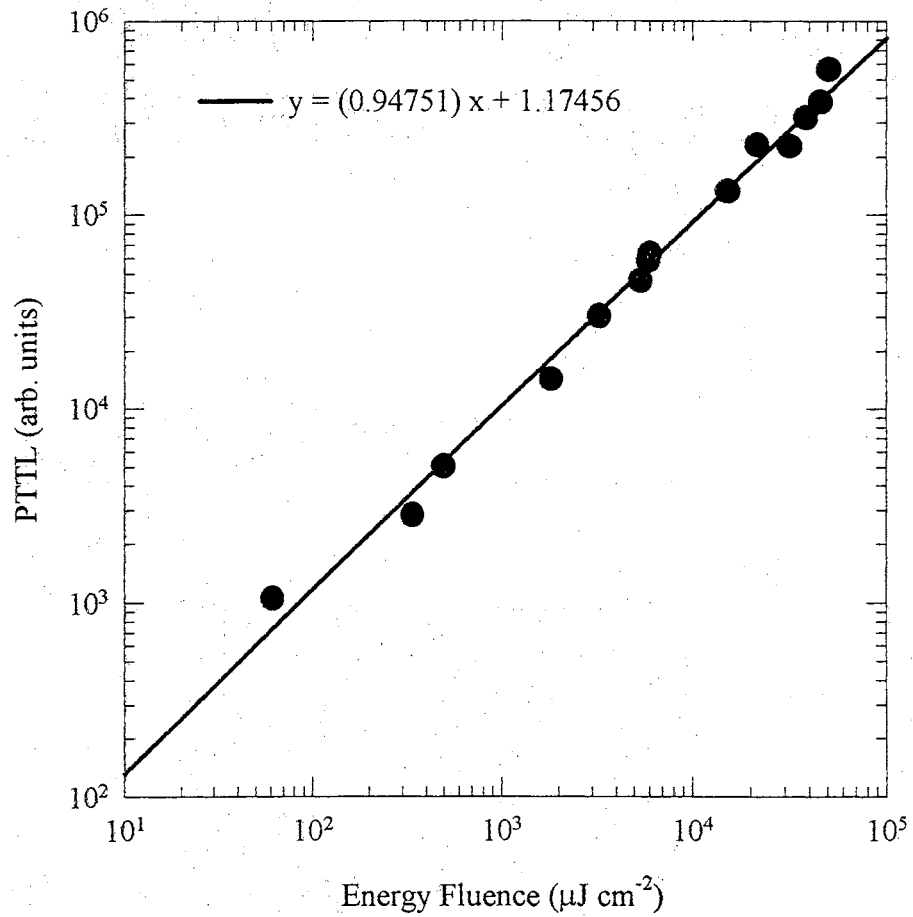
Figure 5.5 - UVB Dosimeter Response to Natural Sunlight. The predose of 30 Gy ^{60}Co was delivered at room temperature. The sample was preheated to 600 K for 2 minutes. The heating rate was 2.0 K·s^{-1}.
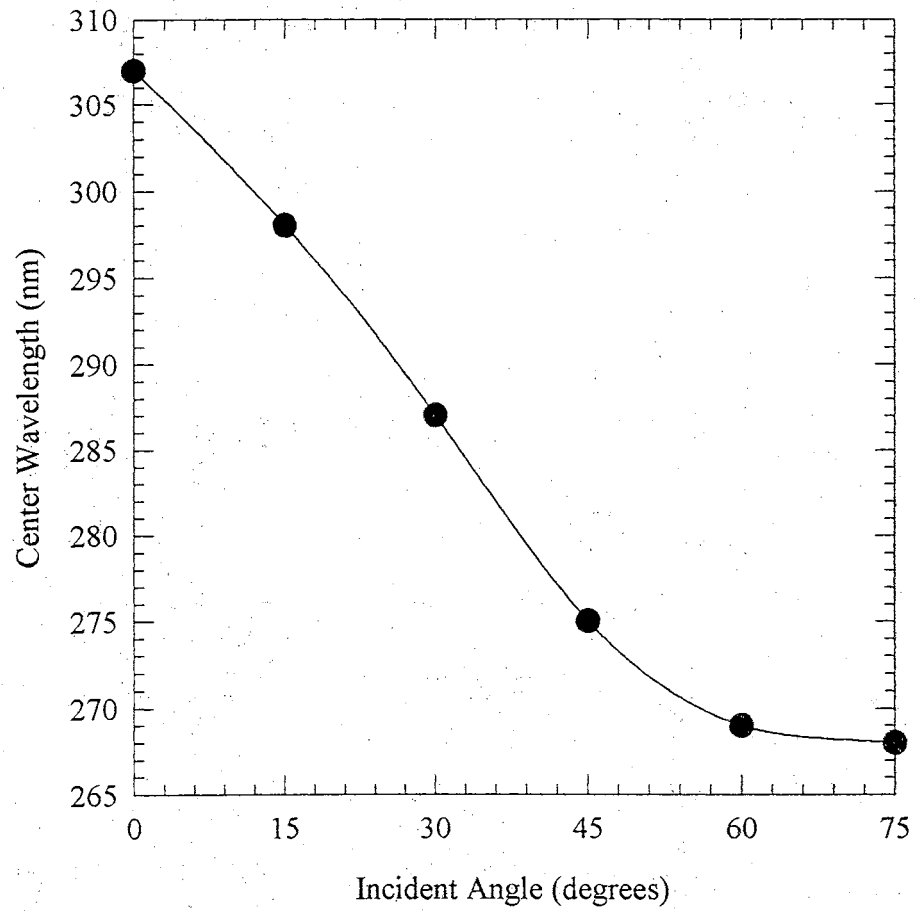
Figure 5.6 - UVB Interference Filter Central Wavelength Shift as a Function of the Incident Angle of Illumination.
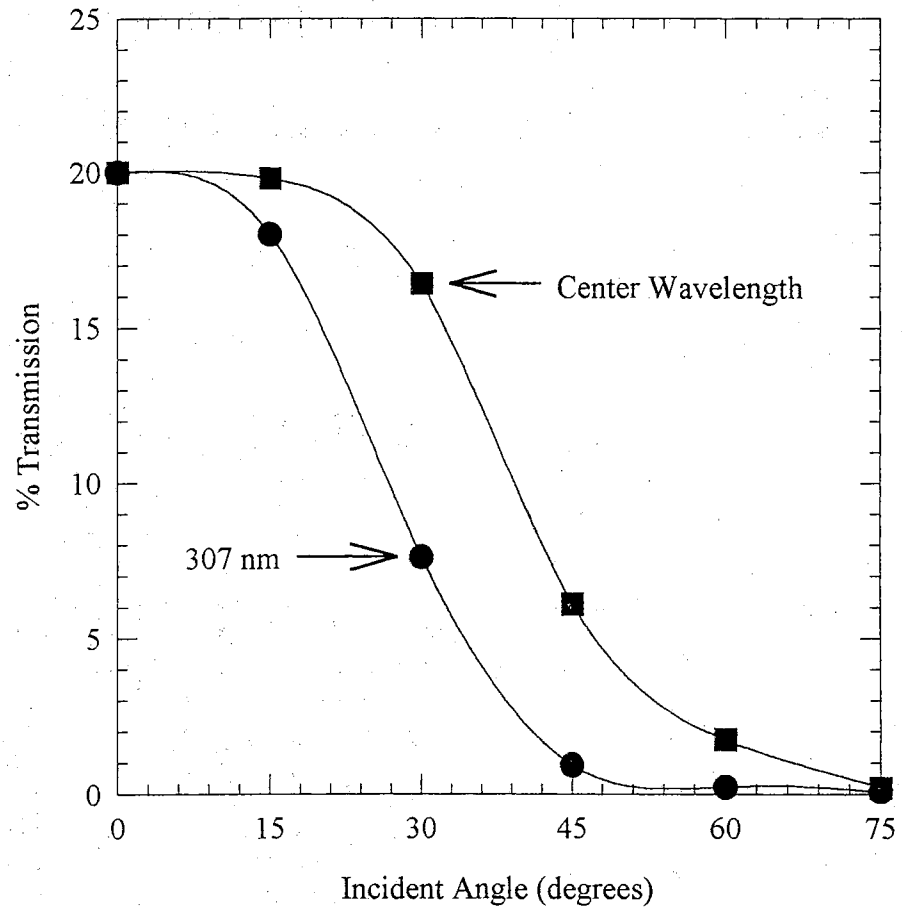
Figure 5.7 - UVB Interference Filter Response versus Incident Angle Illumination. Filled circle - 307 nm, filled square - central wavelength.

filter (Figure 5.6) shifts to lower wavelengths as the incident angle of illumination increases, with respect to the normal of the dosimeter. At the same time, the transmission of the interference filter (Figure 5.7) at both the central wavelength and at 307 nm (for which the filter was originally engineered) decreases as the incident angle increases. Figure 5.8 shows the overall dosimeter response with respect to the incident angle. For comparison, an 'ideal' cosine response curve is shown which represents the maximum normal component of light possible at a given angle of incidence. Comparing Figure 5.7 with Figure 5.8 shows how the dosimeter angular response is broader than that of the interference filter.

One reason for this is the effect of the Teflon™ diffusers. By scattering the incident light before passing through the interference filter, the 'bandwidth' of the incident angle is increased, allowing a distribution of incident angles θ to pass through the interference filter. The resulting response of the dosimeter becomes a summation of curves similar to those of Figure 5.7, each displaced by some $\Delta\theta$. The angular dependence of the dosimeter is thereby flattened with respect to that of the interference filter. In addition, the PTTL efficiency changes as the wavelength decrease[65]. Since the maximum PTTL efficiency occurs near 280 nm, as the central wavelength of the dosimeter shifts from 307 nm (at 0° with 20% transmission) to 268 nm (at 75° with <1% transmission) the efficiency of charge carrier phototransfer increases. This effect also contributes to the flattening of the dosimeter's angular response. The current design restricts the amount of high incident angle light entering the dosimeter as a result of the 6 mm ridge around the Teflon™ window. Beveling the cap near the window to ~30° would allow more light to enter at higher incident angles. This design change should flatten the angular response even more, by simply increasing the amount of light entering the dosimeter at higher incident angles.
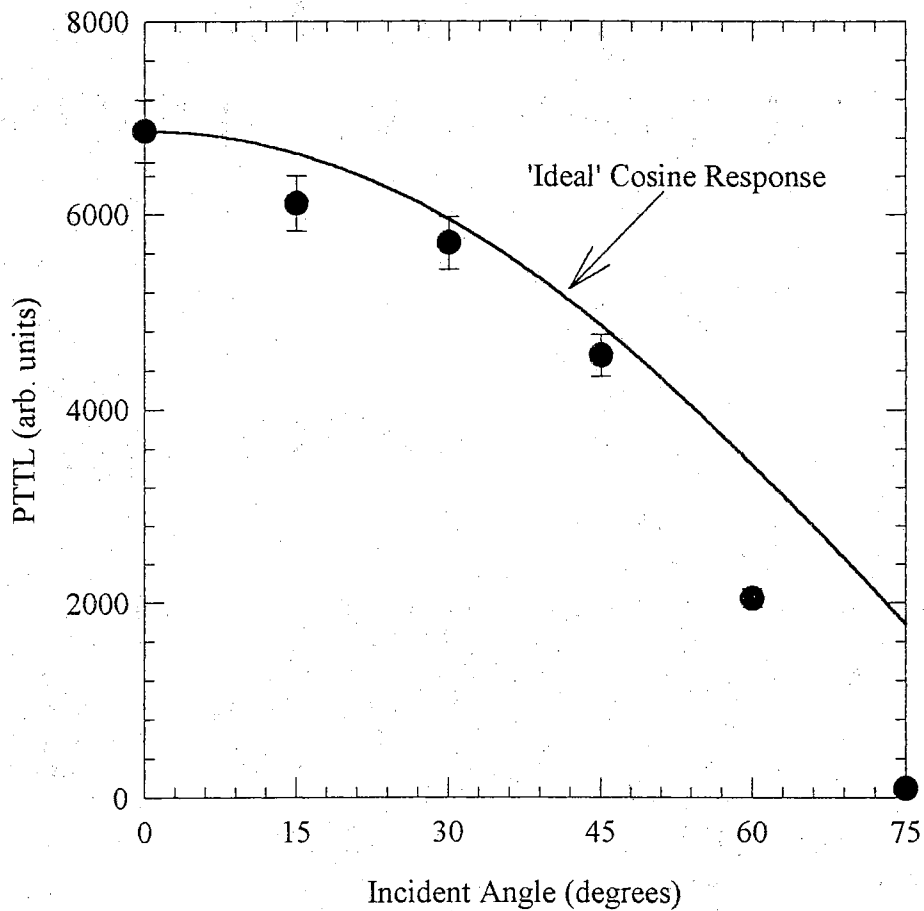
80

Figure 5.8 - UVB Dosimeter Response versus Incident Angle of Illumination. The predose of 30 Gy ^{60}Co was delivered at room temperature. The sample was preheated to 600 K for 2 minutes and illuminated for 10 minutes at 307.0 nm with an intensity of 16.0 $\mu W \cdot cm^{-2}$ before being heated at 2.0 $K \cdot s^{-1}$. Solid line - 'ideal' cosine response for incident light.

81

The response of the GUV-511C with respect to the time-of-day of the measurement is displayed in Figure 5.9, along with the response of the UVB dosimeters. In each case, the curves have been fitted to an equation which takes into account the approximate angle of the sun and the thickness of the atmosphere with respect to the angle of the sun.

Consider light of initial intensity, I_0, incident at an angle θ with respect to the normal. Defining $\theta = 0$ as the direction of normal incidence and assuming the atmosphere is a thick slab (thickness, d) above the region of interest, the actual pathlength for any incident light would be $d/\cos\theta$. This light is absorbed by the atmosphere (absorption coefficient, μ) with a resulting intensity of $I_1 = I_0 \exp\{-\mu d/\cos\theta\}$. The final form of the fitting equation is $I_2 = I_0 \cos\theta \exp\{-\mu d/\cos\theta\}$.

5.4.4 Temperature Response

Figure 5.10 represents the efficiency of phototransfer into the main dosimetry trap as a function of the sample temperature during illumination. While the PTTL efficiency is essentially flat in the region surrounding room temperature, the efficiency decreases by about 10% when illumination occurs at or below the temperature of the shallowest trap responsible for the TL at ~265 K (peak 1 of Figure 5.2(a)). The beginning of another increase of approximately 10% is observed once the illumination temperature of the sample is above that of the two shallow traps (peaks 1 and 2 at ~265 K and ~310 K, respectively (see Figure 5.2(a))).

The PTTL peak maximum shifts as a function of the temperature of the sample during illumination. The PTTL peak maximum appears at approximately 488 K, when illuminated at 200 K, and shifts to approximately 481 K, when illuminated above 240 K. Changes in the
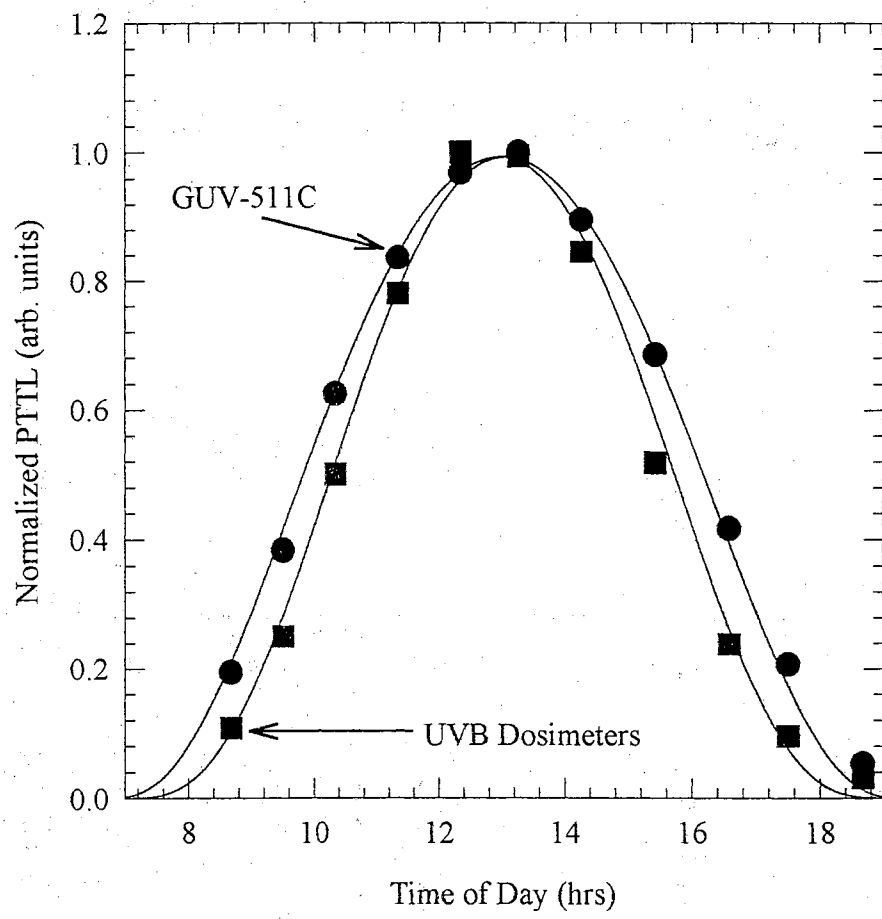
Figure 5.9 - GUV-511C Response and UVB Dosimeter Response as a Function of the Time-of-Day of Illumination. The predose of 30 Gy ^{60}Co was delivered at room temperature. The sample was preheated to 600 K for 2 minutes. The heating rate was 2.0 K·s^{-1}.
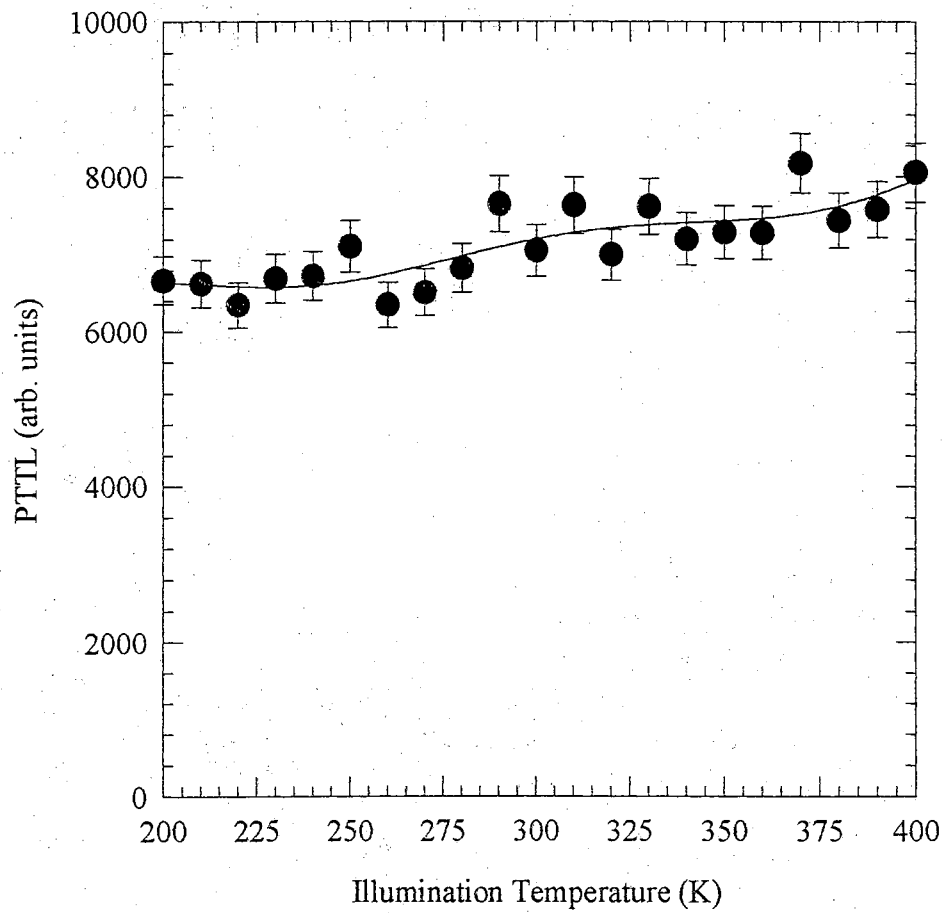
Figure 5.10 - Efficiency of PTTL versus Sample Temperature during Illumination. The predose of 30 Gy ^{60}Co was delivered at room temperature. The sample was preheated to 600 K for 2 minutes and illuminated for 10 minutes at 307.0 nm with an intensity of 0.250 μW·cm^{-2} before being heated at 2.0 K·s^{-1}.

PTTL glow peak shape were shown in Figure 5.2(b). At low illumination temperatures, the low temperature side of the PTTL peak is significantly smaller than that produced at higher illumination temperatures. Thus, as a result of the decrease in the temperature of the illumination, the PTTL signal is smaller and T_{max} is shifted toward higher temperature. These data support the view that the glow peak is caused by a distribution of trapping states[55,65].

5.5   Summary

An integrating UVB dosimeter with a response centered at 307 nm has been developed. This dosimeter takes advantage of the UV-induced phototransferred thermoluminescence efficiency of α-Al_2O_3:C in the wavelength region of 307 nm. The dosimeter can be used in air or in water and has no significant temperature dependence in the region of biological interest (273–323 K). The response of the dosimeter is consistent with the response which would be expected for light incident through an absorbing medium (the atmosphere). The UVB PTTL efficiency and addition of Teflon™ diffusers help to flatten the inherent angular dependence of the interference filter used in the dosimeter design. The observed changes in the glow curve shape due to the illumination temperature support previous work of the authors which suggest a distribution of electron traps may be responsible for the behavior of the 'main dosimetric peak', in α-Al_2O_3:C. The dosimeter has been field tested, in air and in water, and used in biological experiments at sites in Argentina, Belize, Chile, Mexico, and Oklahoma.

Chapter 6

6 Enhanced Numerical Analysis of TL and PTTL

6.1   Introduction

Traditional TL glow curve analysis produces the activation energies (E_t) and attempt-to-escape frequency factors (s) associated with particular glow peaks, subject to the initial assumptions made and parameters chosen for the analysis. However, this analysis does not discriminate between which type of incident radiation (γ, β, n, p, α) deposited energy into the TLD. As a result, unless the TL glow curve exhibits grossly distinct behavior when irradiated with γ-,β-,n-,p- or α-particles (e.g. peaks appear or disappear, depending upon the type of incident radiation), the TLD's response must be qualified with statements such as 'gamma dose equivalent'. In other words, although the measured dose response is similar to that obtained when calibrated against, say, ^{60}Co (E_γ = 1.250 MeV), the actual source of irradiation cannot be determined. This information is particularly important when considering the different biological effects on tissue due to various forms of radiation and the fact that TLDs do not respond in a constant manner when exposed to various forms of radiation.

This problem is most pronounced when considering the dose response in mixed radiation fields. For example, most neutron sources also produce a high gamma background. This results from the fact that most radioactive neutron sources depend upon the Be(α,n) reaction. An alloy is made of Be and a radioactive α-particle source, which results in the neutron emission. The α-emitter is usually ^{210}Po, ^{239}Pu, ^{241}Am, ^{226}Ra or one of their isotopes. The

mixed field results from the gamma photons emitted during the α-particle decay. Thus, a TLD with a markedly better response to gammas relative to neutrons will produce a significant TL signal that may erroneously be attributed to neutrons when, in fact, the response is due almost entirely to the gamma background. This is the case with α-Al_2O_3:C, where the neutron response is only ~4% of the gamma response.

Some TLDs have been engineered to respond differently to gammas and neutrons. LiF has proven to be the most sensitive TLD for thermal neutrons. This is due to the very high thermal neutron capture cross section of ^6Li (945 barns). Natural Li contains only ~7.4% ^6Li. By enriching the concentration of ^6Li to ~95.6%, the TLD's neutron sensitivity can be increased by a factor of 10. Similarly, by reducing the ^6Li concentration to only ~0.007%, the sensitivity can be reduced by a factor of 100. This is due to the relatively low thermal neutron capture cross section of ^7Li (0.033 barns). Thus, by using two TLDs, one with a relatively high ^6Li concentration and the other with a relatively low ^6Li concentration, a simple subtraction of the two signals will yield the actual neutron dose, i.e. while the ^6Li-based TLD will be sensitive to both neutrons and gammas, the ^7Li-based TLD will be sensitive only to gamma photons. The difference in the signals represents the neutron dose. The problem with this approach lies in the calibration of multiple TLD elements required to measure each type of radiation. The optimum approach is to allow the discrimination of various types of radiation, using a single TLD element.

Unfortunately, the absence of any grossly distinct TL effects within a single TLD means that information regarding the form of incident radiation is qualitative at best. Ideally, a truly useful analysis would produce quantitative information as well (e.g. the relative dose of each particle type in a mixed field environment.)

6.2 Linear Energy Transfer Dependence of α-Al$_2$O$_3$:C TL Glow Curves

Different forms of radiation are classified by the amount of energy deposited within a given local volume while traveling through the medium of interest. This linear energy transfer (LET) is intended to focus on the energy deposited in the medium of interest, rather than the energy lost by the incident particle, and to emphasize the local nature of the energy transfer. The LET of a particle of incident energy E, $L(E)$, is defined as

$$L(E) = \frac{dE_{local}}{dx} \qquad (6.1)$$

where dE_{local} is the average energy locally imparted to the medium by a particle of specific energy, while traversing a distance dx. The general trend for LET ordering of incident radiation particles is γ, β, n, p, α, where γ photons are considered to have a low LET, while α-particles have a much higher LET. Of course, these particles have broad energy ranges and penetration depths. As a result, different particle types may have the same LET (e.g. a high energy gamma photon may have a LET similar to that of a low energy neutron).

The main dosimetric peak of α-Al$_2$O$_3$:C shows a slight LET dependence. As shown in Figure 6.1, the peak width increases slightly with LET, where the peak height of each curve has been normalized to unity. (Specifically, the high temperature side of the TL signal shifts to significantly higher temperature, while the low temperature side appears at approximately the same temperature.) However, the main dosimetric peak width of α-Al$_2$O$_3$:C can vary widely from sample to sample and as a function of dose, even for the same radiation type. (In fact, although the temperature of maximum TL signal remains approximately the same, both sides of the TL signal may shift to different temperatures – unlike the LET dependent shift of only the high temperature side.) As a result, an increase in peak width does not
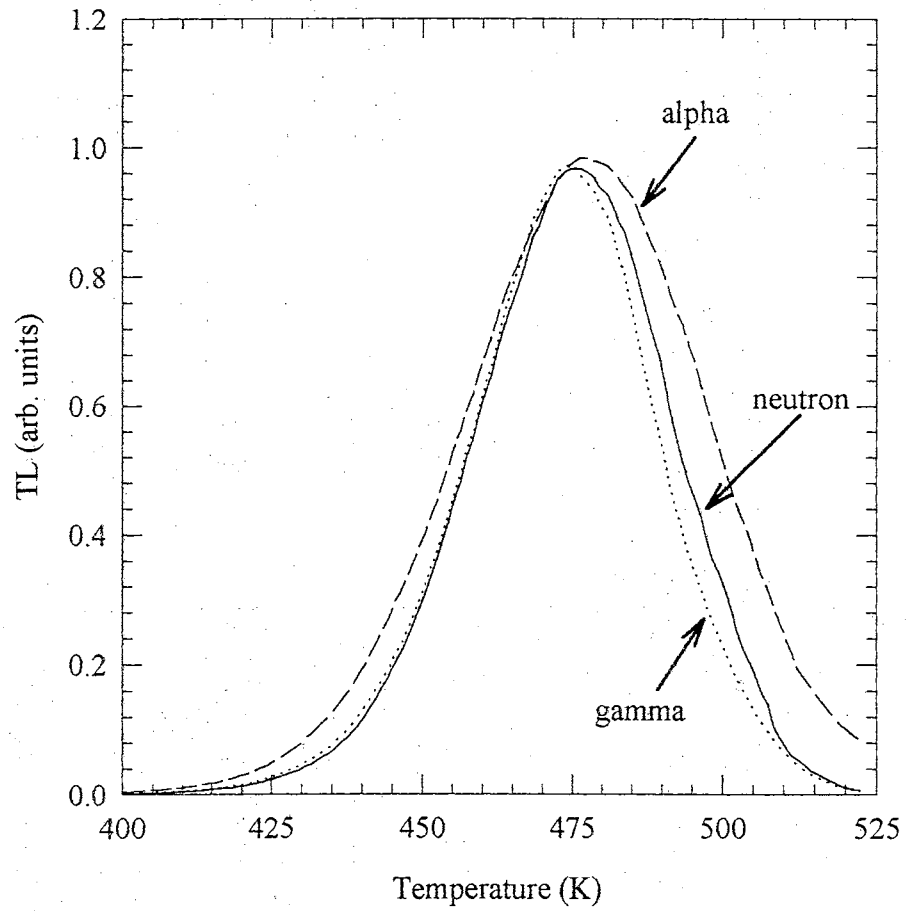
88

Figure 6.1 - LET Dependence of TL Glow Curves. The normalized glow curves of beta-induced (^{90}Sr/^{90}Y, 64 mGy), neutron-induced (1 MeV, 1 mGy) and alpha-induced (^{244}Cm, 1.2 Gy) TL are shown.

necessarily indicate irradiation with higher LET particles, unless the particular sample in question has been calibrated as a function of LET. In addition, the increase in the peak width is more of a qualitative, rather than quantitative, feature and the discrimination of mixed fields, in particular, requires a more quantitative approach. The shift of the TL peak and the variation in width as a function of sample, radiation type and radiation dose appear to be a microdosimetric effect related to the distribution of trapping states responsible for the main TL peak – as previously inferred from Chapters 3–5.

6.3 Distribution of Activation Energies

In general, TL and PTTL glow peaks have been considered single-valued functions, attributable to first-, second- or mixed-order kinetics. However, the trap depths associated with specific defects may be distributed over a range of values. If the lattice surrounding the defect responsible for the TL signal contains variations in the nearest neighbor bond lengths and bond angles, the trap depths may be distributed, rather than unique[77].

When assuming a distribution of activation energies (trap depths), the Randall-Wilkins equation for first-order kinetics (Eq. 2.18) becomes

$$I_{TL}(T) = \int_{E_A}^{E_B} n(E')s \exp\left\{-\frac{E'}{kT}\right\} \exp\left[-\frac{s}{\beta}\int_{T_0}^{T} \exp\left\{-\frac{E'}{k\Theta}\right\} d\Theta\right] dE' \qquad (6.2)$$

where $n(E')$ represents the activation energy dependent trapped charge distribution function, with high and low energy limits of E_A and E_B, respectively[71]. For a uniform distribution,

$$n(E) = n_t \frac{(E - E_A)}{(E_B - E_A)} \qquad (6.3)$$

where n_t is the concentration of constant trapped charge between E_A and E_B. For an exponential distribution, from $E_A = 0$ to E_B,

$$n(E) = n_e \exp\left\{\frac{(E - E_B)}{kT_c}\right\} \qquad (6.4)$$

where n_e is a constant and T_c is a characteristic temperature for the distribution. For a Gaussian distribution,

$$n(E) = n_m \exp\left\{-\left(\frac{E - E_0}{\sigma_E}\right)^2\right\} \qquad (6.5)$$

where n_m is the maximum concentration at the center of the distribution, E_0, and σ_E is the standard deviation of the energy distribution.

In the case of α-Al$_2$O$_3$:C, the results of several experiments (described previously in Chapters 3–5) suggest a distribution of traps are responsible for the TL (and PTTL) signal of the main dosimetric peak. However, the data further suggest that the distribution is comprised of only first-order peaks (see Chapter 4, in particular). As a result, we decided to model the glow curve of the main dosimetric peak as a superposition of several first-order 'curvlets', generated using Eq. 2.18.

6.4   Curve-Fitting Using the Marquardt-Levenberg Algorithm

In order to analyze the TL glow curves produced in this study, a computer program was developed which compared the original TL glow curve data with a superposition of several (typically, 40–60) first-order Randall-Wilkins TL curvlets, with activation energy increments

ranging from 0.01 eV to 0.05 eV. The comparison was made using a Marquardt-Levenberg algorithm, which is a non-linear least-squares fitting method to quantitatively evaluate the differences between two sets of data – namely, the original TL glow curve data and the superposition of several first-order Randall-Wilkins curvlets (i.e. the fitted data). The program adjusts the relative populations of each of the curvlets and continuously minimizes the difference between the original and fitted TL glow curves. As a result, the original TL glow curve is 'deconvolved' into a normalized distribution of first-order Randall-Wilkins TL glow curves.

Ideally, this analysis should include the determination of the proper attempt-to-escape frequency factor, s, as well as the activation energy, E_t. However, this requires an additional data set (e.g. the heating rate dependence of the TL glow curve), which is computationally expensive. Such a 3-dimensional ($n(E,s)$, E, s) deconvolution spectra would more closely mimic the current 2-dimensional analysis (E, s) techniques used, however, the current 2-dimensional ($n(E)$, E) deconvolution spectra may be considered a useful starting point. As a result, the attempt-to-escape frequency factor, s, has been assumed to be constant throughout this study.

Figure 6.2 shows a distribution of nine first-order Randall-Wilkins curvlets, along with a computer-generated TL glow curve. The curvlets were generated using Eq. 2.18, with n_0 and s held constant and activation energies incremented by $\Delta E = 0.05$ eV. The activation energy of the TL glow curve was deliberately chosen to coincide with the activation energy of the center curvlet (i.e. $E_5 = 1.50$ eV). As a result, the activation energy distribution that best fits the original TL glow curve data consists of a very narrow band, centered around the center curvlet ($E_5 = 1.50$ eV), with a weighted average activation energy of 1.50 eV as shown
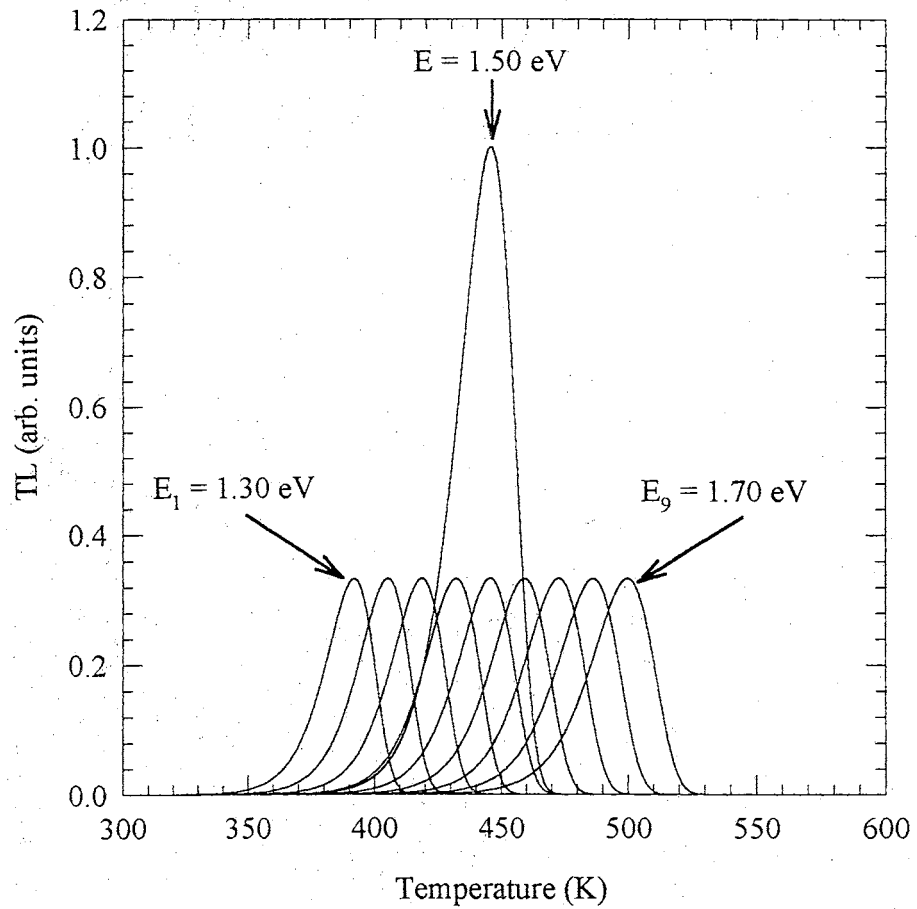
Figure 6.2 - Distribution of First-Order Randall-Wilkins TL Glow Curves. Computer-generated TL glow curve (E = 1.50 eV, s = 10^{14} s^{-1}), along with a distribution of nine first-order Randall-Wilkins 'curvlets' (E$_1$ = 1.30 eV through E$_9$ = 1.70 eV, ΔE = 0.50 eV, s = 10^{14} s^{-1}).

in Figure 6.3. Similarly, should the distribution not contain a curvlet whose activation energy precisely matches that of the original TL glow curve, the resulting activation energy distribution will still produce a weighted average activation energy of 1.50 eV, centered about the two curvlets adjacent to the 1.50 eV region, as displayed in Figure 6.4.

6.5   Deconvolution of TL Glow Curves

The TL glow curves of Figure 6.1 were deconvolved assuming an attempt-to-escape frequency factor of 10^{14} s^{-1} and an activation energy range from 1.30 to 1.60 eV. Figure 6.5 shows the deconvolution activation energy spectrum for the beta-induced TL glow curve of Figure 6.1. The deconvolution spectra clearly show two broad peaks in the distribution, centered around 1.36 eV (peak A) and 1.41 eV (peak B). Figure 6.6 shows the deconvolution spectra for the neutron-induced TL glow curve of Figure 6.1. Once again, two broad peaks appear, centered around 1.36 and 1.41 eV and the ratio of the relative population of peak B to peak A has increased. Similarly, Figure 6.7 shows the deconvolution spectra for the alpha-induced TL glow curve of Figure 6.1. Clearly, the ratio of peak B to peak A increases with higher LET particles. However, as shown in Figure 6.8, the sample-to-sample variability of as-grown α-Al$_2$O$_3$:C crystals can be significant.

6.5.1   Monoenergetic Neutrons and Beta-Particles

A series of experiments were performed to investigate the deconvolved activation energy spectrum dependence on LET. Single crystal α-Al$_2$O$_3$:C samples were annealed at 1175 K for 15 minutes. Several Delrin™ sample holders were machined to hold four α-Al$_2$O$_3$:C samples. Each sample holder was 38.1 mm in diameter and 6.4 mm thick, with a 19.1 mm diameter insert. Each insert contained four radial sample indents. Once the insert is placed

94
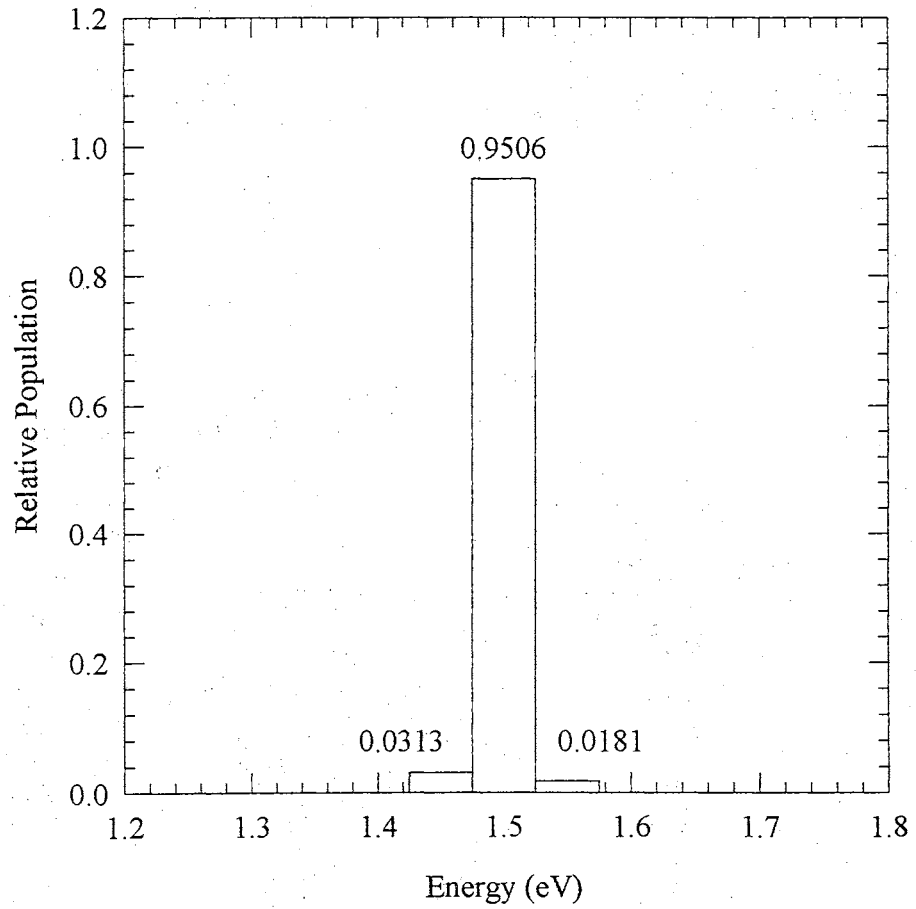
Figure 6.3 - Deconvolution of Activation Energy Spectrum for Single First-Order Randall-Wilkins TL Glow Curve. The spectrum resulting from a deconvolution of the nine first-order Randall-Wilkins 'curvlets' shown in Figure 6.2. Curvlet #5 (E_5 = 1.50 eV) has the same activation energy as the 'original' TL glow curve (E = 1.50 eV). The weighted average of the resulting spectrum has an activation energy of 1.50 eV.

95
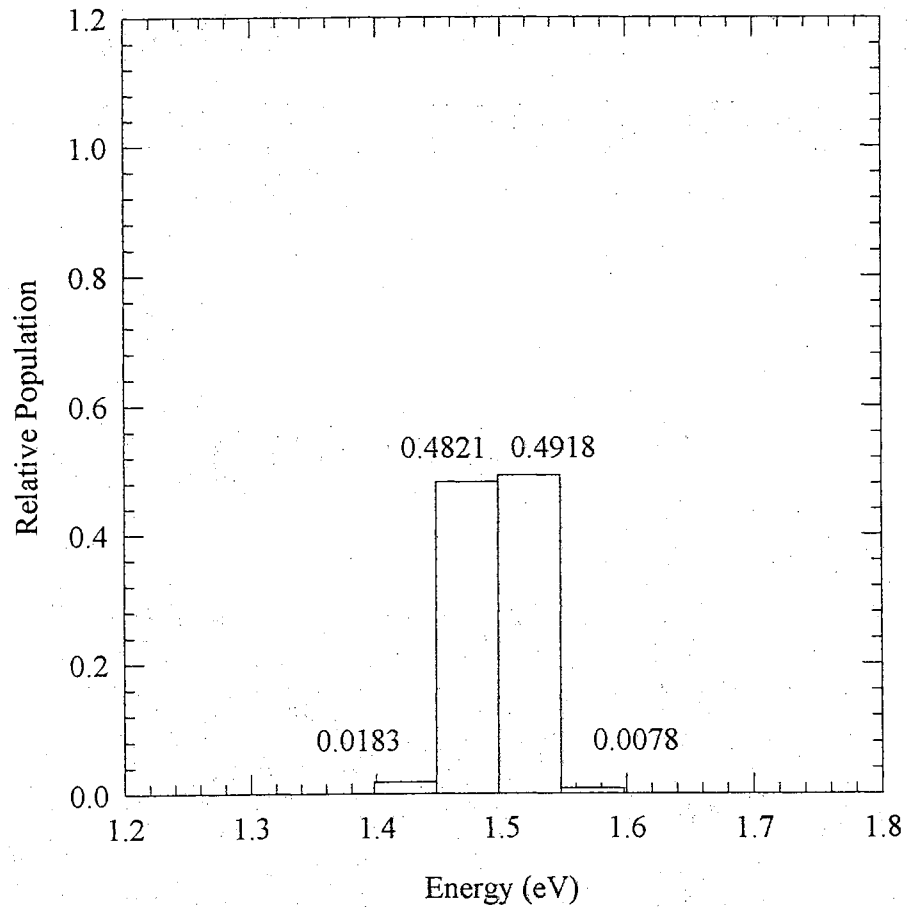
Figure 6.4 - Deconvolution of Activation Energy Spectrum for Single First-Order Randall-Wilkins TL Glow Curve. The spectrum resulting from a deconvolution of nine first-order Randall-Wilkins 'curvlets' similar to those shown in Figure 6.2; however, the distribution range is from $E_1 = 1.323$ eV to $E_9 = 1.723$, $\Delta E = 0.5$ eV, $s = 10^{14}$ s^{-1}. No single curvlet has the same activation energy as the 'original' TL glow curve ($E = 1.50$ eV). The weighted average of the resulting spectrum has an activation energy of 1.50 eV.
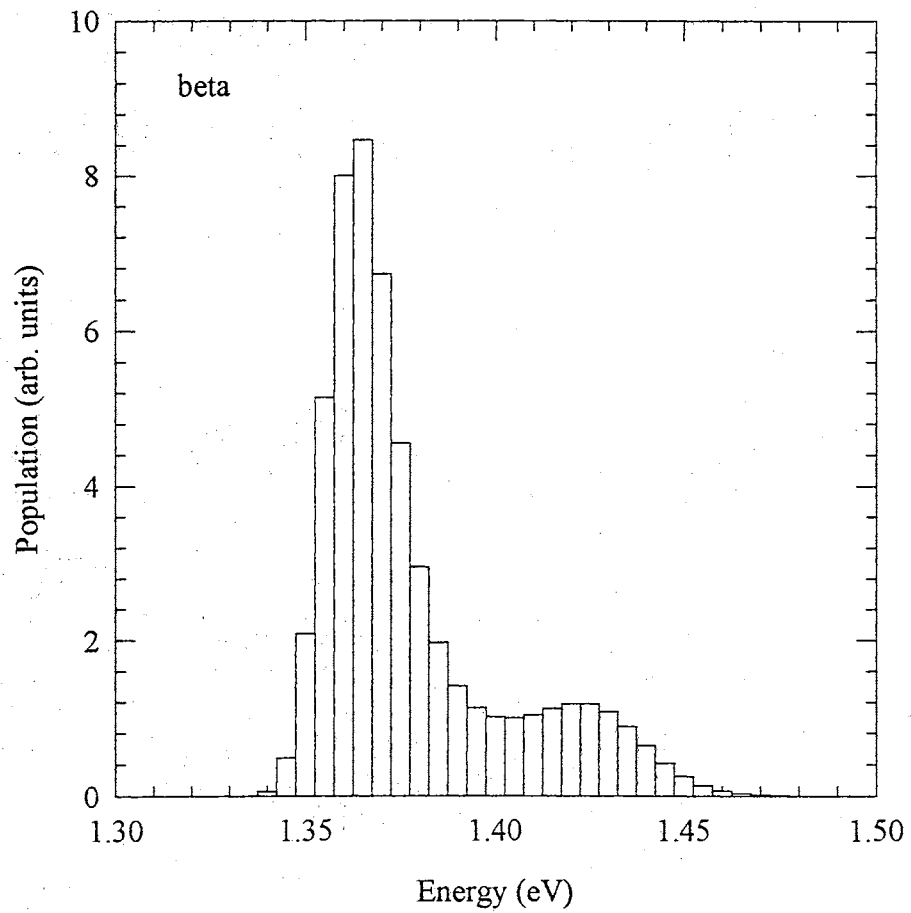
Figure 6.5 - Deconvolution Spectrum of Beta-Induced TL Glow Curve. The deconvolution spectrum of the beta-induced curve of Figure 6.1. The distribution consists of 41 curvlets (E_1 = 1.33 eV to E_{41} = 1.53 eV, ΔE = 0.005 eV, s = 10^{14} s^{-1}).
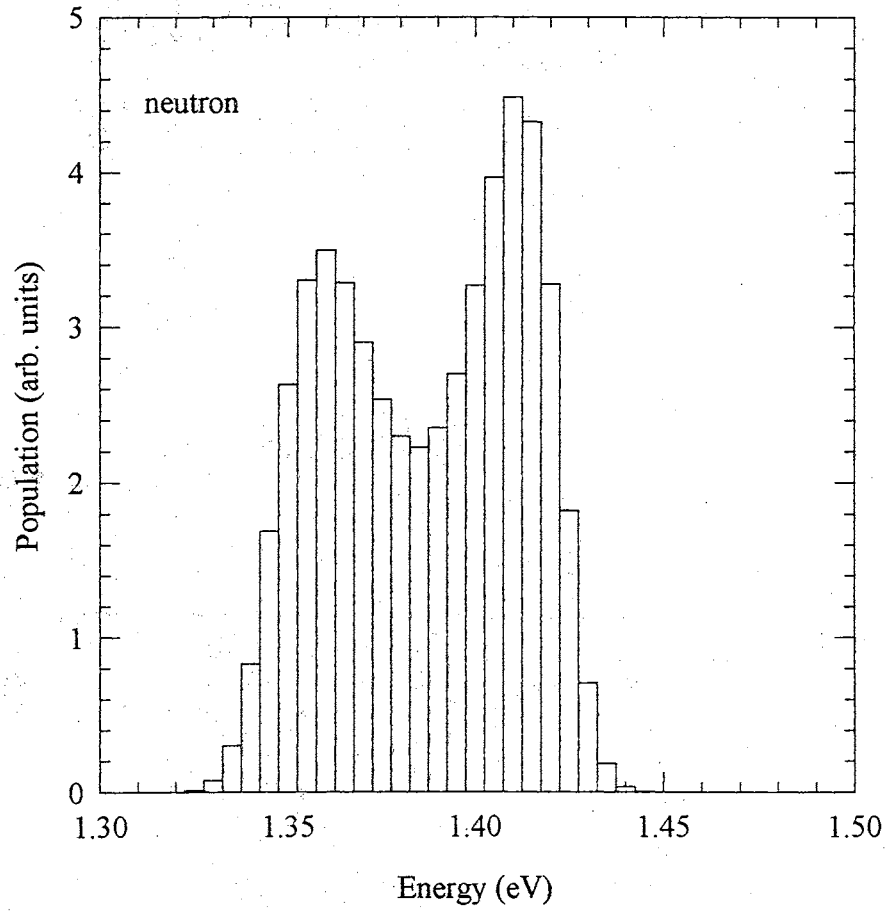
Figure 6.6 - Deconvolution Spectrum of Neutron-Induced TL Glow Curve. The deconvolution spectrum of the neutron-induced curve of Figure 6.1. The distribution consists of 41 curvlets (E_1 = 1.33 eV to E_{41} = 1.53 eV, ΔE = 0.005 eV, s = 10^{14} s^{-1}).
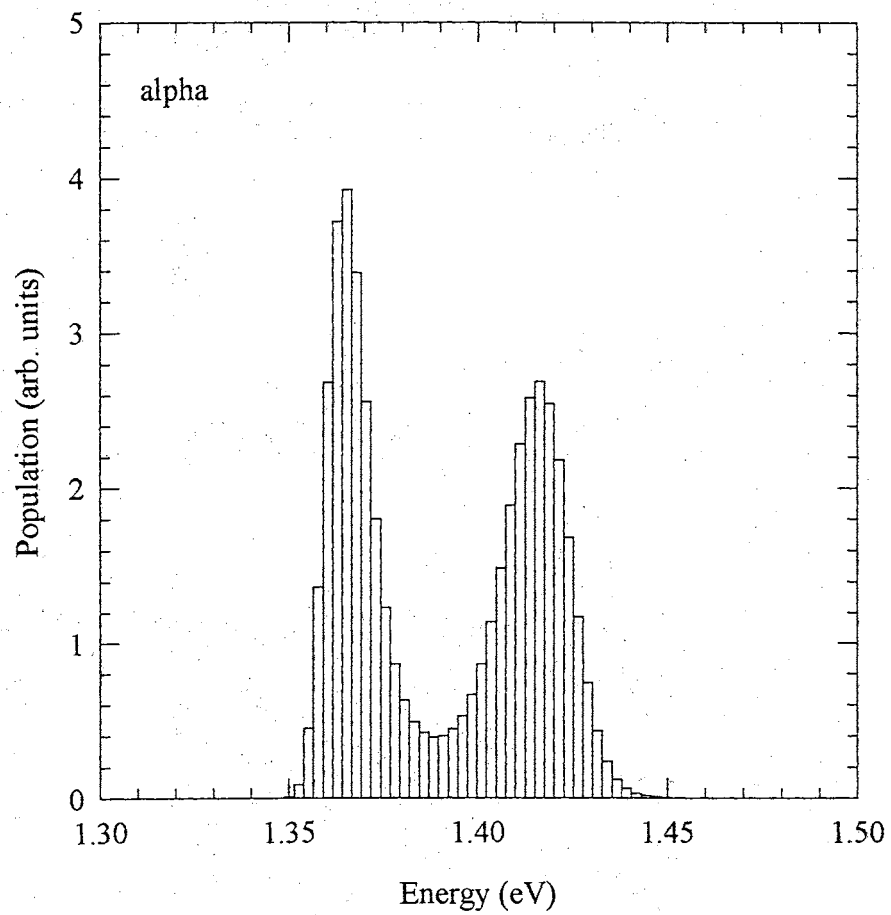
Figure 6.7 - Deconvolution Spectrum of Alpha-Induced TL Glow Curve. The deconvolution spectrum of the alpha-induced curve of Figure 6.1. The distribution consists of 61 curvlets (E_1 = 1.34 eV to E_{61} = 1.49 eV, ΔE = 0.0025 eV, s = 10^{14} s^{-1}).
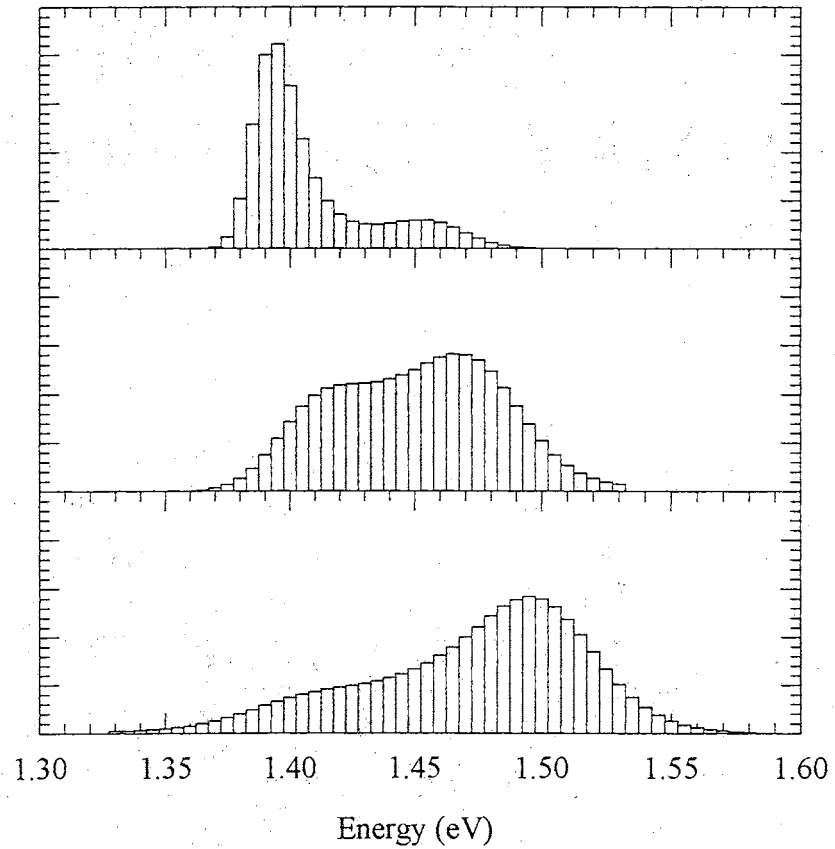
Figure 6.8 - Sample-to-Sample Variability of Deconvolution Spectra. The deconvolution of three arbitrary single crystal α-Al_2O_3:C samples, exposed to 64 mGy, ^{90}Sr/^{90}Y beta-particles. Deconvolution parameters: $s = 10^{14}$ s^{-1} and $\Delta E = 5$ meV.

within the holder, the samples are protected from any light exposure. Eight sample holders were used: six for neutron exposures and two for transit dose controls. (A transit dose is the background radiation exposure that the samples would receive in route to and from the neutron source.)

The samples were irradiated at the Naval Surface Warfare Center's (NSWC) Positive-Ion Accelerator in Silver Spring, MD. Fast, monoenergetic (γ-free) neutrons were produced at the NSWC facility via the $^7\text{Li}(p,n)^7\text{Be}$ reaction. The reaction took place inside a vacuum chamber; however, the neutron irradiations of the sample holders were performed in air. The sample holders were taped to the back end of the target chamber, at a distance of 11.3 cm from the Li_2O source. The irradiation doses were 1 mGy and 100 μGy for neutron energies of 1, 2 and 3 MeV. After receiving their respective neutron doses, the TL of each sample was measured. Following the neutron-induced TL measurements, the samples were annealed at 1175 K for 15 minutes and given a 64 mGy beta dose using a $^{90}\text{Sr}/^{90}\text{Y}$ source. The beta-induced TL of each sample was measured, as well.

The neutron- and beta-induced TL glow curves were deconvolved using 41 first-order Randall-Wilkins curvlets, generated with an attempt-to-escape frequency factor of $s = 10^{14}$ s^{-1} and activation energies ranging from 1.33 eV to 1.53 eV, separated by $\Delta E = 0.005$ eV. The resulting deconvolved activation energy spectra were analyzed by comparing the area under the low energy half of peak A, region 1, with the area under the remaining spectra (i.e. the high energy half of peak A and all of peak B), region 2. As a result, the ratios of region 1 to region 2 for both monoenergetic neutrons and beta-particles can be determined. In addition, the ratio of the neutron to beta ratios can be calculated. The results of all calculations are shown in Table 6.1. Clearly, region 2 is greater for higher LET particles (1, 2 and 3 MeV

101

Table 6.1 - Deconvolution Peak Ratios for NSWC Exposures

Sample	Neutron Energy (MeV)	Neutron Dose (rad)	Region2/Region1 Neutron	Beta	Neutron/Beta
A1	1	0.1150	0.7	0.6	1.1
A2	1	0.1150	0.3	0.2	1.6
A3	1	0.1150	2.4	1.2	2.0
B1	1	0.0115	0.7	0.4	1.6
B2	1	0.0115	1.5	1.1	1.3
B3	1	0.0115	0.7	0.5	1.5
C1	2	0.1120	0.1	0.5	0.2
C2	2	0.1120	0.7	0.4	1.7
C3	2	0.1120	0.9	0.7	1.4
D1	2	0.0112	0.3	0.3	1.0
D2	2	0.0112	0.9	0.8	1.1
D3	2	0.0112	2.0	0.6	3.2
E1	3	0.1386	2.8	2.5	1.1
E2	3	0.1386	1.7	1.4	1.2
E3	3	0.1386	2.5	0.8	2.9
F1	3	0.0145	0.7	0.6	1.2
F2	3	0.0145	0.7	0.4	1.6
F3	3	0.0145	1.0	0.6	1.7

neutrons) than for lower LET particles (beta-particles). In fact, out of 18 samples, only 2 exhibit a lower response for region 2 than expected. However, the results are only qualitative at best, due to the lack of any trends with respect to neutron energy or dose. This is most likely the result of sample-to-sample variability of the as-grown α-Al_2O_3:C crystals.

6.5.2 Alpha and Beta Particles

The alpha- and beta-particle LET dependence of the deconvolved TL glow curves was also investigated using a single crystal α-Al_2O_3:C sample. The sample was annealed at 1175 K for 15 minutes and then sequentially irradiated with varying doses of alpha- (^{244}Cm - 0.4, 1.2 and 4 Gy) and beta-particles (^{90}Sr/^{90}Y - 1, 3 and 10 mGy), so as to form a LET matrix of alpha- and beta- particle exposures. Each element of the resulting 4 x 4 LET matrix (a_0b_0 = no alpha, no beta, while a_3b_3 = 4 Gy alpha + 10 mGy beta) was deconvolved using 51 first-order Randall-Wilkins curvlets, generated with an attempt-to-escape frequency factor of $s = 10^{14}$ s^{-1} and activation energies ranging from 1.33 eV to 1.58 eV, separated by $\Delta E = 0.005$ eV. The resulting deconvolved activation energy spectra were analyzed as described above. The results of all calculations are shown in Table 6.2. Once again, region 2 is clearly greater for higher LET particles (alpha-particle irradiations) than for lower LET particles (beta-particles). However, while row a_0, which represents no alpha-particle exposure, exhibits a response in keeping with the results of the monoenergetic neutron study (i.e. lower LET irradiation), the results are only qualitative. Similarly, the remaining elements, all of which received some alpha-particle exposure, follow the trends established above for higher LET irradiation. Thus, while the ratios of region 2 to region 1 are generally higher for higher LET particles, the absolute value of the ratio does not solely indicate the presence or absence of

Table 6.2 - Alpha-Particle and Beta-Particle LET Matrix

Matrix Element	Alpha Dose (Gy)	Beta Dose (mGy)	Region1	Region2	Region2/Region1
a_1b_0	40	0	25.2	25.8	1.0
a_2b_0	120	0	17.5	32.9	1.9
a_3b_0	400	0	15.3	35.3	2.3
a_0b_1	0	1	23.5	28.0	1.2
a_1b_1	40	1	10.3	41.1	4.0
a_2b_1	120	1	15.3	35.6	2.3
a_3b_1	400	1	17.8	32.9	1.8
a_0b_2	0	3	12.6	38.5	3.1
a_1b_2	40	3	18.6	33.1	1.8
a_2b_2	120	3	25.1	25.1	1.0
a_3b_2	400	3	15.9	34.8	2.2
a_0b_3	0	10	22.4	29.3	1.3
a_1b_3	40	10	9.8	42.1	4.3
a_2b_3	120	10	8.2	42.7	5.2
a_3b_3	400	10	12.6	38.3	3.0

higher LET particles. Once again, this appears to corroborate the view that the sample-to-sample variability of the as-grown α-Al$_2$O$_3$:C crystals is significant.

6.6 Summary

The method of TL glow curve deconvolution described in this chapter clearly demonstrates the ability to detect the presence or absence of high LET particle exposure. However, the current technique does not allow clear discrimination of LET specific information (i.e. particle type) and, as a result, cannot yet be used as a quantitative dosimetric tool. This may be due to the irreproducible nature of the main dosimetric TL peak of α-Al$_2$O$_3$:C, rather than the idea of deconvolution itself. Once a more homogeneous main dosimetric TL peak is produced (either through improved crystal growth techniques or the use of powders) this method may indeed prove to be beneficial to the dosimetry community.

One important consideration in the present discussion involves the use of a constant attempt-to-escape frequency factor, s. The current program allows for multiple values of s; however, in order to produce realistic fits, an additional free parameter (such as TL glow curve heating rate dependence) must be included in the data. Unfortunately, the size of the resulting matrix becomes very large, very quickly and is computationally expensive. Nonetheless, this aspect of deconvolution has not been tested and may very well produce additional insight into the LET and dosimetric properties of this material.

Chapter 7

7 Alteration of α-Al$_2$O$_3$:C Dosimetric Properties by Anneal in O$_2$ Atmosphere

7.1 Introduction

As mentioned earlier, the neutron-induced TL response of α-Al$_2$O$_3$:C is only ~4% that of gammas. Since the gamma-induced TL results from charge carrier interactions with the F- and F$^+$-centers of α-Al$_2$O$_3$:C, and these centers result from oxygen vacancies introduced during the growth process, the elimination of some of these vacancies should decrease the gamma sensitivity of this material. As a result, the neutron response, relative to the gamma response, of this material may increase.

Alternatively, the desensitized material may permit the detection of changes in the concentration of neutron-induced oxygen-vacancies. This may take the form of increased gamma-induced TL sensitivity following neutron irradiation. In addition, the UV-induced TL response of this material may change due to an increase in neutron-induced defects. The UV-induced TL can be used as a probe of the oxygen-vacancy concentration, since UV exposure can excite electrons from existing F-centers (producing F$^+$-centers) into the conduction band and, subsequently electron traps. Both methods may, in turn, lead to an indirect measurement of an increased neutron-induced response, resulting from neutron-induced oxygen-vacancies.

One method of decreasing the oxygen-vacancy concentration would involve the high temperature anneal of α-Al$_2$O$_3$:C fine powder in an oxygen atmosphere. This should increase the diffusion of oxygen atoms into the α-Al$_2$O$_3$:C crystal lattice, thereby decreasing the

concentration of oxygen-vacancies. Once the powder had been annealed, the degree of desensitization could be determined by measuring the initial UV-induced TL (as a measure of the F-center (oxygen-vacancy) concentration and TL sensitivity), followed by gamma-induced TL (as a measure of TL sensitivity). The neutron-induced TL could then be measured, thus providing a determination of the neutron sensitivity and possibly producing additional oxygen-vacancies. A second UV-induced TL measurement should then increase due to an increase of (neutron-induced) oxygen-vacancies. This was the method adopted for this study.

7.2   Experimental

Several grams of α-Al_2O_3:C powder were provided by Stillwater Sciences, LLC. The four powder grain sizes ranged from 10 μm ± 5 μm to 40 μm ± 5 μm, in 10 μm increments. Each grain size was divided into four separate samples of 1–2 grams each. Each sample was placed inside a quartz test tube (8 mm inner diameter, 12 mm outer diameter) using a quartz funnel, which was designed to deposit the α-Al_2O_3:C powder at the bottom of the test tube with no residue on the upper test tube walls. (This was an important consideration, in order to prevent contamination, and subsequent weakening, of the quartz wall, once sealed.) Each test tube was evacuated and backfilled with 1 atm of oxygen using a pressure manifold, as shown in Figure 7.1. The lower portion of each test tube was cooled in liquid nitrogen to create a partial vacuum within the test tube. Each test tube was sealed, resulting in a quartz ampule, approximately 10 cm in length, containing α-Al_2O_3:C powder in an oxygen atmosphere.

The α-Al_2O_3:C powder was evenly distributed throughout the ampules and the ampules were placed in a 375 K tube oven. The temperature of the tube oven was ramped to 1375 K
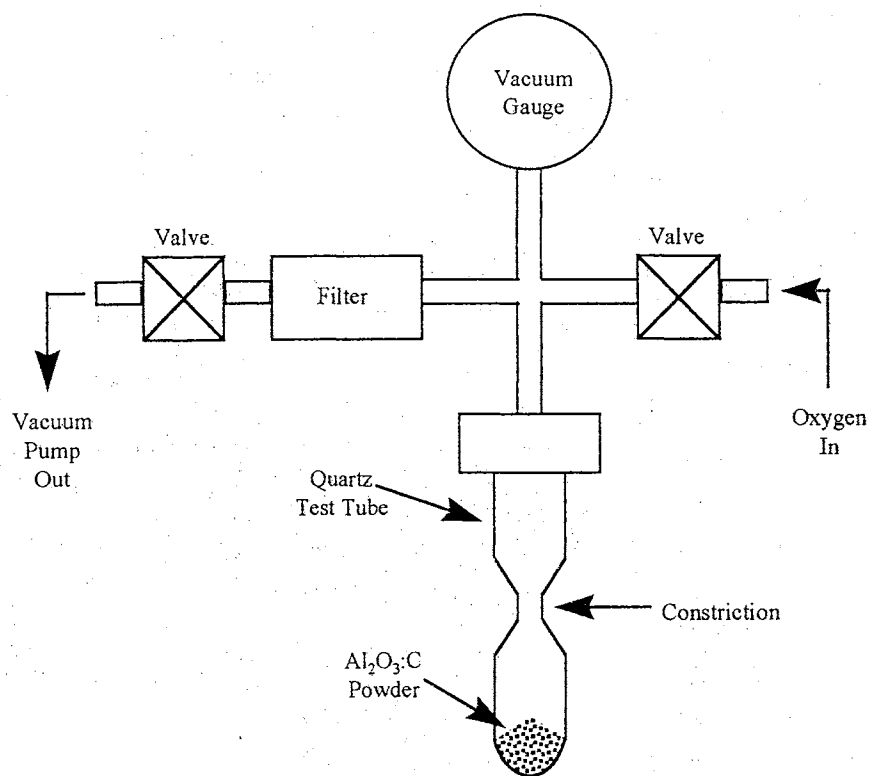
107

Figure 7.1- Schematic Diagram of Pressure Manifold. A schematic diagram of the pressure manifold used to evacuate the quartz test tubes, prior to backfilling with 1 atmosphere of oxygen. The test tubes were subsequently sealed at the constriction shown, resulting in an ampule approximately 10 cm in length.

over approximately 90 minutes. The ampules were annealed in the tube oven at 1375 K for either, 0.33, 1.0, 3.0 or 10 hours. Once the appropriate time had elapsed, the tube oven was cooled to 375 K over approximately 90 minutes. The ampules were removed from the tube oven and allowed to reach room temperature. In order to facilitate removal of as much α-Al_2O_3:C powder as possible and minimize the amount of quartz contamination, the ampules were scored with a file and wrapped with several layers of duct tape. Several light taps with a hammer near the score line cracked the ampules along the score line. Careful removal of the duct tape allowed extraction of the annealed α-Al_2O_3:C powder.

Samples were made from the annealed powder by placing 18 mg of powder in the center of a 1 cm diameter aluminum disk (0.5 mm thick). Approximately 0.05 ml methanol was placed on the disk with an eye dropper and the powder was evenly distributed with the rounded end of a spatula. Each sample was dried for 1 minute at 550 K. This process was repeated 3 times for each grain size (4) and each anneal time (4), resulting in 3 matrices of 16 elements each.

The UV-induced TL of each sample was measured, prior to any irradiations, using a 30 W deuterium lamp. The sample was placed approximately 4 cm from the deuterium lamp, with the height being adjusted slightly to maintain a constant energy flux density of 0.075 μW cm^{-2}. Each sample was illuminated for 10 minutes and the resulting UV-induced TL was measured. A small gamma test dose of 500 mGy ^{60}Co was delivered to each sample and the resulting gamma-induced TL was measured. Following these measurements, the samples were placed in a ^{239}PuBe neutron source (6 x 10^5 neutrons s^{-1}) for 75 hours delivering approximately 50 mGy each of neutrons and gammas. The resulting neutron- and gamma-induced TL was

measured for each sample. Finally, a post-neutron UV-induced TL measurement was made, using the same illumination parameters discussed earlier.

The TL measurements were performed in a nitrogen atmosphere at a partial vacuum of 600 torr. The emission was detected using an EMI 9635QB photomultiplier tube at ambient temperature in the integrated current mode. No filters were used for the TL output. In all cases, the heating rate was 2.0 K s^{-1}.

7.3   Changes in TL Sensitivity

In general, the TL sensitivity of the oxygen annealed samples is ~3 orders of magnitude smaller than that of the unannealed powder. Figure 7.2 compares the gamma-induced TL signals for the 40 μm powder, with anneal times of 0, 0.33 and 10 hours. Similarly, Figure 7.3 compares the TL signals for the 10 μm powder, with the same anneal times. In addition to changes in sensitivity, Figures 7.2 and 7.3 clearly show changes in the TL glow curve shapes associated with the high temperature anneal in an oxygen atmosphere.

Figure 7.4 compares the powder grain size dependence of the normalized gamma-induced (500 mGy, ^{60}Co) TL sensitivity changes resulting from different anneal times. The data show a relatively flat relationship for normalized TL sensitivity changes, as a function of powder grain size. (The exception to this observation being the data for the 30 μm powder. In general, this data set did not behave in a manner similar to that of the other powder grain sizes.)

The neutron-induced (50 mGy each, neutron and gamma; ^{239}PuBe) TL sensitivity is shown in Figure 7.5, as a function of powder grain size, for the various anneal times used in this

110

Figure 7.2 - Gamma-Induced TL of 40 μm Powder. The gamma-induced (500 mGy, ^{60}Co) TL of the 40 μm grain size powder, as a function of the anneal times shown. The samples were irradiated at room temperature.
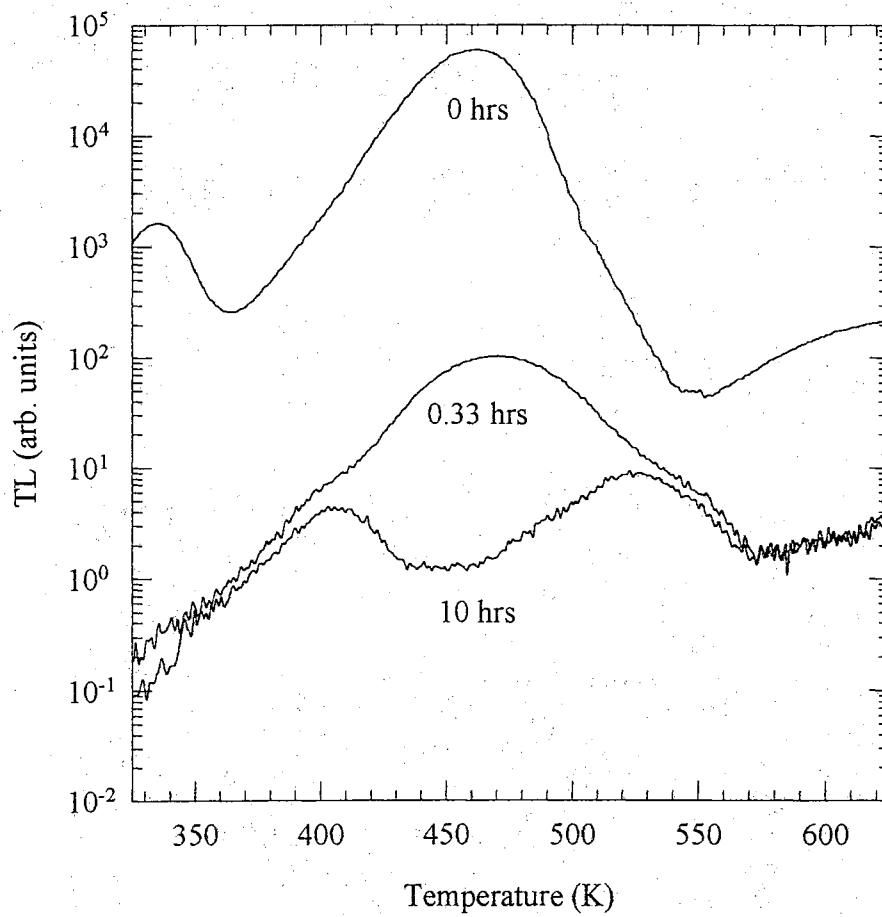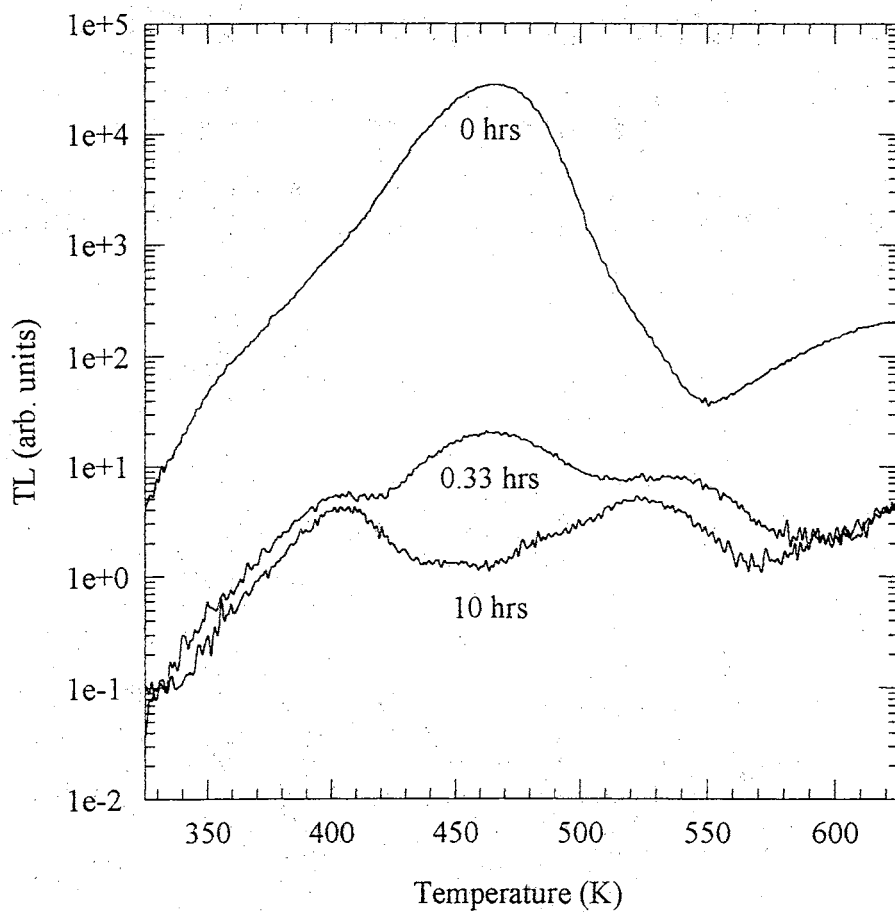
Figure 7.3 - Gamma-Induced TL of 20 μm Powder. The gamma-induced (500 mGy, ^{60}Co) TL of the 20 μm grain size powder, as a function of the anneal times shown. The samples were irradiated at room temperature.
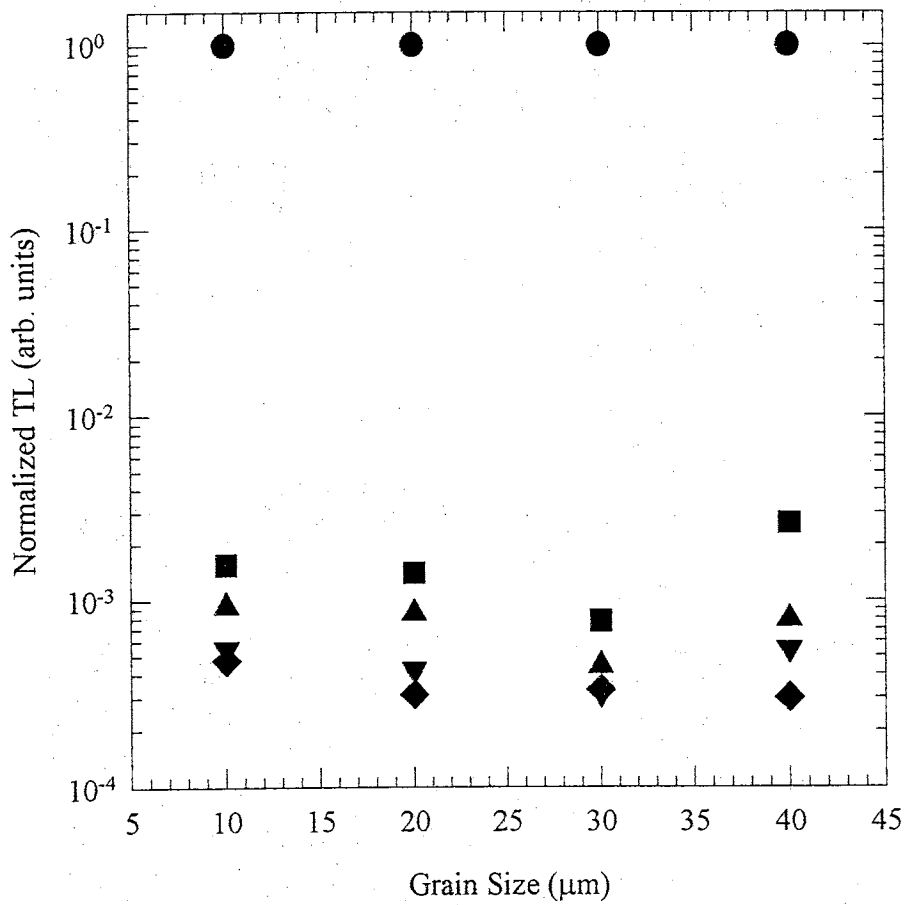
Figure 7.4 - Normalized Gamma-Induced TL. The gamma-induced (500 mGy, ^{60}Co) TL, as a function of grain size, normalized to that of the unannealed powders (anneal time - 0 hrs). The samples were irradiated at room temperature. Symbols shown for anneal times: filled circle - 0 hrs; filled square - 0.33 hrs; filled triangle - 1.0 hrs; filled inverted triangle - 3.0 hrs; filled diamond - 10 hrs.

Figure 7.5 - Neutron-Induced TL. The neutron-induced (50 mGy each, neutron and gamma; ^{239}PuBe) TL, as a function of grain size, for an anneal time of 0.33 hrs. The samples were irradiated at room temperature.

study. While the general sensitivity is low, the data show similar decreases in sensitivity, with respect to grain size and anneal time, as in the case of the gamma-induced TL.

The pre-neutron exposure UV-induced TL is displayed in Figures 7.6 and 7.7, for the 40 μm and 20 μm powder grain sizes, respectively. A comp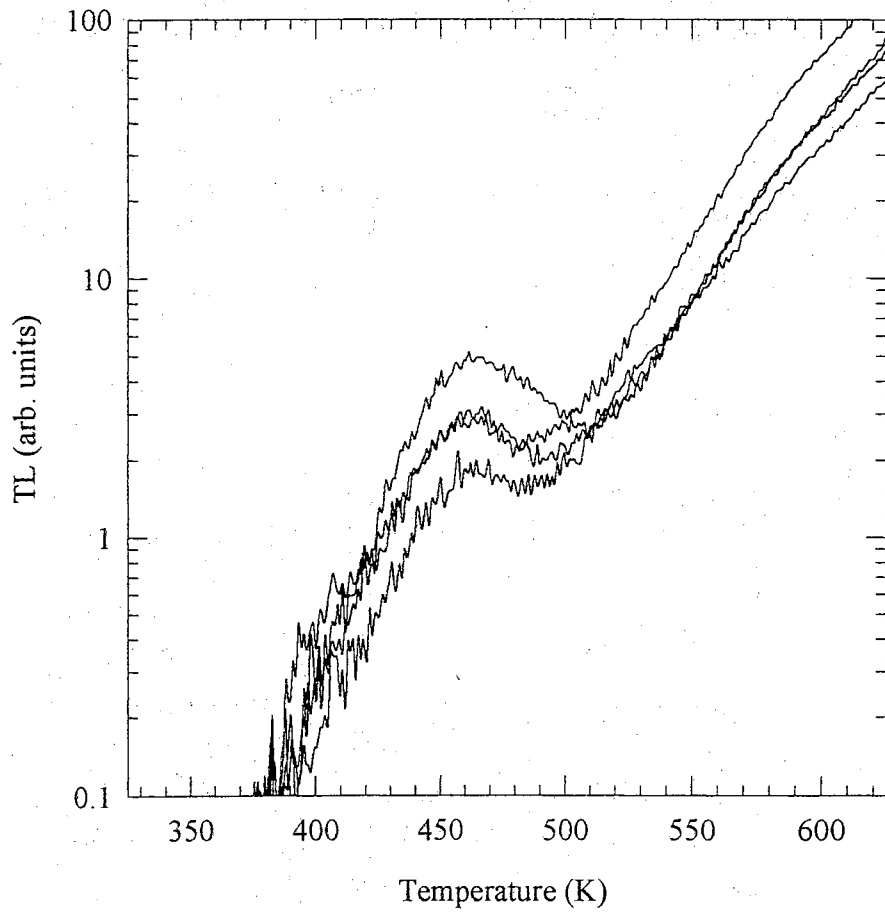arison of these figures shows a decrease in the UV-induced TL response of the thermochemically treated α-Al$_2$O$_3$:C powder, with respect to grain size and anneal time. Figures 7.8 and 7.9 show the post-neutron exposure UV-induced TL, for the 40 μm and 20 μm powder grain sizes, respectively. Once again, the thermochemically treated α-Al$_2$O$_3$:C powder sensitivity decreases with respect to grain size and anneal time. However, another interesting result can be seen when comparing Figure 7.6 with Figure 7.8 and Figure 7.7 with Figure 7.9. In both cases, the UV-induced TL sensitivity decreases following exposure to neutrons. This same result was seen in the 30 μm and 10 μm powders, as well.

The average ratios of the post-neutron to pre-neutron exposure UV-induced TL for each grain size and anneal time is summarized in Table 7.1. This data is displayed in Figure 7.10, as a function of powder grain size, for the anneal times used in this study. The results of this experiment suggest a general *decrease* in the UV-induced TL, following irradiation with neutrons. Furthermore, this effect appears to be more pronounced in the larger grain sizes following longer anneal times.

7.4   Deconvolution of Glow Curves

The TL glow curves of this study were deconvolved using a distribution of 31 first-order Randall-Wilkins curvlets separated by $\Delta E = 0.020$ eV and a constant attempt-to-escape frequency factor of 10^{14} s^{-1}. The area of the TL glow curves have been normalized prior to

Figure 7.6 - UV-Induced TL Spectra of 40 μm Powder Prior to Neutron Exposure. The pre-neutron exposure UV-induced TL of the 40 μm powder, as a function of anneal time.

116
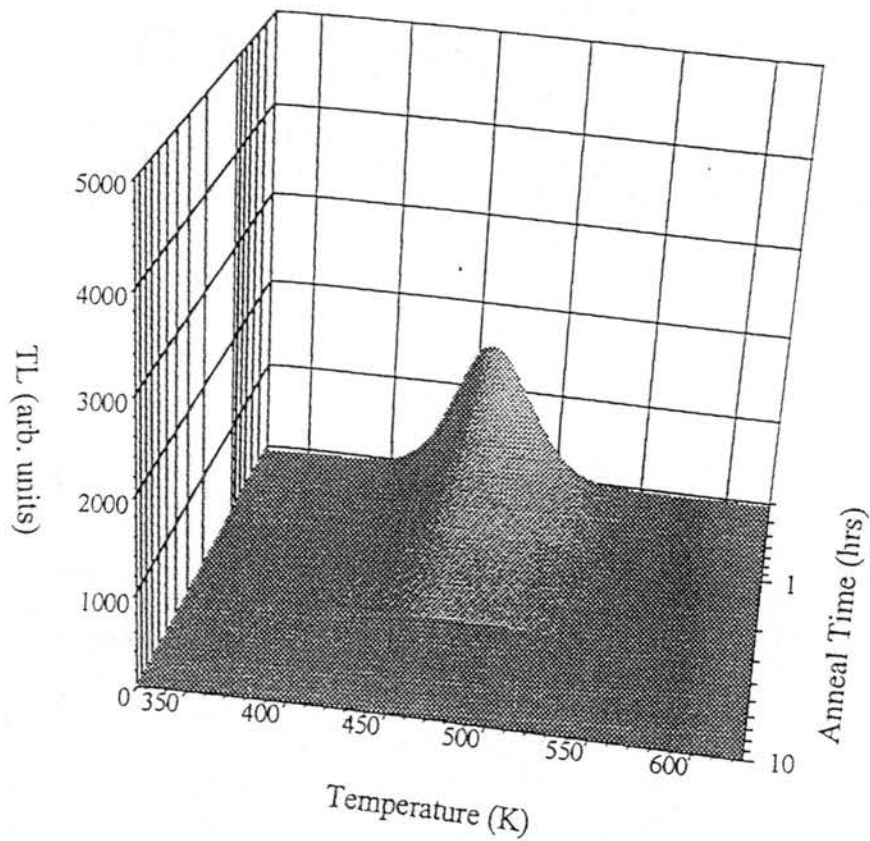
Figure 7.7 - UV-Induced TL Spectra of 20 μm Powder Prior to Neutron Exposure. The pre-neutron exposure UV-induced TL of the 20 μm powder, as a function of anneal time.
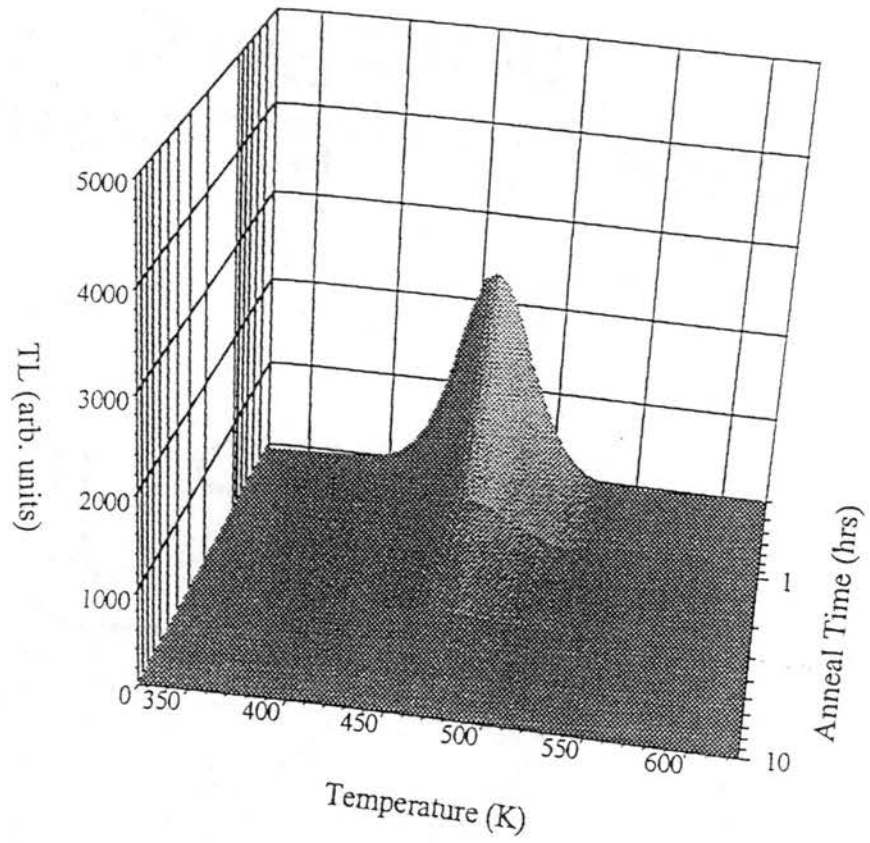
Figure 7.8 - UV-Induced TL Spectra of 40 μm Powder Following Neutron Exposure. The post-neutron exposure UV-induced TL of the 40 μm powder, as a function of anneal time.
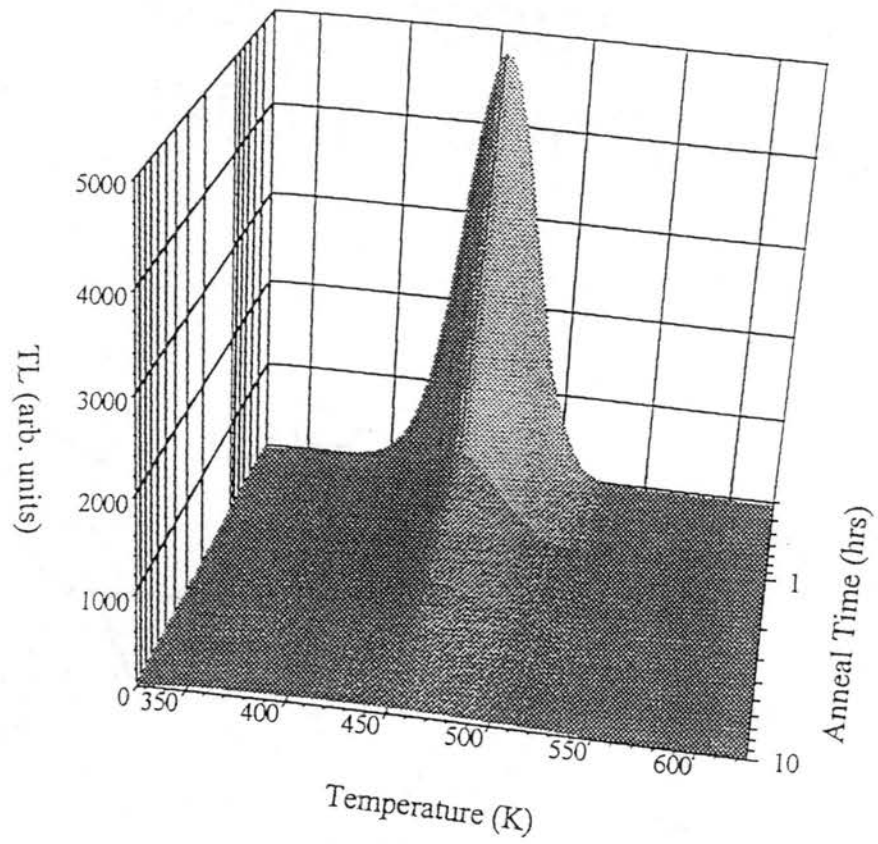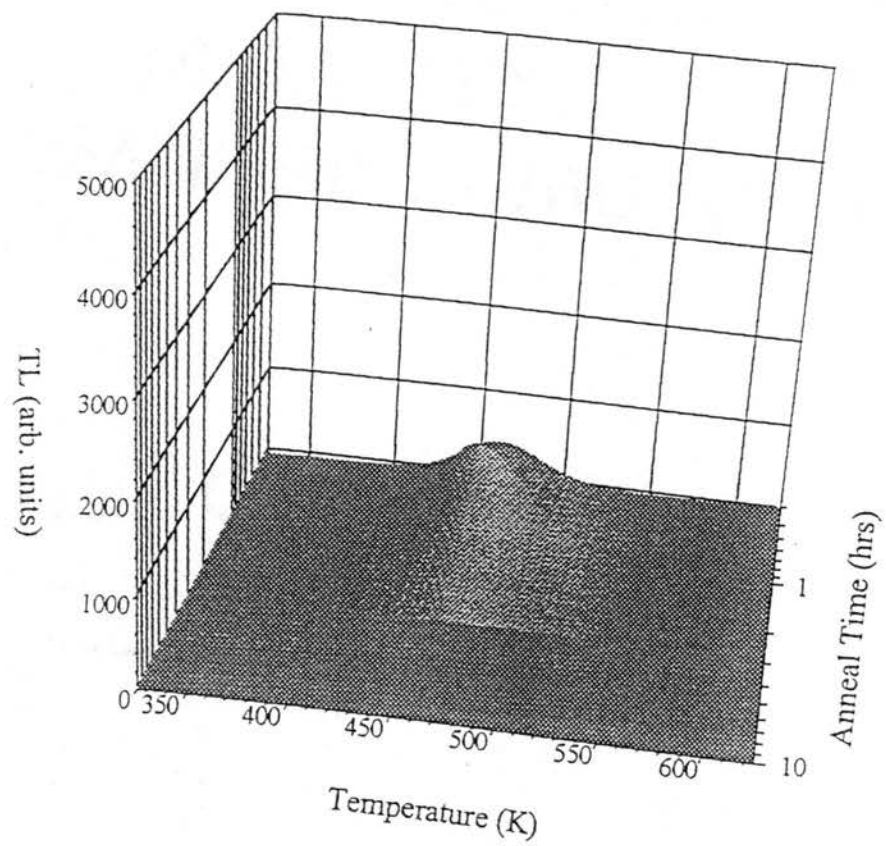
Figure 7.9 - UV-Induced TL Spectra of 20 μm Powder Following Neutron Exposure. The post-neutron exposure UV-induced TL of the 20 μm powder, as a function of anneal time.

Table 7.1 - Average Post-Neutron Relative to Pre-Neutron UV-Induced TL

Powder Grain Size (μm)	Anneal Time (hrs.)			
	0.33	1.0	3.0	10
10	0.52 ± 0.15	0.94 ± 0.45	0.82 ± 0.05	0.87 ± 0.27
20	0.29 ± 0.12	0.92 ± 0.63	0.75 ± 0.45	0.24 ± 0.08
30	0.38 ± 0.27	0.50 ± 0.19	0.41 ± 0.24	0.12 ± 0.05
40	0.56 ± 0.11	0.73 ± 0.40	0.34 ± 0.22	0.20 ± 0.13
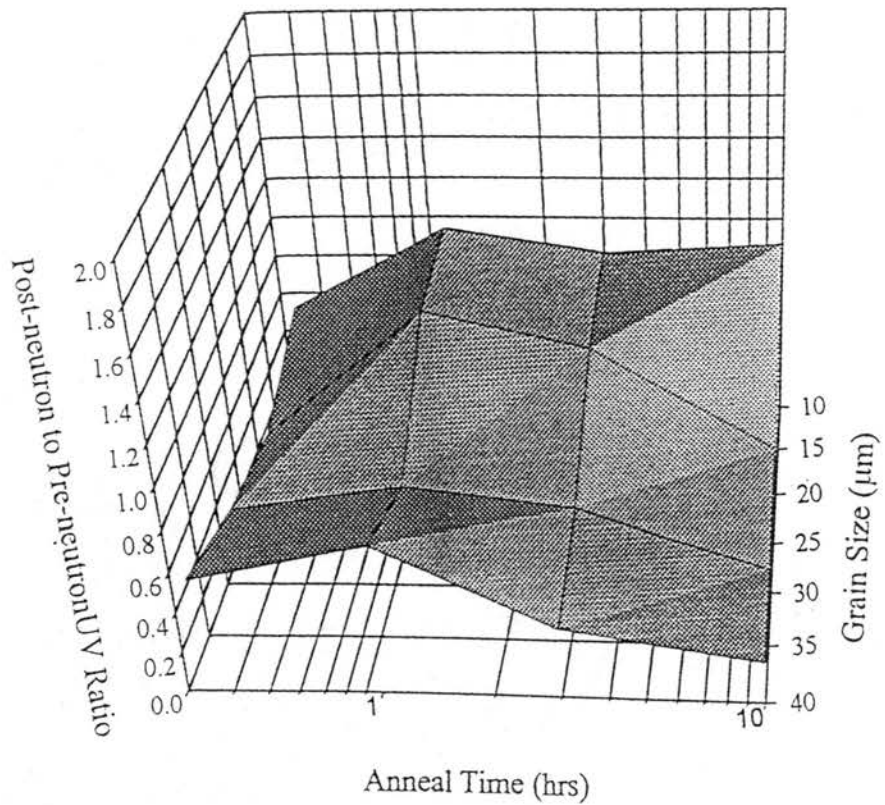
Figure 7.10 - Ratios of Post-Neutron to Pre-Neutron UV-Induced TL. The ratios of the post-neutron to pre-neutron UV-induced TL, as a function of grain size and anneal time (see Table 7.1).

deconvolution. As a result, the deconvolution spectra are normalized, such that

$$\int_{E_A}^{E_B} n(E)\,dE = 1. \tag{7.1}$$

Figure 7.11 shows the deconvolved activation energy spectra for the glow curves of Figure 7.6 (40 μm, pre-neutron UV-induced TL), while Figure 7.12 shows the same for the glow curves of Figure 7.7 (20 μm, pre-neutron UV-induced TL). For comparison, the glow curves of Figure 7.8 (40 μm, post-neutron UV-induced TL) were deconvolved, as shown in Figure 7.13. Similarly, the glow curves of Figure 7.9 (20 μm, post-neutron UV-induced TL) were deconvolved and are displayed in Figure 7.14. The deconvolved spectra of the pre- and post-neutron UV-induced TL do not show any grossly distinct features, which might have been used as a means of determining whether the sample had previously been exposed to higher LET particles.

The gamma-induced TL for the 40 μm samples is shown in Figure 7.15. The resulting deconvolution spectra is displayed in Figure 7.16. The data of Figure 7.15 suggest a *complete absence of F-center luminescence* for longer anneal times. Similarly, the gamma-induced TL for the 20 μm samples is shown in Figure 7.17, while the subsequent deconvolution spectra in displayed in Figure 7.18. As with the deconvolved spectra of the 40 μm samples, the 20 μm samples show no indication of F-center luminescence, following an oxygen atmosphere anneal for relatively long times.

Figure 7.11 - Deconvolution Spectra of 40 μm Powder Pre-Neutron UV-Induced TL. The deconvolved activation energy spectra of the TL glow curves shown in Figure 7.6. Deconvolution parameters: 31 curvlets, $s = 10^{14}$ s^{-1} and $\Delta E = 20$ meV.

Figure 7.12 - Deconvolution Spectra of 20 μm Powder Pre-Neutron UV-Induced TL. The deconvolved activation energy spectra of the TL glow curves shown in Figure 7.7. Deconvolution parameters: 31 curvlets, s = 10^{14} s^{-1} and ΔE = 20 meV.
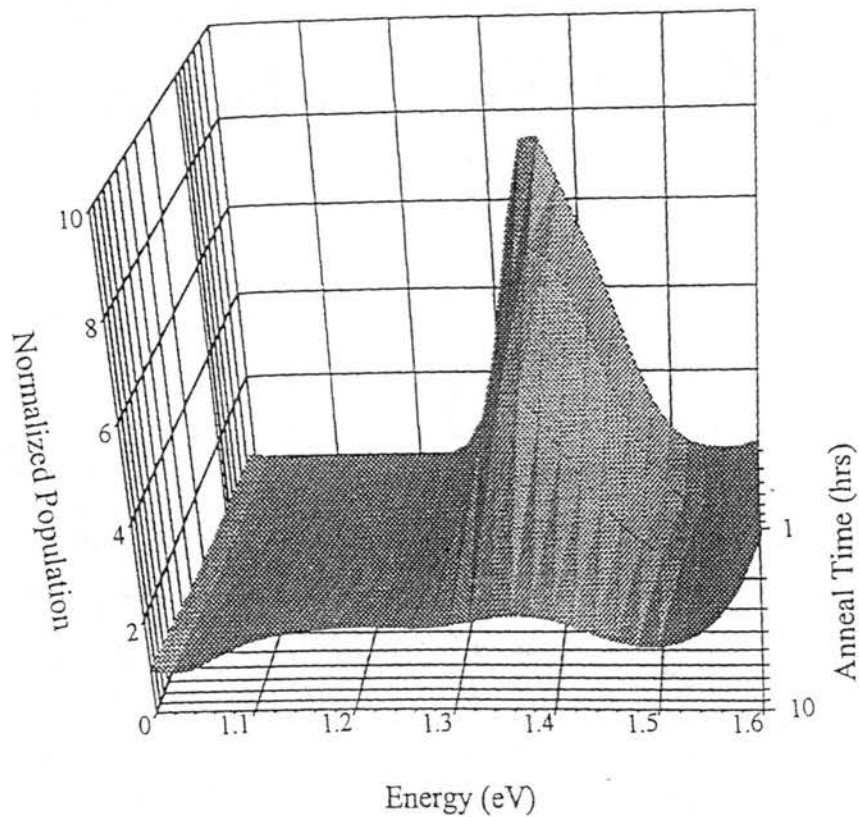
Figure 7.13 - Deconvolution Spectra of 40 µm Powder Post-Neutron UV-Induced TL. The deconvolved activation energy spectra of the TL glow curves shown in Figure 7.8. Deconvolution parameters: 31 curvlets, s = 10^{14} s^{-1} and ΔE = 20 meV.
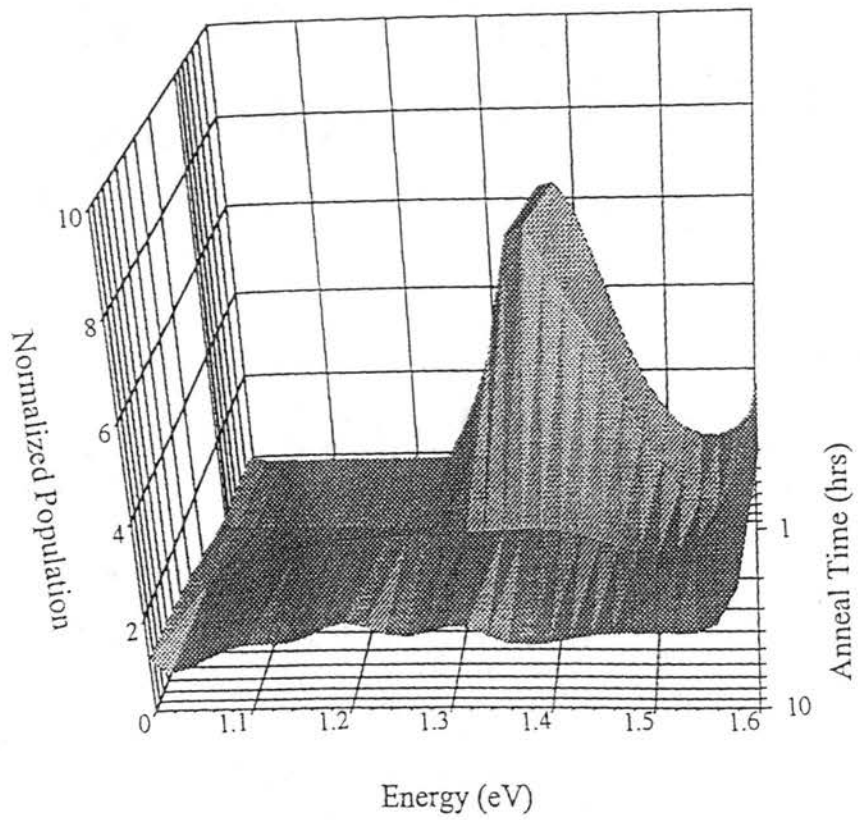
Figure 7.14 - Deconvolution Spectra of 20 μm Powder Post-Neutron UV-Induced TL. The deconvolved activation energy spectra of the TL glow curves shown in Figure 7.9. Deconvolution parameters: 31 curvlets, $s = 10^{14}$ s^{-1} and $\Delta E = 20$ meV.
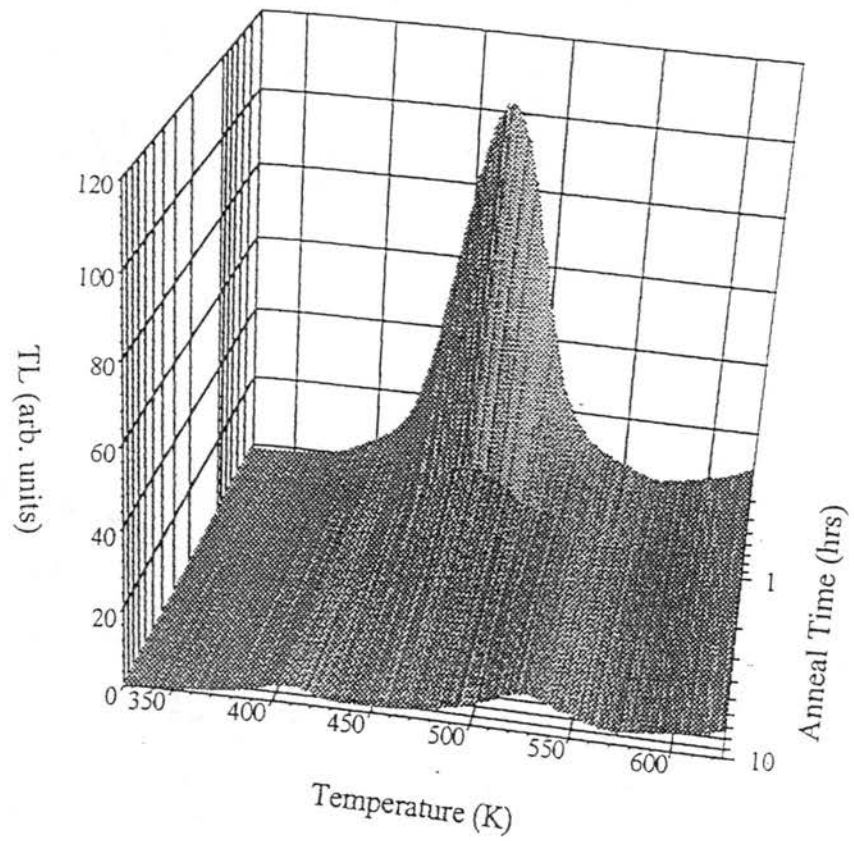
Figure 7.15 - Gamma-Induced TL Spectra for 40 μm Powder. The gamma-induced (500 mGy, ⁶⁰Co) TL of the 40 μm powder, as a function of anneal time.
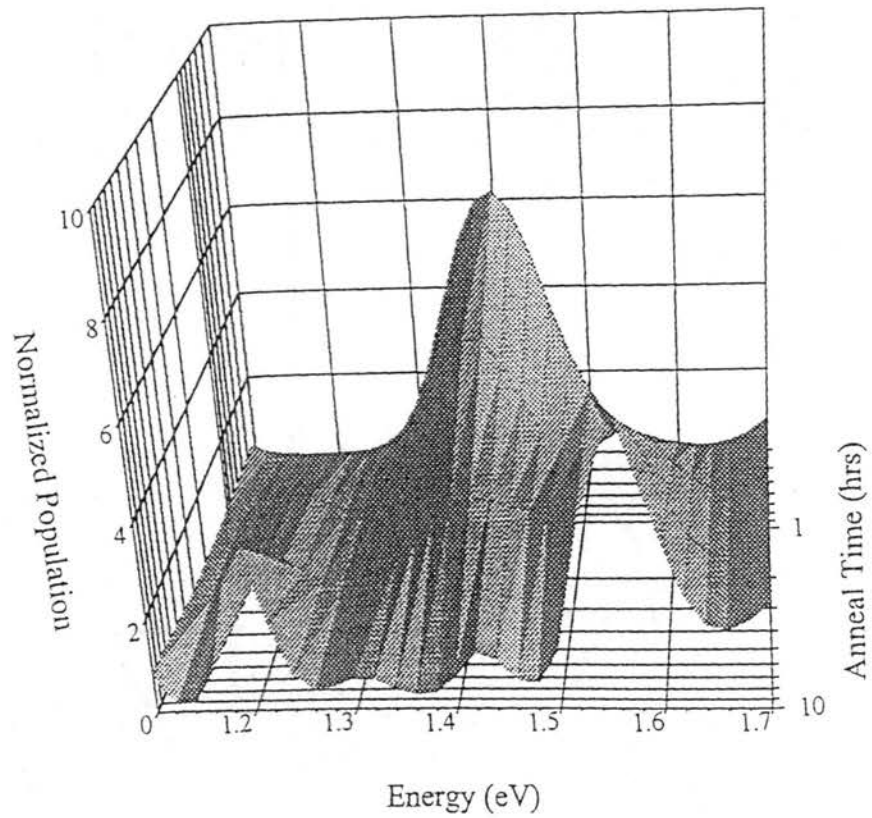
Figure 7.16 - Deconvolution Spectra of 40 μm Powder Gamma-Induced TL. The deconvolved activation energy spectra of the TL glow curves shown in Figure 7.15. Deconvolution parameters: 31 curvlets, s = 10^{14} s^{-1} and ΔE = 20 meV.
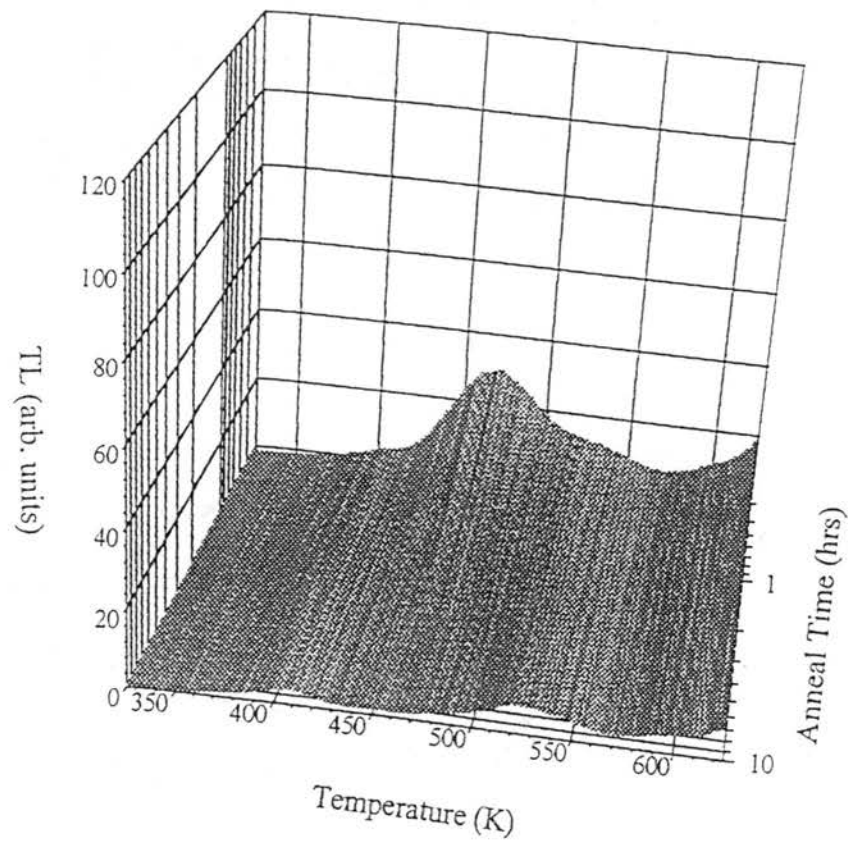
Figure 7.17 - Gamma-Induced TL Spectra for 20 μm Powder. The gamma-induced (500 mGy, ⁶⁰Co) TL of the 20 μm powder, as a function of anneal time.
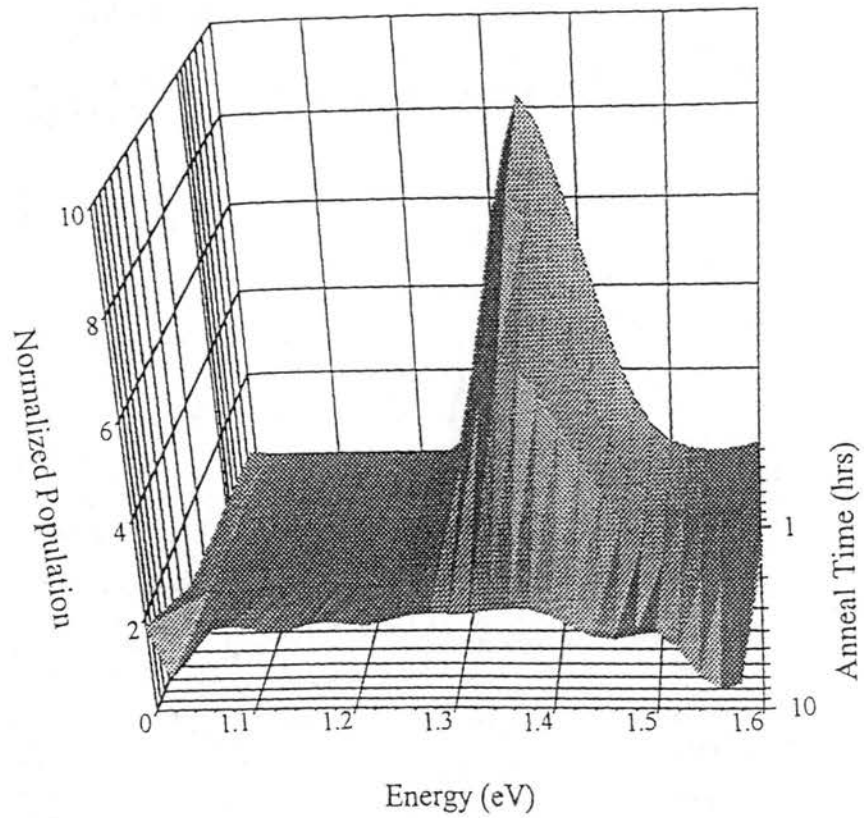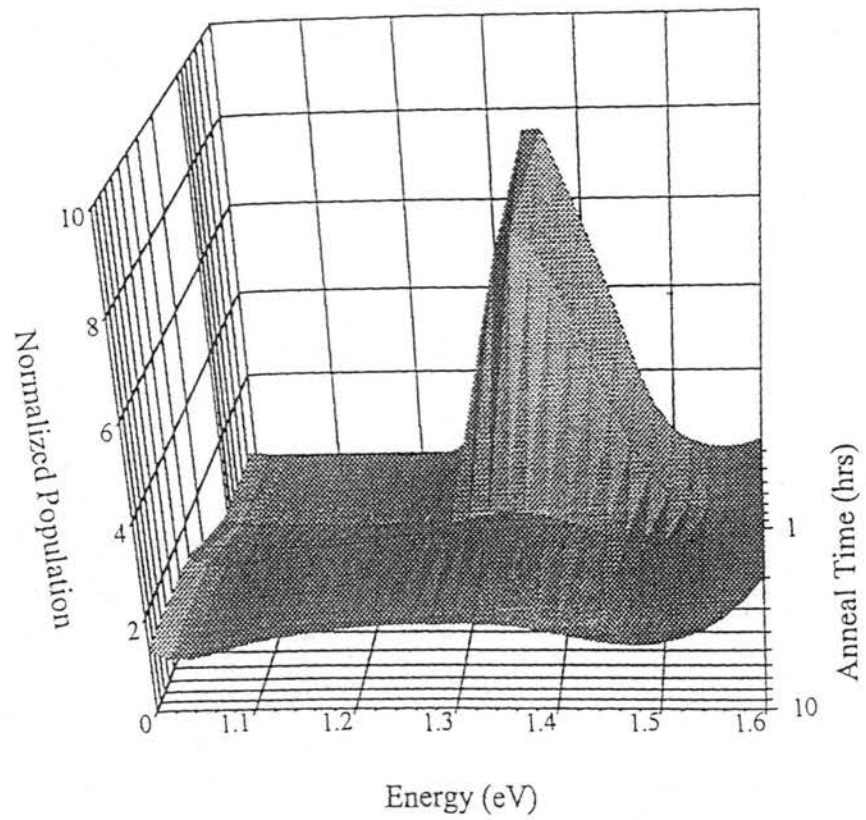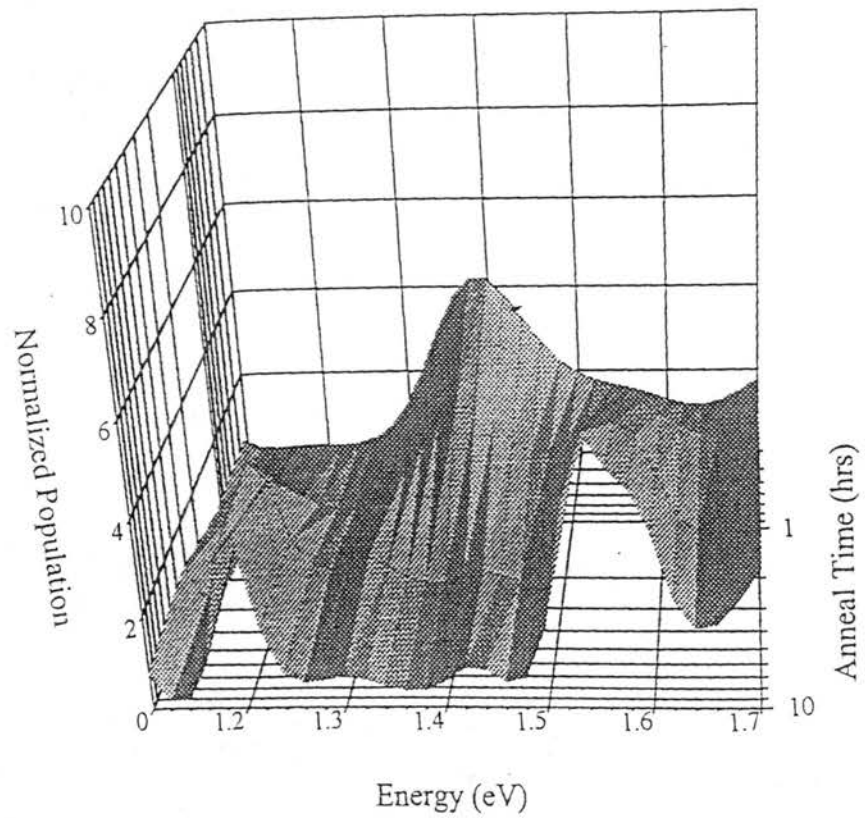
Figure 7.18 - Deconvolution Spectra for 20 μm Powder Gamma-Induced TL. The deconvolved activation energy spectra of the TL glow curves shown in Figure 7.17. Deconvolution parameters: 31 curvlets, s = 10^{14} s^{-1} and ΔE = 20 meV.

7.5   Discussion

The data presented suggest that the high temperature anneal of fine grain α-Al_2O_3:C powder in an oxygen atmosphere desensitizes the radiation induced response of the material. Since the sensitivity of this material has been attributed to the presence of oxygen vacancies introduced into the crystal during the growth process[32], this desensitization is presumed to result from the diffusion of oxygen atoms into the crystal lattice. This is supported further by the apparent lack of appreciable F-center luminescence in samples which have been annealed in oxygen for 10 hours, regardless of the grain sizes used in this study.

The most interesting result of this study is the apparent decrease of UV-induced TL resulting from exposure to neutrons. The UV-induced TL was initially anticipated to increase, as a result of neutron-induced defects within the crystal lattice. This contradicts the work of others, who report the introduction of additional oxygen-vacancies into Al_2O_3 following exposure to neutrons[12,15,16,18,22,26]. However, these authors exposed their samples to much higher neutron fluences (~6–10 orders of magnitude higher) than those used in this study. The data presented simply suggest that while the exposure to neutrons may indeed introduce defects into the crystal lattice, any additional luminescence resulting from these defects is lost.

One possible explanation of this phenomena assumes an increase in neutron-induced defects within the crystal. However, these defects are assumed to be localized around the damage track produced by the higher LET particles, rather than distributed throughout crystal. As a result, heating the material (following any post-neutron exposure excitation) may produce luminescence throughout the crystal, with localized bright spots related to the localized defects. However, the luminescence from these bright spots may not escape the

131

surrounding crystal structure (resulting from self-absorption in the surrounding track defects), much less be detectable by the photomultiplier tube. This effect could then account for the measured luminescence of the post-neutron UV-induced TL being less than that of the pre-neutron UV-induced TL.

in water. The dosimeter has a near-linear ultraviolet dose response with a dynamic range of at least 3 decades, from 10^2 μJ cm^{-2} to 10^5 μJ cm^{-2}, and very little temperature dependence in the region of biological interest (273-323 K). The inherent angular dependence of the interference filter used in the dosimeter is partially flattened due to the wavelength dependence of the phototransferred thermoluminescence efficiency in this wavelength region, the shift in the transmission wavelength of the filter as a function of incident angle and through the use of diffusers.

The results of the deconvolution study are mixed. In general, the method of TL glow curve deconvolution described demonstrates the ability to detect the presence or absence of high LET particle exposure, provided the LET dependence of the particular sample in question is known. However, the current technique does not allow clear discrimination of LET specific information (i.e. particle type) and, as a result, cannot yet be used as a quantitative dosimetric tool. This may be due to the irreproducible nature of the main dosimetric TL peak of α-Al$_2$O$_3$:C.

The high temperature anneal of fine grain α-Al$_2$O$_3$:C powder in an oxygen atmosphere desensitizes the radiation induced response of the material by, presumably, diffusing oxygen atoms into the crystal lattice. The apparent lack of appreciable F-center luminescence in samples which have been annealed in oxygen for 10 hours supports this view. In addition, the UV-induced TL was initially anticipated to increase, as a result of neutron-induced defects within the crystal lattice. However, the most interesting result of this study is the apparent decrease of UV-induced TL resulting from exposure to neutrons. This effect has not yet been explained. One possible reason for no increase in UV-induced TL following exposure to neutrons may result from too little exposure. The neutron dose delivered in this study was

approximately 50 mGy, which corresponds to approximately 1×10^{11} neutrons. This may be several orders of magnitude lower than required for any detectable increase in the UV-induced TL signal.

8.2   Future Work

The investigation of the TL and PTTL properties of as-grown α-Al_2O_3:C have been fairly extensive. However, a study of the PTTL resulting from long illumination times, including an analysis similar to that of Alexander et al.[93], could provide additional insight into the trapping and detrapping mechanisms of the optically active deep traps.

The UVB dosimeter could be redesigned to use optical stimulation (specifically, pulsed OSL or POSL) as the measurement stimulus, rather than heat. This would decrease the measurement time of each sample tremendously (approximately 1 s for POSL compared to approximately 600 s for TL). In addition, the α-Al_2O_3:C detector could consist of a 'powder-in-plastic' thin-layer detector, rather than the current thin-layer design. These mass produced detectors are more homogeneous and much less expensive than the thin-layer design currently in use. As a result, hundreds of detectors could receive a pre-dose at the same time, thus eliminating the need for individual detector calibrations. Once the detectors have been used, they could be stored or discarded, eliminating the need for the restoration dose phase of the current design. The restoration dose has proven to be far too time consuming in exchange for the re-usabilty of the current detectors and would not be cost-effective for any commercial applications.

Another goal of the UVB dosimeter project could involve the development of a portable field POSL reader. This would allow users of the UVB dosimeter to read the detectors in the

135

field, rather than shipping the detectors back to the laboratory for analysis. This could prove to be very attractive to UVB researchers around the world.

The deconvolution analysis could be refined to include the analysis of the proper attempt-to-escape frequency factor, rather than using a constant value supplied by the user. However, this analysis would require an additional data set (such as the heating rate dependence of the TL glow curve) and this, in turn, would be computationally expensive. Nonetheless, the deconvolution of a set of heating rate dependent TL glow curves into a contour plot of relative population densities as a function of activation energy and frequency factor would be attractive to the dosimetric community. Since the current 2-dimensional analysis techniques typically resolve TL glow curves into trap dependent values of E and s, the 3-dimensional counterpart described above may help to assuage the anticipated criticism of the current deconvolution analysis method.

Much of the work presented in Chapters 3 and 4 could be extended to the thermochemically treated α-Al$_2$O$_3$:C powders discussed in Chapter 7. In particular, the wavelength and temperature dependence of PTTL may provide more information as to the existence of optically active deep traps in this material, as well as the extent to which the F- and F$^+$-center population have been affected by the high temperature oxygen anneal. However, the decrease in UV-induced TL following exposure to neutrons indicates a lack of phototransfer from deep traps. As a result, the thermochemically treated powders may lack any significant concentration of optically active deep traps.

Bibliography

1.   Rieke, J.K. and Daniels, F. *Thermoluminescence Studies of Aluminum Oxide*. J. Phys. Chem. **61**(5), 629–633 (1957)

2.   Hunt, R.A. and Schuler, R.H. *Saturation in the X-Ray Coloration of Corundum Single Crystals*. Phys. Rev. **89**(3), 664 (1953)

3.   Levy P.W. and Dienes G.J. *Report of Bristol Conference on Defects in Crystalline Solids, July 1954*. The Physical Society (London) (1955)

4.   Dienes G.J. and Vineyard, G.H. *Radiation Effects in Solids*. Interscience Publishers (New York) (1957)

5.   Arnold, G.W. and Compton, W.D. *Threshold Energy for Lattice Displacement in α-Al_2O_3*. Phys. Rev. Lett. **4**(2), 66–68 (1960)

6.   Novotny, J. and Spurny, Z. *The Effect of X-Rays on Ruby*. Czech. J. Phys. **B16**(2), 119–124 (1966)

7.   Buckman, W.G., Philbrick, C.R. and Underwood, N. *Proceedings of the 2nd International Conference on Luminescence Dosimetry*. CONF-680920 (1968)

8.   Buckman, W.G. *Aluminum Oxide Thermoluminescence Properties for Detecting Radiation*. Health Phys. **22**(4), 402 (1972)

9.   McDougall, R.S. and Rudin, S. *Thermoluminescent Dosimetry of Aluminum Oxide*. Health Phys. **19**(8), 281–283 (1970)

10.   Mitchell, E.W.J., Rigden, J.D. and Townsend, P.D. Philos. Mag. **5**, 1013 (1960)

11.   Levy, P.W. *Color Centers and Radiation-Induced Defects in Al_2O_3*. Phys. Rev. **123**(4), 1226–1233 (1961)

12.   Turner, T.J. and Crawford, J.H. *Nature of the 6.1 eV Band in Neutron-Irradiated Al_2O_3 Single Crystals*. Phys. Rev. B **13**(4), 1735–1740 (1976)

13.   Lee, K.H. and Crawford, J.H. *Electron Centers in Single-Crystal Al_2O_3*. Phys. Rev. B **15**(8), 4065–4070 (1977)

14.   Lee, K.H. and Crawford, J.H. *Additive Coloration of Sapphire*. Appl. Phys. Lett. **33**(4), 273–275 (1978)

15.   Evans, B.D. and Stapelbroek, M. *Optical Properties of the F^+ Center in Crystalline Al_2O_3*. Phys. Rev. B **18**(12), 7089–7098 (1978)

16. Pogatshnik, G.J., Chen, Y. and Evans, B.D. *A Model of Lattice Defects in Sapphire*. IEEE Trans. Nucl. Sci. **NS-34**(6), 1709–1712 (1987)

17. Evans, B.D. *Optical Transmission in Undoped Crystalline α-Al_2O_3 Grown by Several Techniques*. J. Appl. Phys. **70**(7), 3995–3997 (1991)

18. Evans, B.D., Pogatshnik, G.J. and Chen, Y. *Optical Properties of Lattice Defects in α-Al_2O_3*. Nucl. Instr. Meth. B **91**(3), 258–262 (1994)

19. Kristianpoller, N. and Rehavy, A. *Luminescence Centers in Al_2O_3*. J. Luminescence **18&19**(N), 239–243 (1979)

20. Draeger, B.G. and Summers, G.P. *Defects in Unirradiated α-Al_2O_3*. Phys. Rev. B **19**(2), 1172–1177 (1979)

21. Lee, K.H. and Crawford, J.H. *Luminescence of the F Center in Sapphire*. Phys. Rev. B **19**(6), 3217–3221 (1979)

22. Jeffries, B. Summers, G.P. and Crawford, J.H. *F-Center Fluorescence in Neutron-Bombarded Sapphire*. J. Appl. Phys. **51**(7), 3984–3986 (1980)

23. Brewer, J.D., Jeffries, B.T. and Summers, G.P. *Low-Temperature Fluorescence in Sapphire*. Phys. Rev. B **22**(10), 4900–4906 (1980)

24. Jeffries, B.J., Brewer, J.D. and Summers, G.P. *Photoconductivity and Charge Trapping in α-Al_2O_3*. Phys. Rev. B **24**(10), 6074–6082 (1981)

25. Summers, G.P. *Thermoluminescence in Single Crystal α-Al_2O_3*. Radiat. Prot. Dosim. **8**(1–2), 69–80 (1984)

26. Pogatshnik, G.P. and Chen, Y. *Enhancement of Color Center Luminescence in Neutron Irradiated Al_2O_3*. J. Luminescence **40&41**(N), 315–316 (1988)

27. Evans, B.D. *Ubiquitous Blue Luminescence from Undoped Synthetic Sapphires*. J. Luminescence **60&61**(N), 620–626 (1994)

28. Mehta, S.K. and Sengupta, S. *Gamma Dosimetry with Al_2O_3 Thermoluminescent Phosphor*. Phys. Med. Biol. **21**(6), 955–964 (1976)

29. Mehta, S.K. and Sengupta, S. *Annealing Characteristics and Nature of Traps in Al_2O_3 Thermoluminescent Phosphor*. Phys. Med. Biol. **22**(5), 863–872 (1977)

30. Osvay, M. and Biro, T. *Aluminum Oxide in TL Dosimetry*. Nucl. Instr. Meth. **175**(N), 60–61 (1980)

31. Pokorny, P. and Ibarra, A. *Impurity Effects on the Thermoluminescence of Al_2O_3*. J. Appl. Phys. **75**(2), 1088–1092 (1994)

32. Akselrod. M.S., Kortov, V.S., Kravetsky, D.J. and Gotlib, V.I. *Highly Sensitive Thermoluminescent Anion-Defective α-Al₂O₃:C Single Crystal Detectors.* Radiat. Prot. Dosim. **32**(1), 15–20 (1990)

33. Azorin, J., Rubio, J., Gutiérrez, A., González, P. and Rivera, T. *Dosimetric Characteristics and Glow Curve Kinetic Analysis of α-Al₂O₃:C Thermoluminescence Detectors.* J. Therm. Anal. **39**(N), 1107–1116 (1993)

34. Moscovitch, M., Kaufman, M.M., Rodgers, J.E. and Niroomand-Rad, A. *Ultra-Low (100 nGy–100 μGy) Dose Response of α-Al₂O₃:C.* Radiat. Prot. Dosim. **47**(1–4), 173–176 (1993)

35. Mukherjee, B. and Lucas, A.C. *Light Conversion Efficiency of Aluminum Oxide Dosemeters Irradiated with [241]Am Alpha Particles.* Radiat. Prot. Dosim. **47**(1–4), 177–180 (1993)

36. Soumana, S., Faïn, J., Miallier, D., Montret, M., Pilleyre, T., Sanzelle, S. and Akselrod, M. *Gamma and Enclosure Dosimetry for TL/ESR Dating with the New Al₂O₃:C TL Dosemeter.* Radiat. Meas. **23**(2–3), 501–505 (1994)

37. Kitis, G., Papadopoulos, J.G., Charalambous, S. and Tuyn, J.W.N. *The Influence of Heating Rate on the Response and Trapping Parameters of α-Al₂O₃:C.* Radiat. Prot. Dosim. **55**(3), 183–190 (1994)

38. Kortov, V.S., Milman, I.I., Kirpa, V.I. and Lesz, J. *Some Features of α-Al₂O₃ Dosimetric Thermoluminescent Crystals.* Radiat. Prot. Dosim. **55**(4), 279–284 (1994)

39. Mil'man, I.I., Kortov, V.S. and Kirpa, V.I. *Thermal Quenching in the Luminescence of Anion-Defect α-Al₂O₃.* Phys. Solid State **37**(4), 625–629 (1995)

40. Pashchenko, L.P. and Barboza-Flores, M. *Thermoluminescence α-Al₂O₃:C Detectors (TLD-500K): Some Results of a Long-Term Testing.* Radiat. Meas. **24**(4), 427–429 (1995)

41. Pető, Á and Kelemen, A. *Radioluminescence Properties of α-Al₂O₃ TL Dosemeters.* Radiat. Prot. Dosim. **65**(1–4), 139–142 (1996)

42. Klemic, G.A., Azziz, N. and Marino, S.A. *The Neutron Response of Al₂O₃:C, [7]LiF:Mg,Cu,P and [7]LiF:Mg,Ti TLDs.* Radiat. Prot. Dosim. **65**(1–4), 221–226 (1996)

43. Kitis, G., Charalambous, S. and Tuyn, J.W.N. *The Dose Response Function of α-Al₂O₃:C under Isothermal Decay Conditions.* Radiat. Prot. Dosim. **65**(1–4), 239–242 (1996)

44. Kortov, V.S., Milman, I.I., Kirpa, V.I. and Lesz, J. *Thermal Quenching of TL in α-Al₂O₃ Dosimetric Crystals.* Radiat. Prot. Dosim. **65**(1–4), 255–258 (1996)

45. Akselrod, M.S., McKeever, S.W.S., Moscovitch, M., Emfietzoglou, D., Durham, J.S. and Soares, C.G. *A Thin-Layer Al₂O₃:C Beta TL Detector.* Radiat. Prot. Dosim. **66**(1–4), 105–110 (1996)

46. Budzanowski, M., Bilski, P., Bøtter-Jensen, L., Delgado, A., Olko, P., Sáez-Vergara, J.C. and Waligórski, M.P.R. *Comparison of LiF:Mg,Cu,P (MCP-N, Gr-200A) and α-Al₂O₃:C TL Detectors in Short-Term Measurements of Natural Radiation.* Radiat. Prot. Dosim. **66**(1–4), 157–160 (1996)

47. Akselrod, M.S. and Kortov, V.S. *Thermoluminescent and Exoemission Properties of New High-Sensitivity TLD α-Al₂O₃:C Crystals.* Radiat. Prot. Dosim. **33**(1–4), 123–126 (1990)

48. Kortov, V. and Milman, I. *Some New Data on Thermoluminescence Properties of Dosimetric α-Al₂O₃ Crystals.* Radiat. Prot. Dosim. **65**(1–4), 179–184 (1996)

49. Flerov, V.I., Skvortsova, V. and Flerov, A.V. *Thermoluminescence of Reactor-Irradiated Aluminum Oxide.* Radiat. Prot. Dosim. **65**(1–4), 227–230 (1996)

50. Springis, M., Kulis, P., Veipals, A., Tale, V. and Tale, I. *Origin of the 430 K TL Peak in Thermochemically Reduced α-Al₂O₃.* Radiat. Prot. Dosim. **65**(1–4), 231–234 (1996)

51. Papin, E., Grosseau, P., Guilhot, B., Benabdesselam, M., Iacconi, P. and Lapraz, D. *Influence of the Calcining Conditions on the Thermoluminescence of Pure and Doped α-Alumina Powders.* Radiat. Prot. Dosim. **65**(1–4), 243–246 (1996)

52. Pêtel, F., Iacconi, P., Bindi, R., Lapraz, D. and Breuil, P. *Simultaneous Detection of Thermostimulated Luminescence and Exoelectronic Emission Between 77 and 650 K: Application to Alpha Alumina.* Radiat. Prot. Dosim. **65**(1–4), 247–250 (1996)

53. Kim, T.K., Choe, H.S. and Whang, C.N. *Thermoluminescence of Na⁺ Ion Implanted Al₂O₃ Induced by ¹³⁷Cs Gamma Rays.* Radiat. Prot. Dosim. **65**(1–4), 251–254 (1996)

54. Akselrod, M.S. and Gorelova, E.A. *Deep Traps in Highly Sensitive α-Al₂O₃:C TLD Crystals.* Nucl. Tracks Radiat. Meas. **21**(1), 143–146 (1993)

55. Akselrod, M.S., Kortov, V.S. and Gorelova, E.A. *Preparation and Properties of α-Al₂O₃:C.* Radiat. Prot. Dosim. **47**(1–4), 159–164 (1993)

56. Moscovitch, M., Tawil, R.A. and Svinkin, M. *Light Induced Fading in α-Al₂O₃:C.* Radiat. Prot. Dosim. **47**(1–4), 251–253 (1993)

57. Musk, J.H. *Time-Dependent and Light-Induced Fading in Victoreen Model 2600-80 Aluminum Oxide Thermoluminescence Dosemeters.* Radiat. Prot. Dosim. **47**(1–4), 247–249 (1993)

58. Walker, F.D., Colyott, L.E., Agersnap-Larsen, N. and McKeever, S.W.S. *The Wavelength Dependence of Light-Induced Fading of Thermoluminescence from α-Al_2O_3:C.* Radiat. Meas. **26**(5), 711–718 (1996)

59. Izak-Biran, T. and Moscovitch, M. *Light Sensitivity and Light-Induced Fading in α-Al_2O_3:C.* Radiat. Meas. **26**(2), 259–264 (1996)

60. Oster, L., Weiss, D. and Kristianpoller, N. *A Study of Photostimulated Thermoluminescence in C-Doped α-Al_2O_3 Crystals.* J. Phys. D **27**(8), 1732–1736 (1994)

61. Markey, B.G., Colyott, L.E. and McKeever, S.W.S. *Time-Resolved Optically Stimulated Luminescence from α-Al_2O_3:C.* Radiat. Meas. **24**(4), 457–463 (1995)

62. Markey, B.G, McKeever, S.W.S., Akselrod, M.S., Bøtter-Jensen, L., Agersnap-Larsen, N. and Colyott, L.E. *The Temperature Dependence of Optically Stimulated Luminescence from α-Al_2O_3:C.* Radiat. Prot. Dosim. **65**(1–4), 185–190 (1996)

63. Tale, I., Piters, T.M., Barboza-Flores, M., Perez-Salas, R., Aceves, R. and Springis, M. *Optical Properties of Complex Anion Vacancy Centres and Photo-Excited Electronic Processes in Anion-Defective α-Al_2O_3.* Radiat. Prot. Dosim. **65**(1–4), 235–238 (1996)

64. Emfietzoglou, D. and Moscovitch, M. *Phenomenological Study of Light-Induced Effects in α-Al_2O_3:C.* Radiat. Prot. Dosim. **65**(1–4), 259–262 (1996)

65. Colyott, L.E., Akselrod, M.S. and McKeever, S.W.S. *Phototransferred Thermoluminescence in α-Al_2O_3:C.* Radiat. Prot. Dosim. **65**(1–4), 263–266 (1996)

66. McKeever, S.W.S., Akselrod, M.S. and Markey, B.G. *Pulsed Optically Stimulated Luminescence Dosimetry Using α-Al_2O_3:C.* Radiat. Prot. Dosim. **65**(1–4), 267–272 (1996)

67. Bøtter-Jensen, L. and McKeever, S.W.S. *Optically Stimulated Luminescence Dosimetry Using Natural and Synthetic Materials.* Radiat. Prot. Dosim. **65**(1–4), 273–280 (1996)

68. Roesch, W.C. and Attix, F.H. In *Radiation Dosimetry, Vol. I: Fundamentals* (eds. Attix, F.H. and Roesch, W.C.). Academic Press (New York) (1968)

141

69. Attix, F.H. *Introduction to Radiological Physics and Radiation Dosimetry*. John Wiley & Sons (New York). ISBN 0 471 01146 0. (1986)

70. Daniels, F., Boyd, C.A. and Saunders, D.F. *Thermoluminescence as a Research Tool*. Science 117(3040), 343–349 (1953)

71. McKeever, S.W.S. *Thermoluminescence of Solids*. Cambridge University Press (Cambridge). ISBN 0 521 24520 6. (1985)

72. Cameron, J.R., Suntharalingam, N. and Kenney, G.N. *Thermoluminescence Dosimetry*. University of Wisconsin Press (Madison). (1968)

73. McKeever, S.W.S., Moscovitch, M. and Townsend, P.D. *Thermoluminescence Dosimetry Materials: Properties and Uses*. Nuclear Technology Publishing (Kent). ISBN 1 870965 19 1. (1995)

74. Randall, J.T. and Wilkins, M.H.F. *Phosphorescence and Electron Traps I. The Study of Trap Distributions*. Proc. Roy. Soc. (London) **A184**(A999), 366–389 (1945)

75. Randall, J.T. and Wilkins, M.H.F. *Phosphorescence and Electron Traps II. The Interpretation of Long-Period Phosphorescence*. Proc. Roy. Soc. (London) **A184**(A999), 390–407 (1945)

76. Garlick, G.F.J. and Gibson, A.F. *The Electron Trap Mechanism of Luminescence in Sulphide and Silicate Phosphors*. Proc. Phys. Soc. **A60**(6), 574–590 (1948)

77. Chen, R. and McKeever. S.W.S. *Theory of Thermoluminescence and Related Phenomena*. World Science Publishing (Singapore). ISBN 0 000 00000 0. (1997)

78. Lewandowski, A.C. and McKeever, S.W.S. *Generalized Description of Thermally Stimulated Processes Without the Quasiequilibrium Approximation*. Phys. Rev. B **43**(10), 8163–8178 (1991)

79. McKeever, S.W.S., Lewandowski, A.C. and Markey, B.G. *A New Look at Thermoluminescence Kinetics*. Radiat. Prot. Dosim. **47**(1–4), 9–16 (1993)

80. Lewandowski, A.C., Markey, B.G. and McKeever, S.W.S. *Analytical Description of Thermally Stimulated Luminescence and Conductivity Without the Quasiequilibrium Approximation*. Phys. Rev. B **49**(12), 8029–8047 (1994)

81. Hoogenstraaten, W. *Electron Traps in Zinc-Sulphide Phosphors*. Philips Res. Reports **13**(6), 515–693 (1958)

82. Chen, R. *On the Calculation of Activation Energies and Frequency Factors from Glow Curves*. J. Appl. Phys. **40**(2), 570–585 (1969)

83. Keating, P.N. *Thermally Stimulated Emission and Conductivity Peaks in the Case of Temperature Dependent Trapping Cross Sections*. Proc. Phys. Soc. (London) **78**(2), 1408–1415 (1961)

84. Haering, R.R. and Adams, E.N., *Theory and Application of Thermally Stimulated Currents in Photoconductors*. Phys. Rev. **117**(2), 451–454 (1960)

85. Halperin, A. and Braner, A.A. *Evaluation of Thermal Activation Energies from Glow Curves*. Phys. Rev. **117**(2), 408–415 (1960)

86. Dussel, G.A. and Bube, R.H. *Theory of Thermally Stimulated Conductivity in a Previously Photoexcited Crystal*. Phys. Rev. **155**(3), 764–779 (1967)

87. Saunders, I.J. *The Thermally Stimulated Luminescence and Conductivity of Insulators*. J. Phys. C **2**(2), 2181–2198 (1969)

88. Chen, R., Kristianpoller, N., Davidson, Z. and Visocekas, R. *Mixed First and Second Order Kinetics in Thermally Stimulated Processes*. J. Luminescence **23**(3/4), 293–303 (1981)

89. Bøtter-Jensen, L., Agersnap-Larsen, N., Mejdahl, V., Poolton, N.R.J., Morris, M.F. and McKeever, S.W.S. *Luminescence Sensitivity Changes in Quartz as a Result of Annealing*. Radiat. Meas. **24**(4), 513–541 (1995)

90. McKeever, S.W.S., Bøtter-Jensen, L., Agersnap-Larsen, N., Mejdahl, V., and Poolton, N.R.J. *Optically Stimulated Luminescence Sensitivity Changes in Quartz Due to Repeated Use in Single Aliquot Readout: Experiments and Computer Simulations*. Radiat. Prot. Dosim. **65**(1–4), 49–54 (1996)

91. McKeever, S.W.S., Agersnap-Larsen, N., Bøtter-Jensen, L. and Mejdahl, V. *OSL Sensitivity Changes During Single Aliquot Procedures: Computer Simulations*. Radiat. Meas. **27**(2), 75–82 (1997)

92. McKeever, S.W.S., Bøtter-Jensen, L., Agersnap-Larsen, N. and Duller, G.A.T. *Temperature Dependence of OSL Decay Curves: Experimental and Theoretical Aspects*. Radiat. Meas. **27**(2), 161–170 (1997)

93. Alexander, C.S., Morris, M.F. and McKeever, S.W.S. *The Time and Wavelength Response of Phototransferred Thermoluminescence in Natural and Synthetic Quartz*. Radiat. Meas. **27**(2), 153–159 (1997)

94. McKeever, S.W.S. *Mechanisms of Thermoluminescence Production: Some Problems and a Few Answers?* Nucl. Tracks Radiat. Meas. **18**(1–2), 5–12 (1991)

95. McKeever, S.W.S. *Models for Optical Bleaching of Thermoluminescence in Sediments*. Radiat. Meas. **23**(2–3) 267–275 (1994)

96. Böer K. W. *Survey of Semiconductor Physics*. Van Nostrand Reinhold (New York). ISBN 0 442 23793 6. (1990)

97. Bessonova, T. C., Tale, I. A. and Kulis, P.A. *Relaxation Processes in Irradiated Ruby*. Inorg. Mater. **20**, 1000–1003 (1984).

98. Akselrod M.S., Kortov V. S., Kravetsky D. J. and Gotlib V. I. *Highly Sensitive Thermoluminescent Anion-defective α-Al₂O₃:C Single Crystal Detectors*. Radiat. Prot. Dosim. **33**, 119–122 (1990)

99. ICRP. *The 1990-1991 Recommendation of the International Commission of Radiological Protection*. Publication 60, Ann. ICRP 21, 1–3 (1991)

100. Rathbone B. A., Endres A. W. And Antonio E. J. *Evaluation of New and Conventional Thermoluminescent Phosphors for Environmental Monitoring Using Automated Thermoluminescent Dosimeter Readers*. In Proc. 4th. Conf. Radiation Protection and Dosimetry, Orlando, October, 1994. ORNL/TM-12817, 371–380 (1994)

101. Bøtter-Jensen L., Poolton N. R. J., Willumsen F. and Christiansen H. *A Compact Design for Monochromatic OSL Measurements in the Wavelength Range 380-1020 nm*. Radiat. Meas. **23**(2–3), 519–522 (1994)

102. Fredrick, J.E. *Ultraviolet Sunlight in an Evolutionary and Biological Context*. World Meteorol. Org. Report No. 100, Buenos Aires (1994)

103. Madronich, S., McKenzie, R.L., Caldwell, M.M. and Björn, L.O. *Changes in Ultraviolet Radiation Reaching the Earth's Surface*. Ambio **24**(3), 143–152 (1995)

104. Lubin, D. and Jensen, E.H. *Effects of Clouds and Stratospheric Ozone Depletion on Ultraviolet Radiation Trends*. Nature **377**(6551), 710–713 (1995)

105. Miller, A.J., Hollandsworth, S.M., Flynn, L.E., Tiao, G.C., Reinsel, G.C., Bishop, L., McPeters, R.D., Planet, W.G., DeLuisi, J.J., Mateer, C.L., Wuebbles, D., Kerr, J. and Nagatani, R.M. *Comparisons of Observed Ozone Trends and Solar Effects in the Stratosphere Through Examination of Ground-based Umkehr and Combined Solar Backscattered Ultraviolet (SBUV) and SBUV-2 Satellite Data*. J. Geophys. **101**(C4), 9017–9021 (1996)

106. Driscoll, C.M.H. *Solar UVR Measurements*. Radiat. Prot. Dosim. **64**(3) 179–188 (1996)

107. Quintern, L.E., Puskeppeleit, M., Rainer, P., Weber, S., El Naggar, S., Eschweiler, U. and Horneck, G. *Continuous Dosimetry of the Biologically Harmful UV-Radiation in Antarctica with the Biofilm Technique*. Photochem. Photobiol. B **22**(1), 59–66 (1994)

108. Kerr, J.B. and McElroy, C.T. *Evidence for Large Upward Trends of Ultraviolet-B Radiation Linked to Ozone Depletion.* Science **262**(5136), 1032–1034 (1993)

109. Berkelaar, E.J., Ormrod, D.P. and Hale, B.A. *The Influence of Photosynthetically Active Radiation on the Effects of Ultraviolet-B Radiation on* Arabidopsis thaliana. Photochem. Photobiol. **64**(1), 110–116 (1996)

110. Feldheim, K. and Conner, J.K. *The Effects of Increased UV-B Radiation on Growth, Pollination Success and Lifetime Female Fitness in Two* Brassica *Species.* Oecologia **106**(3), 284–297 (1996)

111. Day, T.A., Howells, B.W. and Ruthland, C.T. *Changes in Growth and Pigment Concentrations with Leaf Age in Pea Under Modulated UV-B Radiation Field Treatments.* Plant Cell Environ. **19**(1), 101–108 (1996)

112. Blanke, M.M. *Transmission of UV-Irradiance into Nectarine Fruit.* J. Appl. Botany **70**(1–2), 76–77 (1996)

113. Kim, H.Y., Kobayashi, K., Nouchi, I. and Yoneyama, T. *Enhanced UV-B Radiation has Little Effect on Growth, $\delta^{13}C$ Values and Pigments of Pot-Grown Rice (*Oryza sativa*) in the Field.* Physiol. Plant **96**(1), 1–5 (1996)

114. Barnes, P.W., Ballaré, C.L. and Caldwell, M.M. *Photomorphogenic Effects of UV-B Radiation on Plants: Consequences for Light Competition.* J. Plant Physiol. **148**(1–2), 15–20 (1996)

115. Rau, W. and Hofmann, H. *Sensitivity of UV-B of Plants Growing in Different Altitudes in the Alps.* J. Plant Physiol. **148**(1–2), 21–25 (1996)

116. Middleton, E.M., Chappelle, E. W., Cannon, T.A., Adamse, P. and Britz, S.J. *Initial Assessment of Physiological Response to UV-B Irradiation Using Fluorescence Measurements.* J. Plant Physiol. **148**(1–2), 69–77 (1996)

117. Teramura, A.H. *Effects of Ultraviolet Radiation on the Growth and Yield of Crop Plants.* Physiol. Plant. **58**(3), 415–427 (1983)

118. Olszyk, D., Dai, Q., Teng. P., Leung, H., Luo, Y. and Peng, S. *UV-B Effects on Crops: Response of the Irrigated Rice Ecosystem.* J. Plant Physiol. **148**(1–2), 26–34 (1996)

119. Mark, U. and Tevini, M. *Combination Effects of UV-B Radiation and Temperature on Sunflower (*Helianthus annuus *L., cv. Polstar) and Maize (*Zea mays *L., cv. Zenit 2000) Seedlings.* J. Plant Physiol. **148**(1–2), 49–56 (1996)

120. Morison, W.L. *Effects of Ultraviolet Radiation on the Immune System in Humans.* Photochem. Photobiol. **50**(4), 515–524 (1989)

145

121. Parrish, J.A., Jaenicke, K.F. and Anderson, R.R. *Erythema and Melanogenesis Action Spectra of Normal Human Skin*. Photochem. Photobiol. 36(2), 187–191 (1982)

122. Setlow, R.B. *The Wavelengths in Sunlight Effective in Producing Skin Cancer: A Theoretical Analysis*. Proc. Nat. Acad. Sci. 71(9), 3363–3366 (1974)

123. Brash, D.E. *UV Mutagenic Photoproducts in* Escherichia Coli *and Human Cells: A Molecular Genetics Perspective on Human Skin Cancer*. Photochem. Photobiol. 48(1), 59–66 (1988)

124. Urbach, F. *Potential Effects of Altered Solar Ultraviolet Radiation on Human Skin Cancer*. Photochem. Photobiol. 50(4), 507–513 (1989)

125. Nolan, C.V. and Amanatidis, G.T., *European Commission Research on the Fluxes and Effects of Environmental UVB Radiation*. J. Photochem. Photobiol. B 31(1), 3–7 (1995)

126. Sliney, D.H. *UV Radiation Ocular Exposure Dosimetry*. J. Photochem. Photobiol. B 31(1), 69–77 (1995)

127. Taylor, H.R., West, S.K., Rosenthal, F.S., Muñoz, M.S., Newland, H.S., Abbey, H. and Emmett, E.A. *Effect of Ultraviolet Radiation on Cataract Formation*. New Engl. J. Med. 319(22), 1429–1433 (1988)

128. Francis, A.A., Carrier, W.L. and Regan, J.D. *The Effect of Temperature and Wavelength on Production and Photolysis of a UV-Induced Photosensitive DNA Lesion which is not repaired in Zeroderma Pigmentosum Variant Cells*. Photochem. Photobiol. 48(1), 67–71 (1988)

129. Webb, A.R. *Measuring UV Radiation: A Discussion of Dosemeter Properties, Uses and Limitations*. J. Photochem. Photobiol. B 31(1), 9–13 (1995)

130. Lyman, T. *The Transparency of the Air Between 1100 and 1300 Å*. Phys. Rev. 48(1) 149–151 (1935)

131. Schayes, R., Brooke, C., Kozlowitz, I. and L'Heureux, M. *Thermoluminescent Properties of Natural Calcium Fluoride*. Proc. 1ˢᵗ Int. Conf. on Luminescence Dosimetry, Stanford. CONF 650637, AEC Symposium Series 8 (NTIS, Springfield, VA) (1967)

132. Okuno, E. and Watanabe, S. *U.V. Induced Thermoluminescence on Natural Calcium Fluoride*. Health Phys. 23(9) 377–382 (1972)

133. Buckman, W.G. and Payne, M.R. *Photostimulated Thermoluminescence of Lithium Fluoride as an Ultraviolet Radiation Dosimeter*. Health Phys. 31(12) 501–504 (1976)

146

134. Oberhofer, M. *Dosimetry of Non-Ionizing Radiation*. Radiat. Prot. Dosim. **6**(1–4), 109–112 (1983)

135. Driscoll, C.M.H., McKinlay, A.F. and Smith, P.A. *Multiple Dose Re-Assessment of Lithium Fluoride by the Ultra-Violet Phototransferred Thermoluminescence Technique*. Radiat. Prot. Dosim. **6**(1–4), 117–120 (1983)

136. Chakrabarti, K., Mathur, V.K., Abbundi, R.J. and Hill, M.D. *UV Induced Trapping in Powder and in Sintered $CaSO_4$:Tm and $CaSO_4$:Dy*. Radiat. Prot. Dosim. **33**(1–4), 35–38 (1990)

137. Chang, S.-C. and Su, C.-S. *Direct Thermoluminescence of Sintered ZrO_2 Pellets Induced by Ultraviolet Radiation*. Nucl. Tracks Radiat. Meas. **20**(3), 511–516 (1992)

138. Chang, S.-C. and Su, C.-S. *Influence of the Sintering Process of ZrO_2 Pellets on Thermoluminescence Induced by Ultraviolet Radiation*. Radiat. Prot. Dosim. **47**(1–4), 169–172 (1993)

139. Yeh, S.-H. and Weng, P.-S. *Ultraviolet Radiation Measurement with Neutron Pre-Irradiated Thermoluminescence Dosemeters*. Radiat. Prot. Dosim. **47**(1–4), 689–692 (1993)

140. Fausto, A.M.F., Mol. A.W., Sunta, C.M. and Okuno, E. *Studies on TL of LiF:Mg and/or Cu Exposed to Gamma and UV Rays*. Radiat Prot. Dosim. **51**(3), 211–216 (1994)

141. Su, C.-S. and Yeh, S.-M. *UV Attenuation Coefficient in Water Determined by Thermoluminescence Detector*. Radiat. Meas. **26**(1), 83–86 (1996)

142. Su, C.-S. and Yeh, S.-M. *The Effect of LiF in Gd_2O_3:Eu, Y_2O_3:Eu, ZrO_2:Zn and ZrO_2:Er on UV Induced Thermoluminescence*. Radiat. Prot. Dosim. **65**(1–4), 89–92 (1996)

143. Yeh, S.-M. and Su, C.-S. *UV Induced Thermoluminescence in Rare Earth Oxide Doped Phosphors: Possible Use for UV Dosimetry*. Radiat. Prot. Dosim. **65**(1–4), 359–362 (1996)

144. Potiens, A.J. and Campos, L.L. *Ultraviolet and Laser Radiation Dosimetry Using Phototransferred Thermoluminescence in $CaSO_4$:Dy*. Radiat. Prot. Dosim. **66**(1–4), 95–96 (1996)

VITA

Leslie Edward Colyott

Candidate for the Degree of

Doctor of Philosophy

Thesis: DOSIMETRIC PROPERTIES OF α-AL$_2$O$_3$:C EXPOSED TO IONIZING AND NON-IONIZING RADIATION

Major Field: Physics

Biographical:

Personal Data: Born in Belleville, Illinois on June 10, 1964, the son of Larry E. and Judith C. Colyott.

Education: Graduated from Triad High School, St. Jacob, Illinois in May 1982; received Bachelor of Science degree in Physics and a Bachelor of Science degree in Chemistry from Southern Illinois University, Edwardsville, Illinois in June 1991; received Master of Science degree in Physics from Southern Illinois University, Edwardsville, Illinois in June 1992. Completed the requirements for the Doctor of Philosophy degree with a major in Physics at Oklahoma State University in July 1997.

Experience: Employed by Southern Illinois University, Edwardsville, Illinois as a graduate teaching assistant, 1989 to 1992. Employed by Oklahoma State University, Stillwater, Oklahoma, Department of Physics as a graduate teaching assistant from 1992 to 1994, lead graduate teaching assistant from 1994 to present and graduate research assistant 1993 to present.

Professional Memberships: American Society of Physics Students.